Effect of Rapid Drawdown on the Stability of Railway Embankments

Shuangshuang Xu

A Thesis
In
The Department
of
Building, Civil, and Environmental Engineering

Presented in Partial Fulfillment of the Requirements
for the Degree of
Master of Applied Science (Civil Engineering) at
Concordia University
Montréal, Québec, Canada

August 2019

CONCORDIA UNIVERSITY

School of Graduate Studies

This is to certify that the thesis prepared

By: Shuangshuang Xu

Entitled: Effect of Rapid Drawdown on the Stability of Railway Embankments

and submitted in partial fulfillment of the requirements for the degree of

Master of Applied Science (Civil Engineering)

complies with the regulations of the University and meets the accepted standards with respect to originality and quality.

Signed by the final Examining Committee:

____________________________ Chair and Examiner
Dr. A. M. Hanna

____________________________ Examiner
Dr. A. Dolatabadi

____________________________ Examiner
Dr. B. Li

____________________________ Supervisor
Dr. A. M. Zsaki

Approved by: ____________________ Chair of the Department or Graduate Program Director

____________________ Dean of Faculty

Date:

ABSTRACT

Effect of Rapid Drawdown on the Stability of Railway Embankments

Shuangshuang Xu

The rapid drawdown of water level adjacent to a clay slope under railway embankments reduces the stability of these slopes, which results in further safety implications when a freight train is passing through this area. Thus, to enhance the safety and stability of a clay slope under both rapid drawdown and a moving freight train conditions requires in-depth investigation, which has not been done before. This work is focused on the coupled drawdown analysis with slope stability assessment under undrained conditions using 2-dimensional models through the finite element shear strength reduction (FE-SSR) method. A series of parametric studies were performed including the identification of key factors, such as geometric characteristics of the slope, rapid drawdown ratios, and freight train speeds. The control variable method was introduced to individually study each parameter and its effect on slope stability. For slopes with different geometric parameters and rapid drawdown ratios, maximum safe train speed information is presented for slopes with a minimum factor of safety of 1.3. Noticeably, a slope with 3H:1V slope inclination, and 3-m railway embankment has shown excellent results in terms of high maximum safe train speeds under the studied conditions. As a contribution, this study provides maximum safe train speed information for a slope with different geometric parameters and rapid drawdown ratios, which can be used as a reference for safe freight train operations.

ACKNOWLEDGEMENT

First and foremost, I would like to express my gratitude to my supervisor, Dr. Attila Michael Zsaki, for providing me this opportunity to join his group. His inspiring guidance and consistent support helped me to become an independent researcher.

I am also very grateful to the help provided by Dr. Fubin Tu, for his encouragement and advice on some technical points of this study. This work would not be possible without the endless love and support both in the study and life from my husband, Xiaoqiang Gu. My gratitude also goes to my friends for always being with me during the highs and lows of the past few years.

Finally, I would like to acknowledge the financial support from the Department of Building, Civil, and Environmental Engineering at Concordia University to help me successfully complete the research work.

Table of Contents

List of Tables

List of Figures

Notation

A = bearing area of cross ties (mm^2)
ABP = average ballast pressure (psi) or (MPa)
D = diameter of wheel (in.) or (mm)
DF = distribution factor of axle load carried by a single tie (%)
E = Young's modulus (MPa)
E', υ' = effective elastic parameters (MPa)
F = wheel load (kN)
F_r = resultant wheel load (kN)
G = shear modulus (MPa)
H = initial total head (m)
H_F = height of the soil element (m)
H_n, x = natural slope height (m)
H_r = railway embankment height (m)
H_W = depth of water over the soil element (m)
IF = impact factor (%)
K = stiffness of the spring (N/m)
$[K_E]$ = element stiffness matrix
$[K_G]$ = global stiffness matrix
L = change in water level or drawdown depth (m)
L_O = overall length of railroad car measured over the pulling face of the coupler (m)
N = resultant (total) normal force (kN)
N' = resultant effective normal force (kN)
P = applied load (kN)
R = drawdown rate (m/day)
R_F = rate of FS change
S = degree of saturation (%)
S_I = inboard axle spacing (m)
S_O = outboard axle spacing (m)

S_T = truck axle spacing (m)

T = resultant shear force (kN)

TC = length between the center pin on the trucks (m)

U = displacement (m)

V = train speed (km/h) or (mi/h)

X = width of the soil element (m)

c = cohesion (kPa)

c_h = coefficient of consolidation in the horizontal direction (cm^2/s)

c_v = coefficient of consolidation in the vertical direction (cm^2/s)

h = total head (m)

i = angle formed by a horizontal line and the base of the soil element (°)

k_h, k_x = horizontal hydraulic conductivity (cm/s)

k_v, k_y = vertical hydraulic conductivity (cm/s)

m_v = coefficient of compressibility (m^2/kN)

n = porosity

γ = unit weight of material (kN/m^3) or (kg/ m^3)

γ_1 = shear strain

γ_b = effective unit weight (kN/m^3)

γ_t = total unit weight (kN/m^3)

γ_w = unit weight of water (kN/m^3)

s, t = subgroup number

t_p = time duration of loading pulse (h)

u, u_w = pore pressure (kPa)

u^* = displacement in x direction (m)

v = Poisson's ratio

v^* = displacement in y direction (m)

w = weight of track substructure per unit area (kg/m^2)

z = depth of track substructure (m)

ε = strain

τ = shear strength (kPa)

ϕ = angle of internal friction (°)

σ = normal stress (kPa)

σ' = effective stress (kPa)

σ_{ij} = state of stress

$\{\Delta d_E\}$ = vector of incremental element nodal displacements (m)

$\{\Delta d_G\}$ = vector of all incremental element nodal displacements (m)

$\{\Delta R_E\}$ = vector of incremental element nodal forces (N)

$\{\Delta R_G\}$ = vector of all incremental element nodal forces (N)

Chapter 1 Introduction

1.1 Background

Transportation plays a key role in our economy, international trade, daily life, both in Canada and abroad. As the second largest country in the world with a land area of almost 10 million kilometers, there are many different types of transportation in Canada, including water, rail, motor carrier, pipeline and air (Transport Canada 2017). The economic benefits generated by the transportation section accounted for 4.2 % of Canada's GDP in 2005, higher than that from Canada's mining, oil, and gas extraction industries. It can be seen in Figure 1.1 that truck transportation created the highest Canadian transportation GDP value among all transportation modes in 2005. Noticeably, the share of rail transportation was 13%, among the top three (Dunlavy et al. 2005).

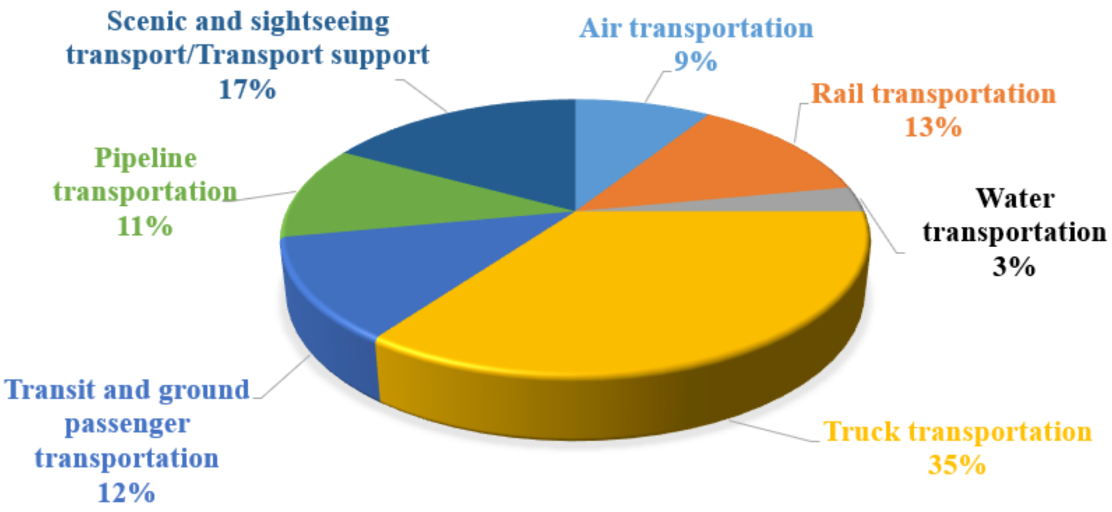

Figure 1. 1. Share of Canadian transportation GDP in 2005 (Dunlavy et al. 2005).

Rail transportation serves both passengers and freight. The Canadian railway system included a total of 41,711 route-kilometers of track in 2017 as shown in Figure 1.2. The two major railway companies are Canadian National and Canadian Pacific Railway, who own over 82% railway routes in Canada (Transport Canada 2017). Particularly, both are freight railway companies, generating approximately 93% of total revenues of rail services in 2006 (Transport Canada 2006). Freight rail transportation is the most critical transportation method to move heavy goods and containerized traffic over long distances. Around 763 billion gross tonnes-kilometers* of freight are transported each year, which has increased the demand for railway safety (Railway Association of Canada 2017).

Figure 1. 2. The Canadian railway network in 2017 (Transport Canada 2017).

According to the Transportation Safety Board of Canada (TSB), the year 2014 has the most incidents related to railways (1455), while the number has drastically dropped to 1224 in 2016 (TSB 2018). However, this number slightly increased to 1365 in 2017 (Figure 1.3). The railway incident data refers to accidents and reportable incidents from the Rail Occurrence Database System, which reflects the performance of regulated freight and passenger member railways (TSB 2018). To improve transportation safety, TSB also investigated and reported some accidents involving embankment/roadbed failure, particularly, the following two derailments.

---

*Gross tonnes-kilometers: The movement of total train weight over a distance of one kilometer. Total train weight consists of the freight cars, their contents, and any inactive locomotives. It excludes the weight of locomotives pulling the trains.

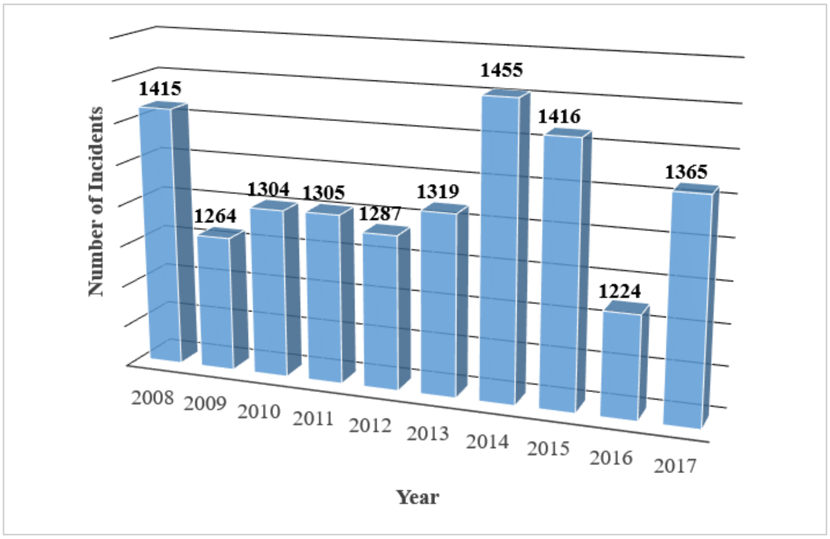

Figure 1. 3. Railway incident data from 2008 to 2017 (TSB 2018).

On 19 July 1992, a Canadian National Railway (CN) freight train (No. 303-18) derailed at Mile 135.0 of the CN Caramat Subdivision near Nakina, Ontario, because of a collapsed subgrade underneath the track at the derailment site (TSB 1992). The train traveled on a suspended part of the track and fell into the lake. In this accident, two crew members died and one sustained serious injury. According to a detailed investigation, the derailment took place due to a roadbed failure, which was destroyed by a 2-meter sudden drawdown of the water caused by a breach of a nearby beaver dam. Also, the rapid drawdown resulted in withdrawing the hydrostatic support from the previously submerged part of the railway embankment.

The Transportation Safety Board also reported another derailment that occurred on 6 May 1997 (TSB 1997). The CN freight train E-283-21-05 traveled from Drummondville, Quebec to Toronto, Ontario, dropping into a depression in the subgrade at Mile 34.55 of the CN Kingston Subdivision next to Coteau-du-Lac, Quebec. The derailment resulted in severe damage to two locomotives and the first 12 of 20 cars. It also led to the puncture of fuel tanks on the locomotives and the leakage of diesel fuel into Rouge River which is located 10 m away from the tracks. Two crew members suffered minor injuries in the accident. The accident site was on a tangent section of double track main line supported by an earth-fill embankment. The derailment was mainly caused by 1) the reduction of the soil strength under the subgrade because of water saturation, 2) the probability of a sudden lowering of the high springtime river level, and 3) the dynamic loading of the heavily loaded moving train.

1.2 Research Objectives and Scope

The rapid drawdown of water levels close to rail lines can trigger embankment collapse causing a derailment. It can potentially threaten railway safety, not only railway property but also life safety. Therefore, this research aims to investigate the effect of slope geometric parameters, rapid drawdown ratios, and moving freight train speeds on slope stability. The slope's factor of safety serves as a measure to quantify the effect. And finally, maximum safe train speeds can be obtained for a given railway slope as an important reference in practice. The detailed objectives are listed below:

- To develop 2-D finite element models of railway embankment on a natural clay slope with various heights of slope and subgrade which adjoins a river.
- To apply the worst drainage condition (undrained condition) for coupled (groundwater flow and stress) drawdown analysis on slope stability, and to summarize its performance and key trends.
- To investigate how different train speeds affect the stability of a railway embankment under rapid drawdown conditions.
- To evaluate the allowable maximum train speed for various drawdown ratios and geometric parameters.

To simplify calculation and simulation, 2-D models assuming an infinitely long tangent track section were used in the analysis. Accordingly, it becomes the main limitation which means curves of the track or any potential change of soil layers along the tracks are not considered. Moreover, any other environmental changes, such as temperature, rainfall, and wind, are not considered as well.

1.3 Research Methodology

The methodology is a critical step in determining the success of a research. In this work, it consists of:

1) FEM-based simulation using RS2 (Rocscience Inc., 2019).

Based on a literature review, key model variables (such as the dimensions of the railway embankment, slope inclination ratios, soil properties, loading due to trains, etc.) can be obtained, which define the model. Then, after generating a basic model, a parametric study of these parameters affecting slope stability was performed using RS2.

2) Parametric study

   Each principal model parameter was investigated separately using a *control variable* method. A comprehensive parametric study of the primary parameters was conducted among three sets of models, including:

   a) Set I: Dry slope model
   b) Set II: Slope model under rapid drawdown condition
   c) Set III: Slope model under both rapid drawdown and moving train loads conditions

   Since the worst case of drainage condition in slope stability turns out to be the undrained condition, this extreme case has been implemented in the models. The parametric study in those three sets of models consists of:

   a) Different drawdown ratios
   b) Variation of slope geometry and subgrade with different moving train loads. This includes the effect of three different parts:
      i. Slope height
      ii. Subgrade height
      iii. Slope inclination

3) Data analysis

   Based on the results obtained by the parametric study for different conditions, a graphical representation helped to better understand the principles of slope stability under these conditions. Also, a chart of maximum safe train speed under different drawdown ratios was developed.

The finite element shear strength reduction (FE-SSR) method was the main method in the analysis to calculate the influence of rapid drawdown on slope stability. Also, the finite element method (FEM) coupled with deformation and seepage was adopted to evaluate the stability due to transient seepage within a slope.

1.4 Thesis Outline

This thesis consists of five chapters. The current chapter presents potential safety problems for railway embankments/roadbeds. Two freight train derailment accidents reveal that the sudden drawdown of water level next to railway tracks could lead to roadbed collapse and slope failure under the train. The objectives and scope of this project are briefly introduced. Finally, the research methodology is illustrated. A concise summary of the remaining chapters is shown below:

Chapter 2 presents a literature review, covering various aspects of slope stability analysis using numerical methods. It begins with a general background of rapid drawdown and a method to analyze behaviors of transient seepage in a slope when a rapid drawdown occurs. Following that, an introduction of railway track structure, loads induced by a moving train on the railway track foundation, and load transfer mechanism are presented to reveal the computation of train loads on a railway embankment. Then, all key dimensional parameters are reviewed for further model generation. Next, some widely used methods in geomechanics for analyzing slope stability are presented and compared, in order to select the most appropriate one for this study. Finally, a review of constitutive models for soils is also presented.

Chapter 3 presents the development of numerical models. With a demonstrated verification, RS2 has been proved to be an effective tool to model both rapid drawdown and train-induced loading.

Chapter 4 presents the analysis of the slope model under different water and loading conditions. Three sets of models were investigated in terms of slope stability and the parametric studies are presented for first two sets of models (Set I and II) to ensure the feasibility of generating models in Set III. Results of the last set of models are also discussed in detail.

Chapter 5 presents conclusions, limitations and recommendation for future studies.

Chapter 2 Literature Review

2.0 Introduction

In the published research work, the rapid drawdown analysis on a slope or a dam has been extensively investigated. However, a specific case combining rapid drawdown with loads due to a passing train on a slope has not been considered yet, which is the main study target of this thesis. This chapter first summarizes background information of the study and lays a foundation for the subsequent two chapters: model establishment and model analysis through the finite element method (FEM). There are five sections in this chapter, and they are organized as follows. Section 2.1 describes the development of rapid drawdown of water level, the theory of transient seepage analysis using FEM and principles of coupled deformation and seepage. Section 2.2 presents the component of the railway track, the method to calculate moving train loads on the railway track foundation, and the load conversion from train wheels to the underlying ties. Section 2.3 demonstrates how key parameters of the model are determined. Section 2.4 reviews popular methods in geomechanics to solve the slope stability problem, and the justification why the FEM has been selected as the optimal method for this study. Moreover, the finite element shear strength reduction method has been proven to be an effective solution for analyzing slope stability. Finally, Section 2.5 describes typical soil constitutive models.

2.1 Analysis for Rapid Drawdown of Water Level

Rapid drawdown occurs when the water level adjoining a slope or an embankment drops relatively quickly, which causes an undrained condition in the slope comprised of low permeability materials (such as clays). It is one of the critical design factors for riverside slopes. Because in this scenario the supporting water load on the slope is removed, leading to larger shear stress within the slope which tends to induce a slope failure.

This section first addresses the development of rapid drawdown in slopes. Then, approaches analyzing transient seepage by the FEM during the rapid drawdown and the theory of coupled solid-fluid interaction used in RS2 are reviewed.

2.1.1 Development of Rapid Drawdown in Slopes

The severe loading condition due to the rapid drawdown could cause a slope failure or instability. Many case histories concerning the total or partial failure of upstream slopes, as summarized by Sherard in 1963, identify rapid drawdown was one of the most important reasons (Sherard et al. 1963). Two stages of rapid drawdown are shown in Figure 2.1. Hydrostatic stresses acting against the slope during the drawdown is shown in Figure 2.1 (a). While Figure 2.1 (b) presents the change of hydrostatic stresses after the drawdown. As shown in Figure 2.1 (a), the initial water table is MO (with a height of H) before the drawdown, so the hydrostatic stresses act on the slope CBO at this stage. Then a drawdown of intensity H_D takes place within a period which finally brings the water level to M'O'. This change of the water level induces a stress difference which has been plotted in Figure 2.1 (b) (Pinyol et al. 2008).

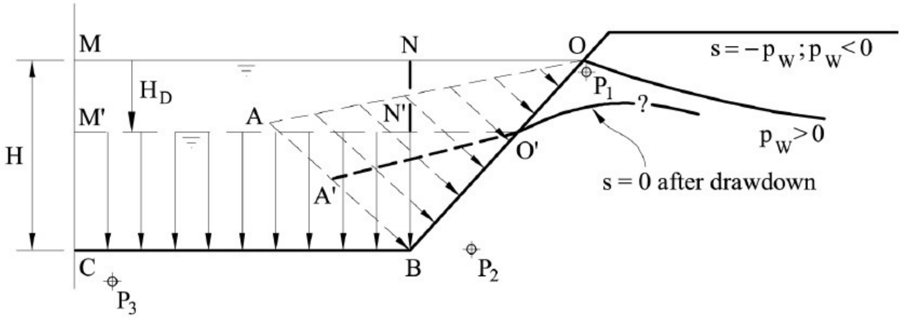

(a)

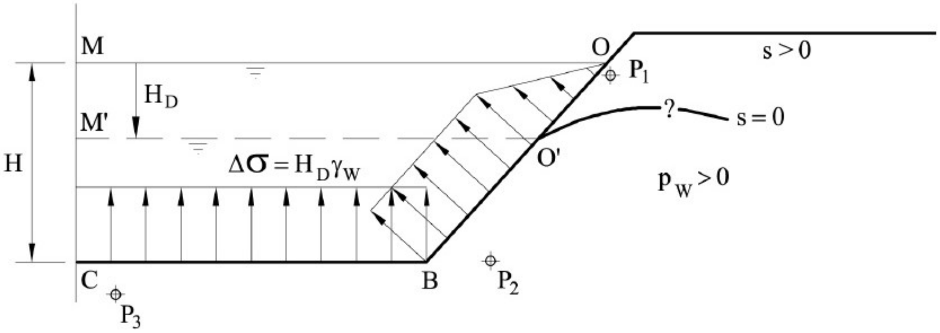

(b)

Figure 2. 1. Drawdown conditions: (a) hydrostatic stresses acting against the exposed slope surface, and (b) change in applied stresses on the exposed boundaries caused by a drawdown of H_D (Pinyol et al. 2008).

The change of total stress boundary results in a new stress distribution in the slope, which will trigger a change of pore pressure. Hopkins et al. (1975) investigated the changes of pore pressures, resultant effective normal forces (summing forces perpendicular to the base of a soil element), and the resultant shear forces (summing forces parallel to the base of a soil element) during the development of a rapid drawdown, which are listed below, while the corresponding graphical explanations are shown in Figure 2.2.

a) Before a rise in water level (Figure 2.2 (a))
  - The pore pressures in the slope: $u_1 = 0$, or < 0 if soils are cohesive and in a semi-dessicated state.
  - The resultant effective normal force:

    $$N_1{}' = N_1 - u_1 = \mathrm{X} H_F \gamma_t \cos i \tag{2.1}$$

    where N_1 is the resultant (total) normal force, X is the width of the soil element, γ_t is the total unit weight, i is the angle formed by a horizontal line and the base of the soil element, and H_F is the height of the soil element.
  - The resultant shear force:

    $$T_1 = X H_F \gamma_t \sin i \tag{2.2}$$

b) High water level (Figure 2.2 (b))
  - The pore pressures in the slope:

    $$u_2 = \gamma_w (H_F + H_W) \tag{2.3}$$

    where γ_w is the unit weight of water, and H_W is the depth of water over the soil element.
  - The resultant effective normal force:

    $$N_2' = N_2 - u_2 = X H_F \gamma_b \cos i \tag{2.4}$$

    where γ_b is the effective unit weight, which means $\gamma_b = \gamma_t - \gamma_w$.
  - The resultant shear force:

    $$T_2 = X H_F \gamma_b \sin i \tag{2.5}$$

c) After rapid drawdown
  i. In cohesive soils (Figure 2.2 (c))
    - The pore pressures in the slope:

$$u_3 = u_2 + \Delta u = \gamma_w(H_F + H_W) - \gamma_W H_W = \gamma_W H_F \tag{2.6}$$

where Δu is the change of pore pressure during the rapid drawdown.

- The resultant effective normal force:

$$N_3' = N_3 - u_3 = XH_F\gamma_b \cos i \tag{2.7}$$

- The resultant shear force:

$$T_3 = XH_F\gamma_t \sin i \tag{2.8}$$

ii. In non-cohesive soils (Figure 2.2 (d))

- The pore pressures in the slope:

$$u_3 = \gamma_w(H_F + H_W) + \Delta u = \gamma_W H_N \tag{2.9}$$

where H_N is as shown in Figure 2.2 (d).

It is noted that the resultant shear force is increasing ($T_3 > T_2$) when the rapid drawdown occurs, because the water tends to flow out of the slope after the rapid drawdown (Hopkins et al. 1975).

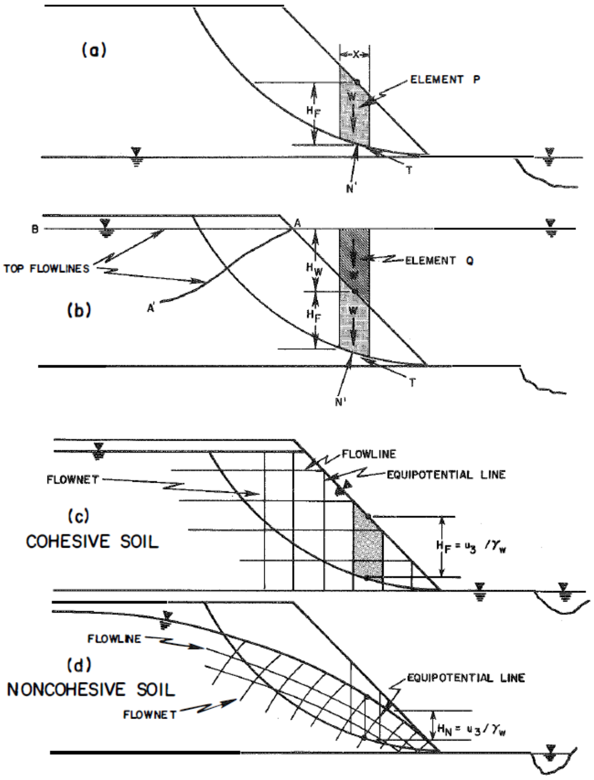

Figure 2. 2. Development of a rapid drawdown scenario: (a) before a rise in the water level, (b) high water level, (c) rapid drawdown in cohesive soils, and (d) rapid drawdown in non-cohesive soils (Hopkins et al. 1975).

2.1.2 Transient Seepage Analysis

In a rapid drawdown condition, the variation of pore water pressure is dependent on the reduction of total stress acting against the slope and the lowered total head. The time-dependent boundary conditions are dynamic when analyzing the pore pressures induced by transient flow, which is considerably different from a steady-state seepage condition. To predict the pore water pressures due to a lowering of the water level, two methods are introduced here:

a) Uncoupled transient seepage analysis

In the 1980s, uncoupled transient seepage analysis based on the FEM was developed to analyze slope stability (Lam et al. 1987; Li and Desai 1983). Although pore pressures are associated with the changes of total stress and head boundary condition, the uncoupled analysis only considers the effect of hydraulic boundary when used to predict pore pressures in slopes after the rapid drawdown.

The governing equation for transient fluid flow in the soil can be understood as a mass balance where the mass of water flowing in or out of a reference volume of soil equals to the change in water mass within the reference volume. So, assuming incompressible water, homogeneous soil, and direction of permeability aligned with the coordinate system, this equation has a form of (Bear 2012):

$$k_h \frac{\partial^2 h}{\partial x^2} + k_v \frac{\partial^2 h}{\partial y^2} = n\frac{dS}{dt} + S\gamma_w m_v \frac{dh}{dt} \tag{2.10}$$

where k_h is horizontal hydraulic conductivity, k_v is vertical hydraulic conductivity, h is the total head, n is porosity, S is water degree of saturation, γ_w is the unit weight of water, and m_v is the coefficient of compressibility.

For saturated conditions (S=1.0), Equation (2.10) then can be simplified as:

$$\frac{k_h}{\gamma_w m_v}\frac{\partial^2 h}{\partial x^2} + \frac{k_v}{\gamma_w m_v}\frac{\partial^2 h}{\partial y^2} = \frac{dh}{dt} \tag{2.11}$$

or

$$c_h \frac{\partial^2 h}{\partial x^2} + c_v \frac{\partial^2 h}{\partial y^2} = \frac{dh}{dt} \tag{2.12}$$

where c_h is the coefficient of consolidation in the horizontal (x) direction, and c_v is the coefficient of consolidation in the vertical (y) direction.

Equation (2.12) indicates that the rate of change in the head in a saturated zone is determined by the coefficients of consolidation. So, in transient seepage analysis, the total heads and pore pressures are dependent on the values of k and m_v with a significant impact on the coefficients of consolidation.

b) Coupled transient seepage analysis

Unlike the uncoupled case, the coupled analysis considers the changes in both stress and pore pressure simultaneously. For rapid drawdown analysis, the importance of pore pressure coupling with total stress has been proved in literature. Pinyol et al. (2008) proposed the fully coupled hydromechanical approach using a finite element program to solve the limits of the current methods for rapid drawdown analysis. In their study, the soil was used as the elastic-plastic Barcelona Basic Model. After comparison, the coupled results were found matching well with the actual measured results. By contrast, the uncoupled results show unrealistic values due to the change of initial pore pressure water during the rapid drawdown (Pinyol et al. 2008). As expected, the coupled analysis of rapid drawdown can provide more accurate results at the cost of consuming more resources, such as time and computer memory (Fredlund et al. 2011).

In the coupled analysis, a number of complex constitutive models have been used to couple changes in pore pressure and changes in total stress boundary conditions while solving the transient seepage equation. In this research, the transient seepage analysis was coupled with the Biot consolidation theory. An elastic-plastic constitutive model (Mohr-Coulomb model) was adopted, which is discussed in detail in Section 2.5.

In the Biot theory, the mechanical behavior of a soil skeleton (Smith et al. 2013) is treated as a porous elastic solid with laminar pore fluid flow coupled with the solid by the conditions of equilibrium and continuity. The coupled Biot equations for a 2-D poroelastic material could be derived through two steps. First, the following 2-D equilibrium equations need to be defined (Smith et al. 2013):

$$\frac{\partial \sigma'_x}{\partial x} + \frac{\partial \tau_{xy}}{\partial y} + \frac{\partial u_w}{\partial x} = 0 \tag{2.13a}$$

$$\frac{\partial \tau_{xy}}{\partial x} + \frac{\partial \sigma_y'}{\partial y} + \frac{\partial u_w}{\partial y} = 0 \tag{2.13b}$$

where σ_x' and σ_y' are the effective stresses $(\sigma - u_w)$, and u_w is the fluid pressure.

Then, Equation (2.13) can be simplified by removing the stress terms in terms of the displacements (Griffiths 1994). This simplification is made based on the assumptions that strains are in-plane and small.

$$\frac{E'(1-v')}{(1+v')(1-2v')}\left[\frac{\partial^2 u^*}{\partial x^2} + \frac{(1-2v')}{2(1-v')}\frac{\partial^2 u^*}{\partial y^2} + \frac{1}{2(1-v')}\frac{\partial^2 v^*}{\partial x \partial y}\right] + \frac{\partial u_w}{\partial x} = 0 \tag{2.14a}$$

$$\frac{E'(1-v')}{(1+v')(1-2v')}\left[\frac{1}{2(1-v')}\frac{\partial^2 u^*}{\partial x \partial y} + \frac{\partial^2 v^*}{\partial y^2} + \frac{(1-2v')}{2(1-v')}\frac{\partial^2 v^*}{\partial x^2}\right] + \frac{\partial u_w}{\partial y} = 0 \tag{2.14b}$$

where E' and v' are the effective elastic parameters, and u^*, v^* are the components of displacement in the x, y directions.

Next, considering 2-D continuity, if the net flow rate is equivalent to the volume rate of change of the soil element, then (Smith et al. 2013):

$$\frac{\partial}{\partial t}\left(\frac{\partial u^*}{\partial x} + \frac{\partial v^*}{\partial y}\right) + \frac{k_x}{\gamma_w}\frac{\partial^2 u_w}{\partial x^2} + \frac{k_y}{\gamma_w}\frac{\partial^2 u_w}{\partial y^2} = 0 \tag{2.15}$$

where k_x and k_y are the material permeabilities in the x- and y-directions.

Equations (2.14) and (2.15) are the coupled Biot equations, which can be interpreted that at a spatial location (x, y) at any time t, the displacements u^*, v^* and excess pore pressure u_w can be predicted. However, due to the dynamic boundary conditions, seepage patterns may not reach a steady state during the simulation.

2.2 Analysis of Moving Loads on the Railway Embankment

Under the external moving loading condition, pore pressure is generated and affects slope stability. When water could not escape from the embankment in a short time, excess pore water pressure is induced, which reduces soil strength (Li et al. 2002). Besides, track foundation failures may occur if there exists a moving wheel load (Li et al. 2002). This section first introduces the railway track structure. Then, moving loads on the railway track foundation will be discussed. Finally, the load transfer mechanism is developed.

2.2.1 Railway Track Structure

As the most fundamental component of the railway infrastructure, the track supports rolling stock by transferring wheel loads from track superstructure to track substructure (Figure 2.3) (Li et al. 2002). Currently, two types of railway tracks are commonly utilized, namely ballasted track and slab track, as shown in Figure 2.4 (Indraratna et al. 2011; Esveld 2001). In comparison, the initial construction cost of a ballasted track is much lower than that of a slab track, being the main limit for slab tracks to be widely used. Nevertheless, a ballasted track tends to deteriorate with the increasing passage of traffic (Esveld 2001). In this thesis, a ballast track is adopted, since it is the prevalent track structure in Canada, and in North America, in general.

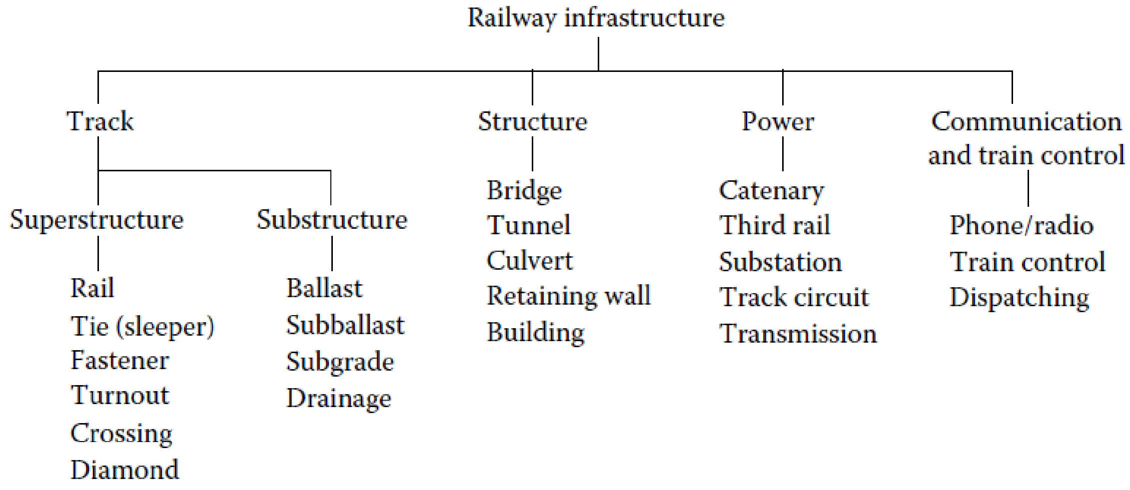

Figure 2. 3. Elements of railway infrastructure (Li et al. 2002).

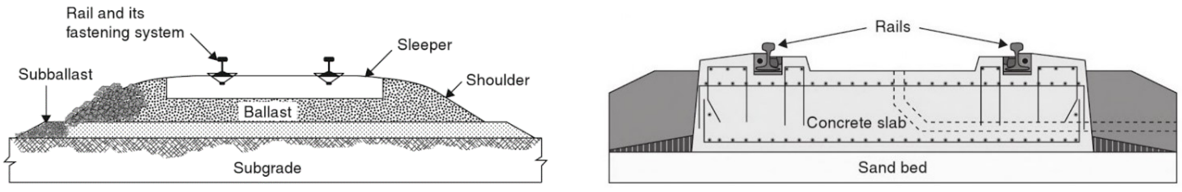

(a) (b)

Figure 2. 4. Cross-section of (a) a ballasted rail track (Indraratna et al. 2011), and (b) a slab track (Esveld 2001).

Ballasted rail track with its track structure components are presented in Figure 2.4 (a), consisting of steel rail, fastening system, timber or concrete sleepers in the superstructure (sleepers – British terminology, cross ties are the corresponding US terminology, however, both are in popular use in North America, so in this thesis both will be used). While the substructure includes natural rock aggregates (ballast), subballast and subgrade (Indraratna et al. 2011). The sleeper-ballast interface separating the superstructure from the substructure is the most important part of the track to distribute the loads to the railway track foundation.

2.2.2 Moving Loads on the Railway Track Foundation

There exist three types of loads which are imposed on the railway track foundation, namely static, cyclic, and dynamic loads (Li et al. 2002). Under a moving train load, shear stresses grow on both horizontal and vertical planes since the principal stresses rotate to withstand the applied load. Figure 2.5 illustrates the stress state on a soil element *a* when a train is approaching.

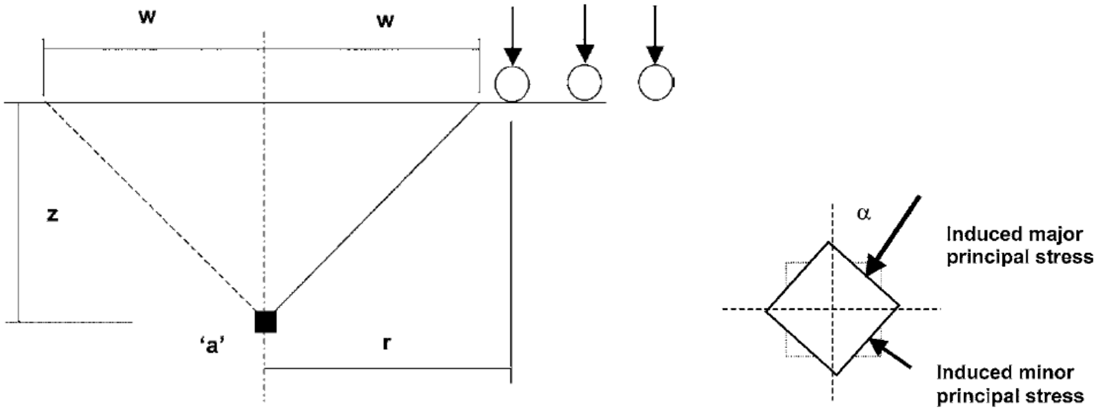

Figure 2. 5. Stress state on a soil element *a* (Wong et al. 2006).

Static loading contains live load and dead loads, induced by the weight of train, track, and subgrade. The weight of train load is distributed to the track and subgrade by the contact points of wheel and rail. The stresses due to the weight of track and subgrade are mainly determined by 1) rail weight which depends on the size of the rail and cross section, 2) sleeper weight which is governed by the type of material and the size of tie, and 3) the weight of track substructure (ballast, subballast, and subgrade) which relies on the material type and can be estimated by Equation (2.16) (Li et al. 2002).

$$w = \gamma \cdot z \tag{2.16}$$

where w is the weight of track substructure per unit area (kg/m^2), γ is the unit weight of the material (kg/m^3), and z is the depth of track substructure (m).

Cyclic loading is a type of repeated loading generated by the train passing on the railway track. Undergoing millions of loading cycles, the soils deform non-elastically in response (Jiang et al. 2016). Especially, the residual settlements accumulate after every cycle of train loading (Frost et al. 2004; Lekarp and Dawson 1998). The character of cyclic loading depends on the shape, duration, magnitude of loading pulse, time interval between consecutive pulses, and the total number of loading pulses. The duration of loading pulse is determined by the operating speed of the train and the depth of consideration which can be evaluated by Equation (2.17) (Li et al. 2002).

$$t_p = \frac{L}{V} \tag{2.17}$$

where t_p is the time duration of loading pulse, V is the train speed, and L is the influence length of an axle load or adjacent axle loads for a given depth of ballast or subgrade.

Suiker et al. (2005) studied the triaxial testing of ballast and subballast materials which are common materials for a railway track substructure. The results showed the cyclic loading can lead to an increase in the material strength and stiffness. The permanent deviatoric deformations due to cyclic loading mainly depend on the stress ratio (the ratio of minimum stress to maximum stress). Also, the permanent volumetric deformation is determined by both stress ratio and hydrostatic pressure (Suiker et al. 2005).

Dynamic loads or impact loads are induced by wheel or rail abnormalities such as wheel-flats, wheel-shells, dipped rails, turnouts, crossings, insulated joints, expansion gaps between two rail segments, imperfect rail welds and rail corrugations (Indraratna et al. 2011). Dynamic loading is either short duration force with no reaction time for the vehicle suspension and track foundation or longer duration load with enough time for the dynamic wheel loads to be transmitted into the track substructure (Li et al. 2002).

2.2.3 Load Transfer Mechanism

Wheel loads applied to the rail are transferred by the wheel to rail, sleepers, ballast, subballast and eventually, subgrade. Figure 2.6 (a) shows the load transfer model which assumes the distribution of vertical stress is uniform in the substructure. While Figure 2.6 (b) illustrates a modified spread model induced by a 2-axle rolling stock (Zhang et al. 2016).

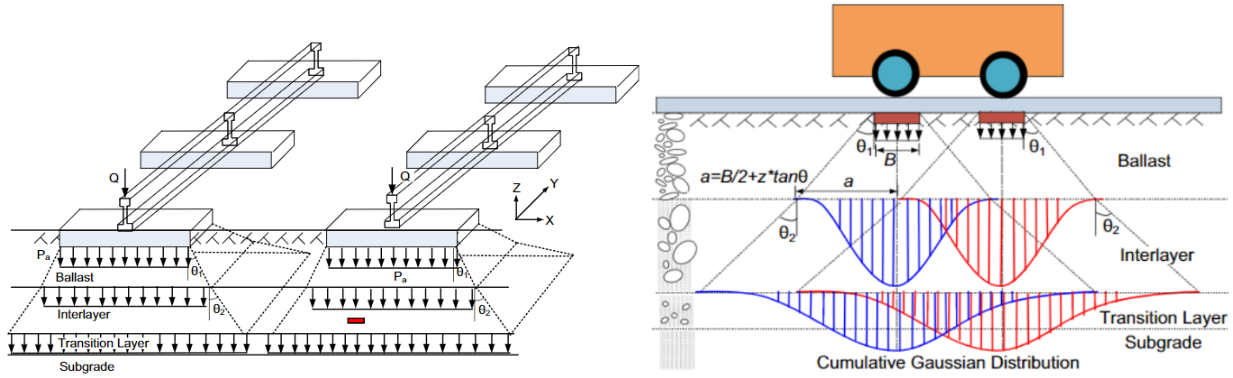

Figure 2. 6. (a) Load spread model, and (b) modified load spread model (Zhang et al. 2016).

Although various methods have been developed to determine the maximum vertical stress for a plane strain situation on the subgrade, the load distribution method proposed by AREMA (2010) in the Manual for Railway Engineering is adopted in this research, since it is the governing standardization body for North American railways. Since the simulation software RS2 is geared towards rock and soil applications, forces due to the rolling stock and rails on the timber sleepers need to be calculated manually and applied as an external load. The equations to calculate tie-to-ballast pressure includes (AREMA 2010):

a) Impact factor

The most common method to determine the design dynamic wheel load is to increase the static wheel load by a dynamic load factor or impact load factor. Thus, the impact factor needs to be obtained first. Since the train speed affects the stress placed by the wheel load on a sleeper (cross tie), the impact factor (IF) for the track is determined by Equation (2.18).

$$IF = \frac{33V}{100D} \tag{2.18}$$

where V is velocity (mi/h), and D is the diameter of the wheel (in).

b) Distribution factor

The distribution of load is also dependent on tie and axle spacing, and the percentage of the wheel-to-rail load carried by an individual tie varies from location to location. Figure 2.7 shows that the percentage axle load carried by a single tie as a function of the center to center tie spacing.

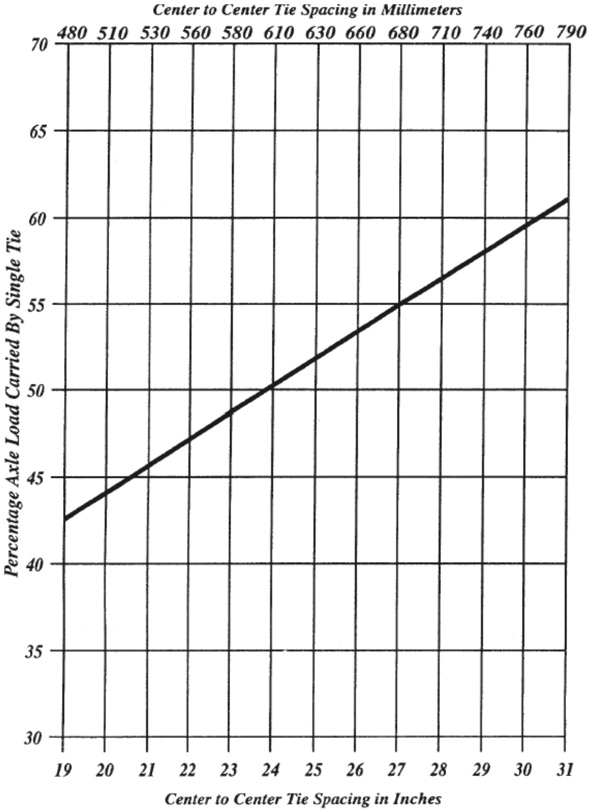

Figure 2. 7. Estimated distribution of loads (AREMA 2013).

c) AREMA formula for average ballast pressure at tie face

Considering tie-to-ballast pressure usually is not evenly distributed across or along the bottom of a cross tie, a method to calculate the average pressure at the bottom of the tie is proposed as an approximation. This average pressure is associated with axle load, modified by distribution, impact factors, and the bearing area of the tie. The calculation of Average ballast pressure (ABP) is expressed below:

$$ABP = \frac{(2F)[1+\frac{IF}{100}](\frac{DF}{100})}{A} \tag{2.19}$$

where F is wheel load in pounds (kN), IF is impact factor in percent, DF is distribution factor in percent, and A is bearing area of cross ties in square inches (millimeters). It is noted that the corresponding unit of ABP is psi (MPa).

2.3 Key Parameters of the Model

It is important to identify key parameters of a system in order to create a reasonable model representing physical reality. The main goal of this section is to determine these key parameters and their credible ranges. There are four main components in the model: 1) the freight train, 2) the rail system, 3) the foundation, and 4) the condition of the waterway affected by the rapid drawdown of water level. Therefore, these key parameters are discussed in detail including the size of freight trains, the magnitude of moving loads, the dimension of railway embankments, slope inclination ratios, and soil/material properties.

2.3.1 Parameters for Freight Trains

Parameters for a freight train include the quantity and weight of axles and reasonable operating speeds. Table 2.1 shows both empty and loaded axle loads, which are applied on the rail and the number of axles for different typical train types. The diameter (d) range of railway wheels is from 27 inches (685.8 mm) to 39 inches (990.6 mm) (Leonard 1971). For a freight car, the typical diameter of wheels is 920 mm (Johansson 2006). In North America, a freight car is usually supported by two trucks with two axles per truck as shown in Figure 2.8. All the dimensional parameters describing this freight car are listed below.

Table 2. 1 Number of axles and weight per axle of several types of rolling stock (Esveld 2001; Dick 2016)

	number of axles	empty	loaded
trams	4	50 kN	70 kN
light-rail	4	80 kN	100 kN
passenger coach	4	100 kN	120 kN
passenger motor coach	4	150 kN	170 kN
locomotive	4 or 6	215 kN	/
freight wagon	2	120 kN	225 kN
heavy haul (USA, Australia)	4	120 kN	250-350 kN

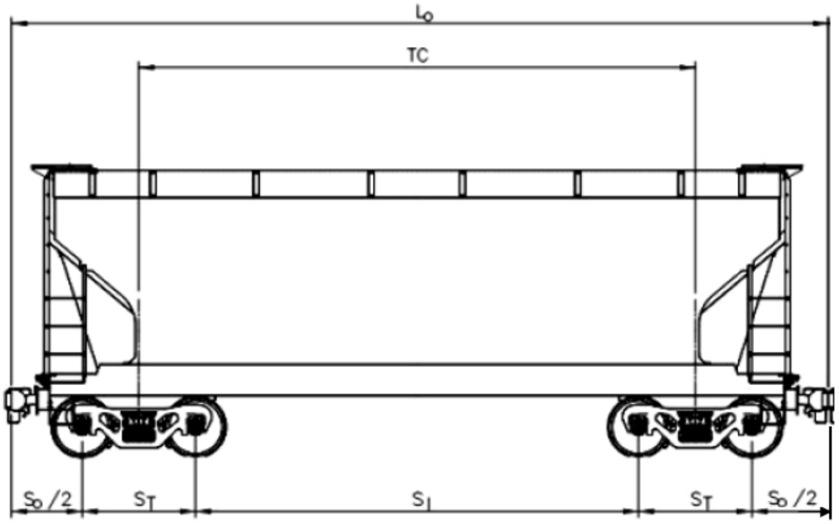

L_O = overall length of railroad car measured over the pulling face of the coupler,
TC = length between the center pin on the trucks, known as the truck center distance,
S_I = inboard axle spacing, the distance between the inside axles of the railroad car,
S_O = outboard axle spacing, the distance between the outside axles of the railroad car, and
S_T = truck axle spacing, the distance between the adjacent axles of a truck.

Figure 2. 8. Typical railcar dimension for a standard freight car used in North America (Dick 2016).

The units of maximum speed will be presented in km/h. The speed of a typical freight train varies from 30 km/h to 120 km/h, which is given in Table 2.2.

Table 2. 2 Maximum speeds for railways (Esveld 2001)

	passenger trains (km/h)	freight trains (km/h)
branch lines	/	30-40
secondary lines	80-120	60-80
main lines	160-200	100-120
high speed lines	250-300	/

Based on the parameter values of freight trains in North America listed in Tables 2.1 and 2.2, the freight train in this study is considered as a train with 4 axles per car, 36 000 lbs (160 kN) for each axle (loaded). While the maximum train speed is limited to 120 km/h for freight trains on a main line.

2.3.2 Parameters for Railway Track Structure

This subsection summarizes the parameters of both superstructure (e.g. track gauge, sleeper (British terminology, in the US it is referred to as cross tie) dimensions, sleeper spacing and their material properties) and substructure (e.g. the thickness of each layer, the slope geometry and material properties of each layer).

a) Superstructure

Table 2.3 gives representative values of track gauge in different countries. Most rails have been laid at 1435 mm, which is the standard gauge (4ft 8.5in) (Profillidis 2014).

Table 2. 3 Rail gauge values (Selig and Waters 1994)

Location	Gauge (mm)	Gauge (in.)
North America	1435	56.5
Europe	1435-1668	56.5-65.7
South Africa	1065	41.9
Australia	1524-1676	42-63
China	1435	56.5

The definition of the track gauge is the distance between the inner sides of the rails, which is measured 14 mm below the rolling surface, as shown in Figure 2.9 (Profillidis 2014).

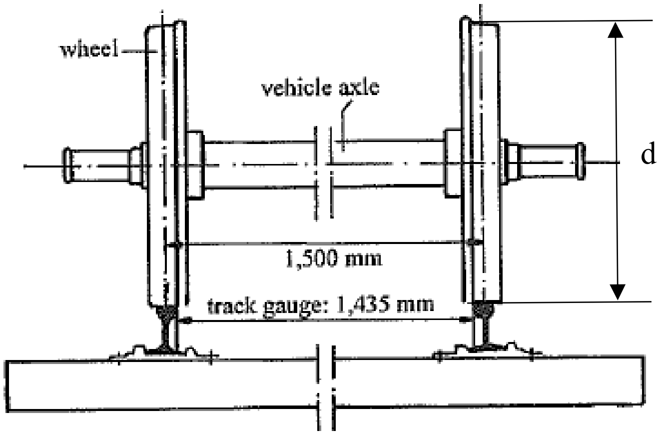

Figure 2. 9. Wheel of the railway freight car with a standard gauge track (Profillidis 2014)

The commonly used sleeper sizes and sleeper spacing are classified in Table 2.4. Figure 2.10 (a) illustrates the geometric characteristics of wood (or timber) sleepers with standard track gauge in Europe, and (b) is a corresponding diagram of timber sleepers with dimensions specified.

Table 2. 4 Typical sleeper dimensions (Selig and Waters 1994)

Location	Material	Width (mm)	Length (mm)	Spacing (mm)
Australia	Wood	210-260	2000-2743	610-760
	Concrete	/	/	600-685
China	Wood	190-220	2500	543-568
	Concrete	240-290	2500	568
Europe	Wood	250	2600	630-700
	Concrete	250-300	2300-2600	692
North America	Wood	229	2590	495
	Concrete	286	2629	610
South Africa	Wood	250	2100	700
	Concrete	203-254	2057	700
		230-300	2200	600

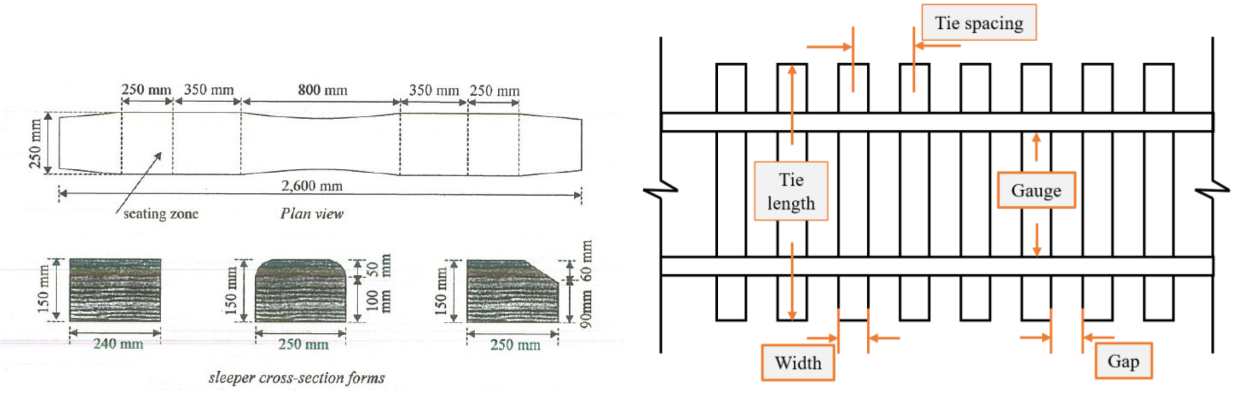

(a) (b)

Figure 2. 10. (a) Geometric characteristics of timber sleepers with standard track gauge (Profillidis 2014), and (b) diagram of timber sleepers.

Besides geometric parameters, material properties are also the important factors which need to be considered as well. It can be seen from Table 2.5 that a timber sleeper appears to be a better material in terms of tensile and compressive strengths compared to concrete sleepers.

Table 2. 5 Values of the mechanical characteristics of superstructure materials (Profillidis 2014)

Material	Elasticity modulus (MPa)	Poisson's ratio	Tensile strength R_T (MPa)	Compressive strength R_C (MPa)
Reinforced-concrete sleeper	2.94×10^4	0.25	2.94	29.42
Prestressed-concrete sleeper	4.90×10^4	0.25	5.88	8.83
Tropical timber sleeper	2.45×10^4	0.25	9.81	98.07
Rail (steel)	2.06×10^5	0.30	686.47	588.40

For the parameters of superstructure, the rail gauge is 1435 mm, and the timber sleeper is 229 mm in width, 2590 mm in length, and 495 mm in spacing. The mechanical characteristics of timber sleepers in this study are used as shown in Table 2.5.

b) Substructure

AREMA's Manual for Railway Engineering (AREMA 2010) recommends the range of geometry parameters for substructure. The minimum ballast thickness is 12 inches (304 mm) recommended for standard gauge (1435 mm). While the ballast shoulder width of not less than 12 inches (304 mm) is recommended. The subballast depth varies from 100 mm to 150 mm (Indraratna et al. 2011). The subgrade may be natural soil or fill material whose thickness is usually over 2000 mm (Egeli and Usun 2012).

Table 2. 6 Parameters of railway embankments (Xue and Zhang 2014)

Name	Unit weight (kN/m^3)	Compression modulus (MPa)	Poisson's ratio	Cohesion (kPa)	Internal friction angle (°)	Damp. Ratio
Upper layer of formation	19.5	190	0.3	32	75	0.08
Lower layer of formation	19	100	0.3	26	25	0.07
Embankment below formation	18.5	85	0.28	25	22.3	0.1

Table 2. 7 Values of the mechanical characteristics of subgrade materials (Profillidis 2014)

Material	Elasticity modulus (kp/cm^2)	Elasticity modulus (MPa)	Poisson's ratio	Cohesion (kp/cm^2)	Cohesion (kPa)	Friction angle (°)
Poor quality subgrade	125	12.26	0.4	0.15	14.71	10
Medium quality subgrade	250	24.52	0.3	0.1	9.81	20
Good quality subgrade	800	78.45	0.3	0	0.00	35
Rock subgrade	3.0×10^4	2942.00	0.2	15	1471.00	20
Ballast	1300	127.49	0.2	0	0.00	45
Gravel subballast	2000	196.13	0.3	0	0.00	35
Sand	1000	98.07	0.3	0	0.00	30

Note: 1kp/cm^2 = 98.067 kPa = 0.098 MPa

Material properties of railway embankments are displayed in Table 2.6. Both upper and lower layers of formation are listed, and the embankment below the formation is included as well. While the mechanical characteristics of subgrade materials are discussed in Table 2.7, including different quality types of subgrades.

Several typical values of hydraulic conductivity of saturated soils are presented in Table 2.8. It mainly discusses the drainage performance of different soils often used in the construction of railway embankments.

Table 2. 8 Typical values of hydraulic conductivity of saturated soils (Budhu 2008)

Soil type	k (cm/s)
Clean gravel	>1.0
Clean sands, clean sand, and gravel mixtures	1.0 to 10^{-3}
Fine sands, silts, mixtures comprising sands, silts, and clays	10^{-3} to 10^{-7}
Homogeneous clays	$<10^{-7}$

AREMA’s Manual for Railway Engineering recommends a typical slope inclination of 2H:1V (AREMA 2010). But other ratios are also accepted in some studies. The inclination of a ballast slope may be different from that of subballast and subgrade slope, which can be seen in Table 2.9.

Table 2. 9 Values of slope inclination (Calamak and Yanmaz 2016; Egeli and Usun 2012; Profillidis 2014)

Name	Horizontal: Vertical		
Ballast slope	3:2	2:1	2:1
Suballast and subgrade slope	3:2	3:1	2:1

2.3.3 Soil Properties of Foundation Soil Mass

For the foundation soil mass, soil properties are mainly represented by their unit weight, cohesion, internal friction angle, Young’s modulus, and Poisson’s ratio. Table 2.10 shows typical values of unit weight, cohesion and internal friction angle of sand and clay soils. The cohesion of clay could vary from 12.5 kPa to 200 kPa due to different water contents, while sand has negligible cohesion.

Table 2. 10 The typical values of unit weight, cohesion and internal friction angle for sand and clay soils (Chang and Zhang 2006; Peck et al. 1974)

Name		Unit weight (kN/m^3)	Cohesion (kPa)	Internal friction angle (°)
Sand	Very loose sand	11.5-16.5	0	<29
	Loose sand	14.8-19.0	0	29-30
	Medium sand	18.1-21.4	0	30-36
	Dense sand	18.1-23.1	0	36-41
	Very dense sand	21.4-24.7	0	>41
Clay	Very soft clay	15.0-16.0	12.5	<3
	Soft clay	16.0-17.0	25	3-5
	Medium clay	17.0-18.0	50	4-9
	Stiff clay	18.0-19.0	100	8-16
	Very stiff clay	19.0-20.0	200	15-25
	Hard clay	20.0-22.0		>25

To simplify the calculation in further work, the unit weight uses metric units (kN/m^3) instead of the imperial system (lb/ft^3). The conversion of the units is 1 lb/ft^3=0.165 kN/m^3. Young's modulus (E) or shear modulus (G) and Poisson's ratio describe the elasticity of materials. The typical values of E and G of different soils under the drained condition and the Poisson's ratios of soils are shown in Table 2.11 and Table 2.12, respectively.

Table 2. 11 Typical values of E and G (Budhu 2008)

Soil type		E^a (MPa)	G* (MPa)
Clay	Soft	1-15	0.5-5
	Medium	15-30	5-15
	Stiff	30-100	15-40
Sand	Loose	10-20	5-10
	Medium	20-40	10-15
	Dense	40-80	15-35

Table 2. 12 Approximate values of Poisson's ratio of soils (Rowe 2012)

Soil	Poisson's ratio
Saturated soil, undrained loading	0.5
Clay, drained loading	0.2-0.4
Dense sand, drained loading	0.3-0.4
Loose sand, drained loading	0.1-0.3
Peat, drained loading	0-0.1

2.4 Slope Stability Analysis Methods

Stability analysis and deformation analysis are two critical calculations in geotechnical designs (Terzaghi 1951). The former one determines if geotechnical structures are safe and stable. While the latter one gives information if the deformation of a geotechnical structure under working loads is excessively large or not. The stability of a slope could be analyzed in several different ways, such as using the limit equilibrium method (LEM), and various numerical methods (Cheng and Lau 2014), which will be briefly introduced as follows.

2.4.1 Limit Equilibrium Method

The Limit Equilibrium Methods (LEMs) are the most popular and simplest approaches for slope stability analysis. The idea of LEMs is to find a factor of safety (FS) for a slope which can be represented by the ratio of shear strength and shear stress within a soil (Equation (2.20)) (Cheng and Lau 2014).

$$FS = \frac{Shear\ strength\ of\ the\ soil}{Shear\ stress\ in\ the\ soil\ mass} \tag{2.20}$$

The calculation of LEMs is based on 1) the existence of a slip surface assumption and 2) the static equilibrium for the entire failing soil mass (e.g. Swedish circle ($\phi_u = 0$) method (Fellenius 1922)) or the slices which are smaller blocks of failing soil mass (e.g. ordinary method of slices (Fellenius 1927)).

2.4.2 Numerical Methods

In geomechanics, numerical methods have been widely used because they can take advantage of the available computing power to solve complex models representing geomaterials which are otherwise unsolvable. In particular for slope stability analysis, being the topic of this thesis, one of the numerical methods will be used extensively. Currently, there are multiple popular numerical methods to evaluate slope behavior. Therefore, this part briefly reviews the frequently-used numerical methods in geomechanics, including Discrete Element Method, Boundary Element Method, Finite Difference Method, and Finite Element Method.

a) Discrete Element Method (DEM)

The DEM is one of the discontinuum methods (Luding 2008), which simulates the domain by the microscopic understanding of macroscopic particulate material behavior (Herrmann 1997; Hinrichsen and Wolf 2006). Particularly, this method is designed to deal with contact conditions for a mass of irregular particles (Munjiza 2004). The interaction force is associated with the overlap δ of two particles (Figure 2.11 shows how to evaluate the deformations of particles (Luding 2008)).

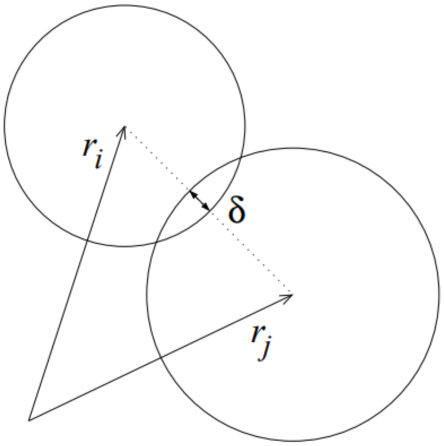

Figure 2. 11. Two particles in contact with overlap δ.

The DEM technique features three different aspects: (1) the representation of contacts, (2) the representation of solid material, and (3) the scheme which is used to detect and update the set of contacts (Cundall and Hart 1992).

b) Boundary Element Method (BEM)

Different from the DEM, all the remaining methods (the BEM, the FDM, and the FEM) discussed in this and subsequent sections belong to continuum methods. In spite of all classified into continuum methods, the discretization of the BEM is different from both the FDM and the FEM. The BEM solves a boundary integral equations only related to boundary values (Hall 1994). Thus, in the BEM, only the boundaries of the domain are discretized (Figure 2.12), while the entire medium and boundaries need to be divided in both the FDM and the FEM (Bobet 2010). This method evolved from the beginning with different names such as ‘the boundary integral equation method’, ‘panel method’, ‘integral equation’, etc. in the 1960s, then the name was changed to ‘BEM’ in 1975 (Banerjee and Wilson 2005).

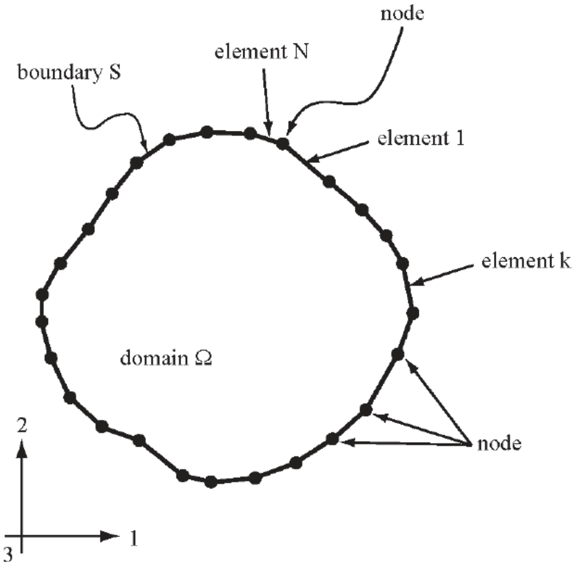

Figure 2. 12. Discretization in BEM (two dimensions) (Bobet 2010)

Compared to FEM and FDM, the BEM has some advantages (Costabel 1987). For example, only the discretization of a domain boundary is considered in the BEM, and it is easy to handle the exterior problems with unbounded domains but bounded boundaries. However, there are still some challenges of the BEM, such as angular boundaries, appropriate boundary integral equations, causing large and dense matrices to be solved, etc. (Costabel 1987).

c) Finite Difference Method (FDM)

The FDM is the oldest numerical method used in geomechanics for solving differential equations involving derivatives which represent the rates of changes in the variables (Desai and Christian 1979). According to Timoshenko and Goodier's study, the FDM was first developed by Runge in 1908 for torsion problems in solid mechanics (Timoshenko and Goodier 1982). Particularly, Desai first used FDM for geotechnical problems in 1977 (Desai and Christian 1979). As an example, the FDM solving the problem on a grid superimposed on a domain is shown in Figure 2.13 (Bobet 2010).

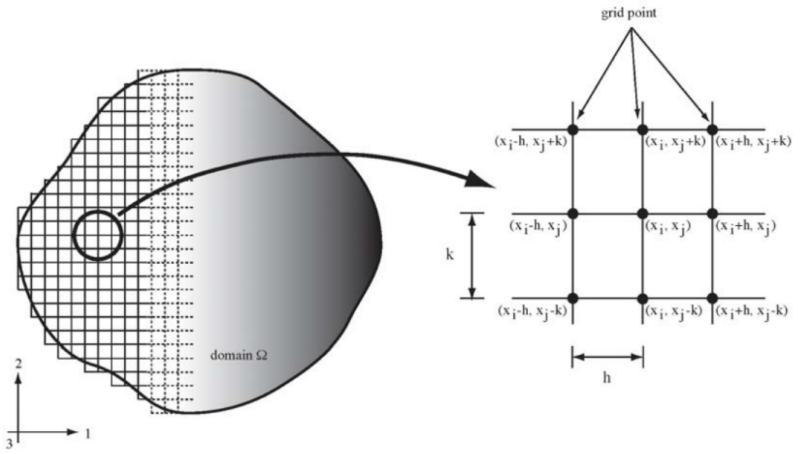

Figure 2. 13. Finite difference grid (two dimensions) (Bobet 2010).

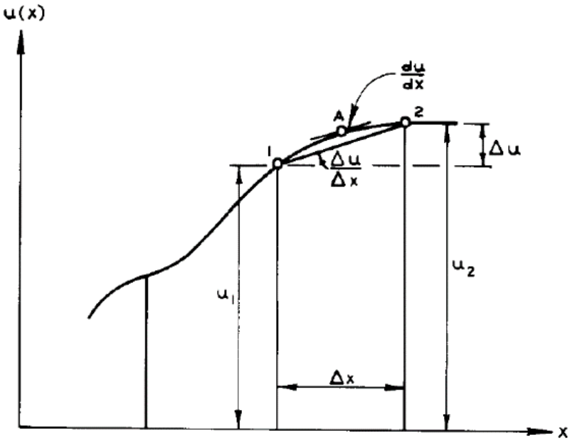

Figure 2. 14. Finite difference approximation to the first derivative (Desai and Christian 1979).

In Figure 2.14, the principle of FDM can be depicted by the following Equation (2.21) in which the differential equation $\frac{du}{dx}$ is converted into the difference equation $\frac{\Delta u}{\Delta x}$ (Desai and Christian 1979).

$$\frac{du}{dx} = \lim_{\Delta x \to 0} \frac{\Delta u}{\Delta x} \approx \frac{\Delta u}{\Delta x} \tag{2.21}$$

After the replacement, three basic approximations to the first derivative could express the differentials of a function u(x):

- Forward difference $$\frac{du}{dx} = \frac{u_{i+1,j} - u_{i,j}}{\Delta x} + O(\Delta x) \tag{2.22}$$
- Backward difference $$\frac{du}{dx} = \frac{u_{i,j} - u_{i-1,j}}{\Delta x} + O(\Delta x) \tag{2.23}$$

- Central difference $$\frac{du}{dx} = \frac{u_{i+1,j} - u_{i-1,j}}{2\Delta x} + O(\Delta x)^2 \qquad (2.24)$$

It is noted that the FDM can solve time-dependent problems (Nikolić et al. 2016) and handle complicated nonlinear material behavior well, such as laterally loaded piles, one-dimensional consolidation, two- and three-dimensional seepage (Bobet 2010; Desai and Christian 1979). However, it is difficult to obtain finite difference equations to clarify the variations of material properties for nonhomogeneous materials. The difficulty in modeling arbitrarily shaped domains is also the most important shortcoming of this method (Desai and Christian 1979). When the configuration of a domain is simple (e.g. rectangular), the mesh points are able to be adjusted to coincide with the boundaries. But for an irregular boundary, the mesh points may not fall on the boundary. Therefore, it is necessary to improve the FDM to deal with these shortcomings.

d) Finite Element Method (FEM)

The FEM has been used beyond the field of geotechnics. With powerful capacity, it is widely applied in electromagnetic, mechanical and aerospace areas. In our community, it is often used in geotechnical problems with continuous or quasi-continuous media. The FEM was first proposed by Clough (1960). Then, FEM was used to solve a variety of engineering problems in the late 1960s and early 1970s (Cook 2007). In this method, both the boundary and interior region are discretized into small finite elements which are reconnected by lines at the nodes as shown in Figure 2.15 (Bobet 2010). Although the nodal points can be located along or inside the subdivided mesh, they are always at the intersecting mesh lines (Akin 2005).

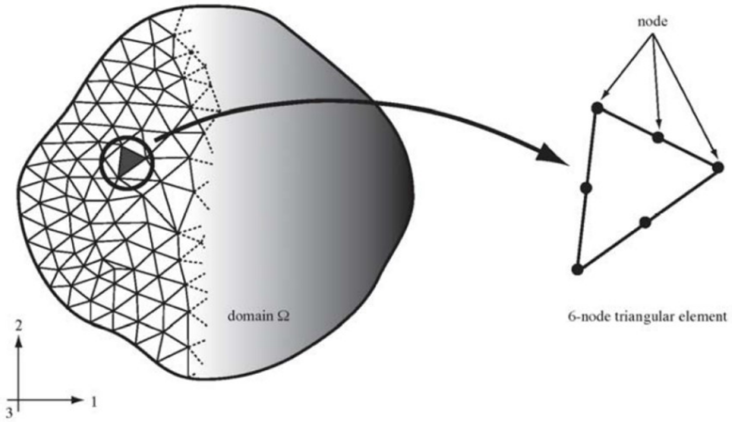

Figure 2. 15. Finite element discretization (two dimensions) (Bobet 2010)

The FEM is an integral equation in terms of its mathematical concept (Akin 2005). So, the typical FEM procedure can be summarized by the following steps (Desai and Christian 1979).

i. Element discretization: divide the domain into smaller finite elements including the nodes on the element boundaries or within an element.

ii. Primary variable approximation: select a primary variable (e.g. displacements, stresses, etc.) and compute by approximation functions (e.g. displacement functions, interpolation functions, etc.).

iii. Element equations derivation: derive element equations to define properties of a finite element in Equation (2.25).

$$[K_E] \cdot \{\Delta d_E\} = \{\Delta R_E\} \tag{2.25}$$

where $[K_E]$ is the element stiffness matrix, $\{\Delta d_E\}$ is the vector of incremental element nodal displacements, and $\{\Delta R_E\}$ is the vector of incremental element nodal forces.

iv. Global equations assembly: combine the element properties to obtain global equations, which is to reach a stiffness relation for the entire system:

$$[K_G] \cdot \{\Delta d_G\} = \{\Delta R_G\} \tag{2.26}$$

where $[K_G]$ is the global stiffness matrix, $\{\Delta d_G\}$ is the vector of all incremental element nodal displacements, and $\{\Delta R_G\}$ is the vector of all incremental element nodal forces.

v. Boundary conditions modification: adjust the global equations by the boundary conditions (e.g. loading effect, displacement effect)

vi. Computation of primary and secondary quantities. It consists of two steps:

  - Determine the nodal displacement by solving simultaneous linear algebraic equations.
  - Obtain element strains through the nodal displacements and the element displacement field interpolation, then calculate the stresses from strains.

2.4.3 Advantages of FEM in Slope Stability Analysis

The FEM is a numerical method aimed at solving the governing partial differential equation by dividing the model domain into small and simple parts and interpolating the solution over them. When comparing with traditional LEMs, FEM has advantages of (Griffiths and Lane 1999):

- Assumptions of the shape and location of the failure surface are not necessary anymore.
- Slice concept does not exist in this method, thus inter-slice force assumption/analysis is not required.
- More information can be provided in practical soil compressibility analysis, such as deformations of stress levels.
- Real-time analysis of progressive failure and overall shear failure is possible.

In terms of the applicability to solve geotechnical problems, the FEM also brings several distinct benefits among the numerical methods: 1) simulating slopes with a high similarity of actual situations (such as complex geometry, sequences of loading, presence of material for reinforcement, action of water, and laws for complex soil behavior), 2) easily observing the deformations of soils in the contours from the analysis output (Matthews et al. 2014). However, the long processing time to create a model and perform the analysis is the potential limits of the FEM approach (Cheng et al. 2007).

Due to the aforementioned advantages, the FEM is selected as the method in this work for the slope stability analysis. The FS is a significant factor quantifying slope stability, in other words, how far a slope is from failing. To obtain FS using FEM, the shear strength reduction (SSR) technique must be employed because the finite element analysis is applied to compute stresses and displacement, which could not directly determine the stability of a slope. SSR technique can predict the development of shear strain, reflecting the potential failure zone of a slope. It also allows users to visualize the development of how a slope fails (Hammah et al. 2005a).

2.4.4 Finite Element Shear Strength Reduction Method

This section focuses on the finite element shear strength reduction (FE-SSR) approach and its application to calculate the factor of safety (FS).

The SSR technique was first applied for slope stability analysis by Zienkiewicz et al. (1975) as early as 1977. After that, many researchers applied the SSR technique for their research studies, such as Naylor (1982), Donald and Giam (1988), Matsui and San (1992), Ugai and Leshchinsky (1995), Dawson et al. (1999), Griffiths and Lane (1999), Song (1997), Zheng et al. (2005) and others. Among these studies, one milestone is that SSR approach was verified by Matsui and San (1992) in the finite element slope stability analysis. So far FE SSR method has been used to deal with a wide range of problems, such as stability problems in blocky rock masses (Hammah et al. 2007a), and determination of serviceability-based slope FS (Hammah et al. 2007b).

The FE SSR analysis obtains the FS of a slope by gradually reducing the shear strength of the soil material and simultaneously calculating deformations by the FEM until non-convergence of solutions occurs (Matsui 1988), while the FS could have more than one definition (Abramson et al. 2002). In two-dimensional finite element slope stability analysis, there are two commonly used definitions (Kainthola et al. 2013): 1) the strength reserving definition which considers the FS as the factor where the shear strength of the soil would have to be divided to bring the slope into the state of critical equilibrium (Duncan 1996), and 2) the overloading defining the FS as the ratio of total resisting forces to the total driving forces along a certain slip line (Farias and Naylor 1998).

The strength reserving definition is considered because the SSR technique is usually used to obtain the FS based on it (Dawson et al. 1999; Griffiths and Lane 1999). In FE-SSR approach, the FS is determined by searching for a series of strength reduction factors (SRFs) using finite element analysis until the ultimate state of the system is attained, and the corresponding SRF is the FS for the slope. Moreover, this method usually relies on the Mohr-Coulomb strength models of materials, though other constitutive models are feasible as well. Then, the reduced shear strength material parameters (c^* and $\emptyset^*$) are defined as (Cheng and Lau 2014)

$$c^* = \frac{c'}{F}\ ; \quad \emptyset^* = \arctan\left(\frac{tan\emptyset'}{F}\right) \tag{2.27}$$

where c' and $\emptyset'$ are the shear strength parameters, and F is the SRF.

The reduced shear strength for a Mohr-Coulomb material is demonstrated in the following equation:

$$\frac{\tau}{F} = \frac{c'}{F} + \frac{\sigma tan\emptyset'}{F} \tag{2.28}$$

where τ is the shear strength, and σ is the normal stress.

Which can also be expressed as

$$\frac{\tau}{F} = c^* + \sigma tan\emptyset^* \tag{2.29}$$

There are three main steps to determine the FS (or critical SRF) of a slope by FE-SSR method (Hammah et al. 2007a):

i. Create a slope model by FEM with the initial properties, compute the model, and record the maximum total displacement.
ii. Raise the value of SRF (or F in Equation (2.28)), figure out the new shear strength parameters, assign the new strength properties to the model, re-compute the model, and record the maximum total displacement.
iii. Repeat 2, and terminate the calculation if the situation requires one of the following situations (Cheng and Lau 2014):
    - The non-linear equation solver does not converge when reaching user-defined maximum iterations.
    - Displacement in the system grows dramatically in a short time.
    - The mechanism to explain the failure has been established.

Especially, the contour of the maximum shear strain or the maximum shear strain rate shows the developing failure mechanism of the slope (Cheng and Lau 2014). Figure 2.16 (a) shows the contours of maximum shear strain for a failed slope, and (b) defines the location of critical failure surface in the slope by FE-SSR method.

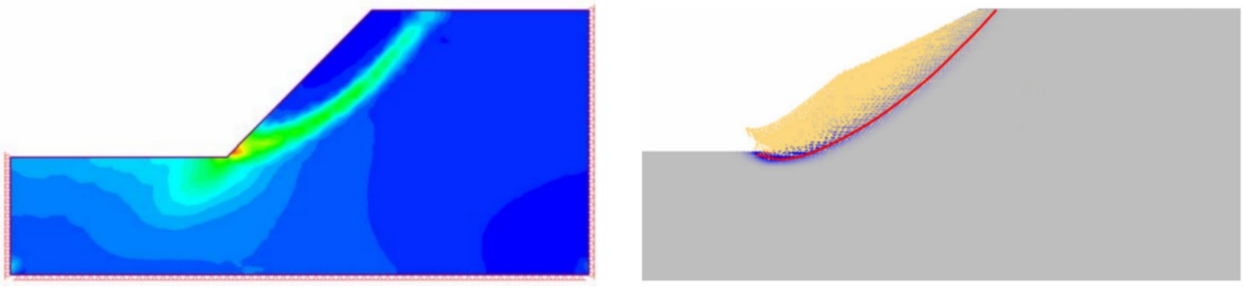
(a) (b)

Figure 2. 16. (a) Contour of maximum shear strain (Hammah et al. 2005b), and (b) failure mechanism by FE-SSR method (Cheng et al. 2007)

2.4.5 Convergence Criteria

Several different criteria can be used to evaluate the convergence of FE analysis, such as the limiting of the shear stresses on the potential slip surface (Duncan and Dunlop 1969), non-convergence solution (Zienkiewicz et al. 1977), or some test of bulging of the slope (Snitbhan and Chen 1976). Once non-convergence occurs, it actually stands for slope failure. Although the convergence of the simulation is complicated, its solution process, convergence and stopping criterion used in RS2 can be expressed as a simple non-linear spring with a single force applied on it. The relationship between the applied load P and displacement U is shown below:

$$P = KU \tag{2.30}$$

where $K(U)$ is the stiffness of the spring and is a non-linear factor dependent on displacement. The curve shown in Figure 2.17 presents the response of the spring to loads.

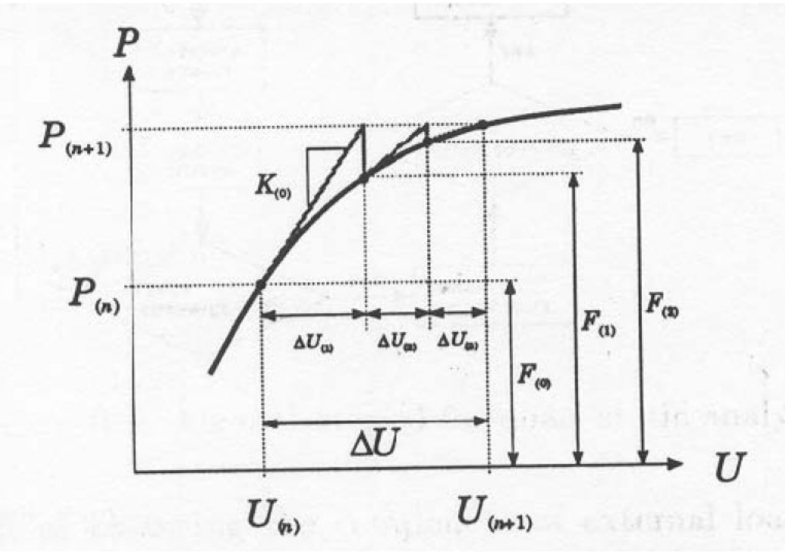

Figure 2. 17. Response curve of spring to applied loads (Rocscience Inc. 2018a).

The initial guess is set at $U_{(n)}$ when $P_{(n)}$ is applied to the spring. The goal of FEM analysis can be understood as finding the relative displacement ΔU with respect to a new load $P_{(n+1)}$ which can be seen in Figure 2.17. The first iteration of the analysis begins with calculating the tangent stiffness $K_{(0)}$ of the response curve at the initial point. This is a linear approximation of the response curve. Thus, the linear line of $K_{(0)}$ intersects $P_{(n+1)}$ and the first displacement $\Delta U_{(1)}$ is obtained. $F_{(1)}$, the internal force of the spring can be calculated at this point $U_{(n+1)}$= $U_{(n)}$+$\Delta U_{(1)}$. The imbalance of the force or in other words, the calculation error is $P_{(n+1)} - F_{(1)}$. As can be clearly seen in Figure 2.17, the imbalance is large. So, the second iteration begins at the updated point $U_{(n+1)}$. Using the linear approximation of the response curve. The displacement and internal force of this iteration are $\Delta U_{(2)}$ and $F_{(2)}$, respectively. The point then is updated as $U_{(n+1)} = U_{(n+1)} + \Delta U_{(2)}$. The imbalance becomes $P_{(n+1)} - F_{(2)}$, which is evidently smaller than the first iteration. With more iterations, this imbalance and displacement continuously reduce. To avoid infinite iterations, certain criteria need to be introduced.

In RS2 analysis, two conditions are checked at the same time, which are absolute force and energy.

$$\left|\frac{P_{(n+1)}-F_{(i)}}{P_{(n+1)}}\right| < user\ defined\ tolerance \tag{2.31}$$

$$\left|\frac{\Delta U_{(i)}\cdot(P_{(n+1)}-F_{(i)})}{\Delta U_{(1)}\cdot(P_{(n+1)}-F_{(1)})}\right| < user\ defined\ tolerance \tag{2.32}$$

where $i = 1, 2, 3$ is the iteration number. The physical meaning of the absolute force is the imbalance with respect to the new load has been reduced to a certain level. Whereas, the absolute energy criterion further takes the displacement into consideration. If the final iteration has been reduced to a certain level with respect to the first iteration results, then $F_{(i)}$ can be considered sufficiently close to $P_{(n+1)}$.

2.4.6 Determination of Factor of Safety (FS)

The FS is the most important factor to analyze slope stability. The definition of FS for a slope is the shear strength of the soil divided by the shear stress (Duncan et al. 2014). Theoretically, when the FS > 1.0, the slope is absolutely stable. However, for design and construction of earth or rockfill dams, required factors of safety are achieved based on experience due to inaccurate values of variables during calculating FS. Table 2.13 summarizes appropriate factors of safety for various types of slopes and analysis conditions.

Table 2. 13 Minimum required factors of safety for different loading in the design of earth and rockfill dams (Hoek 2007).

Loading condition	S.F.	Remarks
End of construction porewater pressures in the dam and undissipated porewater pressures in the foundation. No reservoir loading.	1.3	
Reservoir at full supply level with steady state seepage in the dam and undissipated end-of-construction porewater pressures in the foundation.	1.3	Possibly the most critical (even if rare) condition.
Reservoir at full supply level with steady state seepage.	1.5	Critical to design.
Reservoir at probable maximum flood level with steady state seepage conditions.	1.2	
Rapid reservoir drawdown from full supply level to minimum supply level	1.3	Not significant in design. Failures very rare and, if they occur, usually shallow.

In this study, the minimum FS is adopted as 1.3 to ensure the adequate performance of slopes because the rapid drawdown condition is considered.

2.5 Constitutive Models for Soils

As mentioned in coupled transient seepage analysis discussion (Section 2.1), an appropriate constitutive model defines the physical correctness of the material behavior. This section gives the background information on elastic and elastic-plastic soil models, as well as the elastic and plastic behaviors of the Mohr-Coulomb model.

2.5.1 Elastic Soil Model

Hooke’s law represents the physical meaning of stresses and strains for a linear, isotropic, elastic soil. For a general state of stress (Figure 2.18), Hooke’s law is (Punmia et al. 2005)

$$\begin{Bmatrix} \varepsilon_x \\ \varepsilon_y \\ \varepsilon_z \\ \gamma_{1_{xy}} \\ \gamma_{1_{yz}} \\ \gamma_{1_{zx}} \end{Bmatrix} = \frac{1}{E} \begin{bmatrix} 1 & -v & -v & 0 & 0 & 0 \\ -v & 1 & -v & 0 & 0 & 0 \\ -v & -v & 1 & 0 & 0 & 0 \\ 0 & 0 & 0 & 2(1+v) & 0 & 0 \\ 0 & 0 & 0 & 0 & 2(1+v) & 0 \\ 0 & 0 & 0 & 0 & 0 & 2(1+v) \end{bmatrix} \begin{Bmatrix} \sigma_x \\ \sigma_y \\ \sigma_z \\ \tau_{xy} \\ \tau_{yz} \\ \tau_{zx} \end{Bmatrix} \tag{2.33}$$

where ε, σ are the strains, normal stresses in the X, Y, and Z directions, respectively, γ_1, τ are the shear strains, shear stresses in XY, YZ, and ZX planes, respectively, E is the elastic (or Young's) modulus, and v is Poisson's ratio.

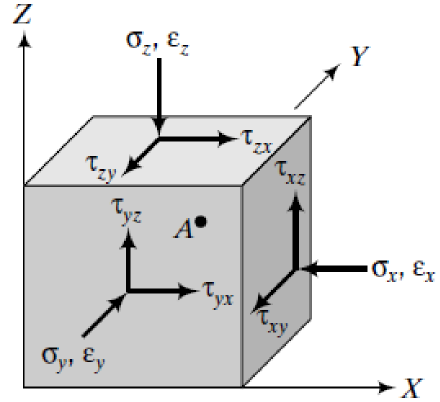

Figure 2. 18. General 3D state of stress (Punmia et al. 2005)

Equation 2.33 indicates that only two parameters govern the stress state, which makes the soil model inaccurate at high stress and strain levels. As a result, some nonlinear elastic models are proposed, such as Cauchy elastic model, Hyperelastic (Green) model, etc. (Chen and Mizuno 1990).

2.5.2 Elastic-Plastic Soil Model (Mohr-Coulomb Model)

Although both elastic and elastic-plastic models have been proposed as soil constitutive models, an elastic-plastic model is accepted to capture soil behavior in this research, which is closer to physical soil behavior. Various elastic-plastic models of soil material were proposed, including simple elastic-plastic models (e.g. Tresca and von Mises, Mohr-Coulomb, Drucker-Prager models, etc.) and advanced elastic-plastic models (e.g. Lade-Duncan model, Bounding surface models, MIT soil models, Bubble models, etc.) (Chen and Mizuno 1990). However, considering the lack of specific laboratory results required for using advanced elastic-plastic models, simple ones are adopted in this work.

The classical elastic-plastic model has four ingredients to be characterized (Bertram and Gluge 2013):

(a) an *elastic law*, which demonstrates the elastic behavior of the material before yielding. In this research, Hooke's law is used to model the elastic deformation.

(b) a *yield criterion*, which describes the elastic limit of the material, i.e. yield function, and surface. It is assumed that the soil's mechanical behavior is elastic before yielding, while the soil behavior is obtained by various plastic failure criteria after yielding (Figure 2.19). The following equations explain the yield relationship (Punmia et al. 2005):

$$f(\sigma_{ij}) = 0 \quad Yield \tag{2.34}$$

$$f(\sigma_{ij}) < 0 \quad Elastic\ State \tag{2.35}$$

where σ_{ij} is the state of stress.

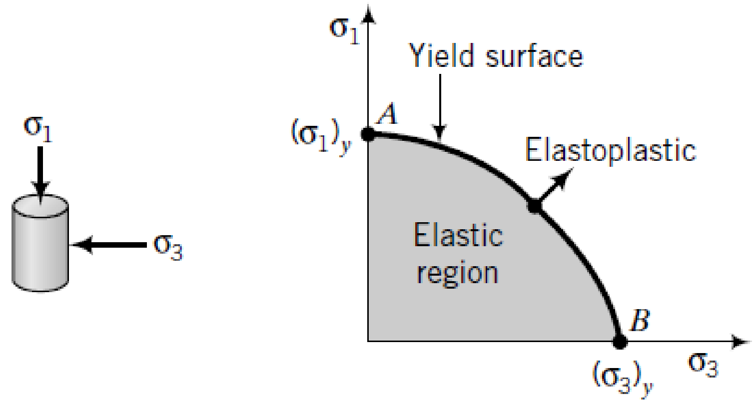

Figure 2. 19. Elastic, yield and elastoplastic stress states (Punmia et al. 2005)

Many different elastic-plastic constitutive models are available. This section focuses on the Mohr-Coulomb model which assumes soil as an elastic-perfectly plastic material. Figure 2.20 shows the stresses response of an elastic-perfectly plastic model when strained. Once the stress reaches the ultimate stress σ_U, the material is yielding. After the yielding point, the stress remains σ_U, as the strain increases. In general, it represents that the state of stress always satisfies $f\left(\sigma_{ij}\right) = 0$ during the plastic flow (Pietruszczak 2010).

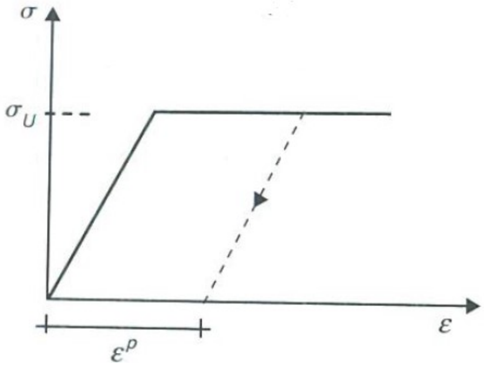

Figure 2. 20. Elastic-perfectly plastic stress-strain behavior (Pietruszczak 2010).

The critical shear stress is a function of normal stress. In 1773, Coulomb proposed a linear relationship between shear strength on a plane and the normal stress on it (Pietruszczak 2010):

$$\tau = c - \sigma tan\emptyset \qquad (2.36)$$

where τ is the shear strength, σ is the normal stress (tension positive), c is the cohesion and $\emptyset$ is the angle of internal friction. Mohr circle is tangential to the Coulomb's envelope to formulate a general mathematical criterion. At the failure state, shown in Figure 2.21, the stress state can be expressed as:

$$\tau = \frac{1}{2}(\sigma_1 - \sigma_3)cos\emptyset; \quad \sigma = \frac{1}{2}(\sigma_1 + \sigma_3) + \frac{1}{2}(\sigma_1 - \sigma_3)sin\emptyset \qquad (2.37)$$

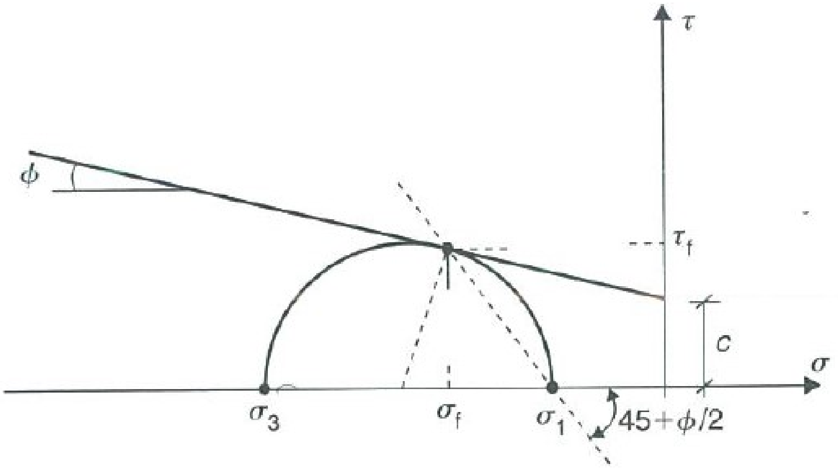

Figure 2. 21. Mohr circle defining the conditions at failure (Pietruszczak 2010)

For elastic-perfectly plastic materials, yield occurs while the material is failing. Thus, combining Equation 2.36 with Equation 2.37, the well-established Mohr-Coulomb yield (failure) surface for $\sigma_1 > \sigma_2 > \sigma_3$ is (Pietruszczak 2010):

$$F = \frac{1}{2}(\sigma_1 - \sigma_3) + \frac{1}{2}(\sigma_1 + \sigma_3)sin\emptyset - ccos\emptyset = 0 \tag{2.38}$$

The corresponding yield surface of Mohr-Coulomb criterion in principal stress space is displayed in Figure 2.22.

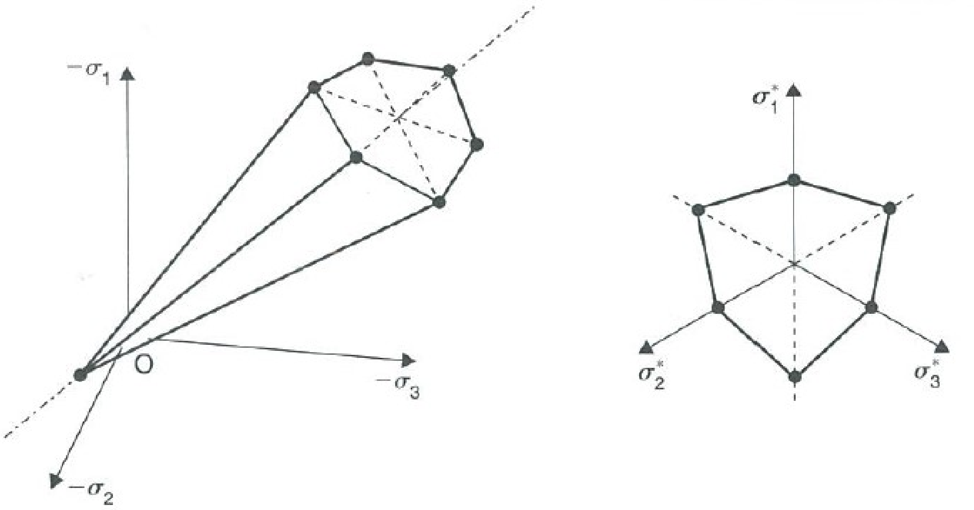

Figure 2. 22. Mohr-Coulomb criterion in the principal stress space (Pietruszczak 2010)

(c) a *flow rule*, which depicts the development of plastic deformation during yielding. Since the plastic potential function coincides the yield function of a Mohr-Coulomb model, the plastic potential function has the same form as the yield surface (Equation 2.38).

(d) a *hardening rule*, which governs the evolution of hardening or softening during yielding. After the initial yielding, the yield surface will expand (hardening) according to the applied hardening rules (e.g. isotropic hardening, kinematic hardening, and mixed hardening) until failure occurs. The stress-strain behavior of the Mohr-Coulomb model reflects perfectly plastic response after yielding so that no hardening or softening law is required.

Chapter 3 Development of the Slope Stability Numerical Model

3.0 Introduction

This section presents the generation of numerical models based on the literature review, and the verification of RS2 for further simulation work through the comparison of analysis results with literature-reported cases. Since there is no material model for rails or ties in RS2 and the objective of the research is not to study their behavior, train loads on the tie-ballast interaction surface of all models were calculated manually and then applied to the model. Thus, the behavior of rails and ties is not considered in this study. Section 3.1 addresses the model creation of each part such as external train loads, superstructure of the track, substructure of the track, natural slope and water conditions. Section 3.2 describes the verification of a simple case similar to the model in this thesis, which shows RS2 can successfully handle slope stability analysis under these conditions.

3.1 Process of Building the Simulation Model

In this section, one typical model will be taken as an example to demonstrate how it was built step-by-step. Creating a simulation model begins with parameter selection of track superstructure and calculation results of external train loads on the tie-ballast contact surface. Next step is to determine all the dimensions of track substructure. The geometry of the whole model is completed once the dimension of the natural slope, applied loads, and the water condition are established. Assigning material properties, setting boundary conditions and generating mesh elements are also required.

3.1.1 Geometry of Track and Load Condition

The step of track design is prior to achieving the corresponding external train loads. Considering a practical case of heavy haul freight trains (AREMA 2010), the load per axle is set to be 36,000 lbs (160kN) with a typical freight car wheel diameter of 0.914 m (36 inches). The dimensions of the track, such as rail gauge, tie width, length, height, and spacing, are then determined, as shown in Table 3.1 (Selig and Waters 1994). As can be seen in Figure 3.1, two trucks with two axles per truck support a freight car. And generally, these two adjacent axles of a truck are connected with each other. As seen in Figure 3.1, the distance between two trucks of a car, known as the truck center distance (TC) is much larger than that between axles of each truck, known as truck axle spacing (S_T). Moreover, the analysis in this work focuses on the front-view transverse section, other than the side-view longitudinal section denoted in Figure 3.1. Based on the preceding two points, two wheel loads per truck can be simplified as one which counts the resultant of loads on two adjacent axles as seen in Figure 3.1.

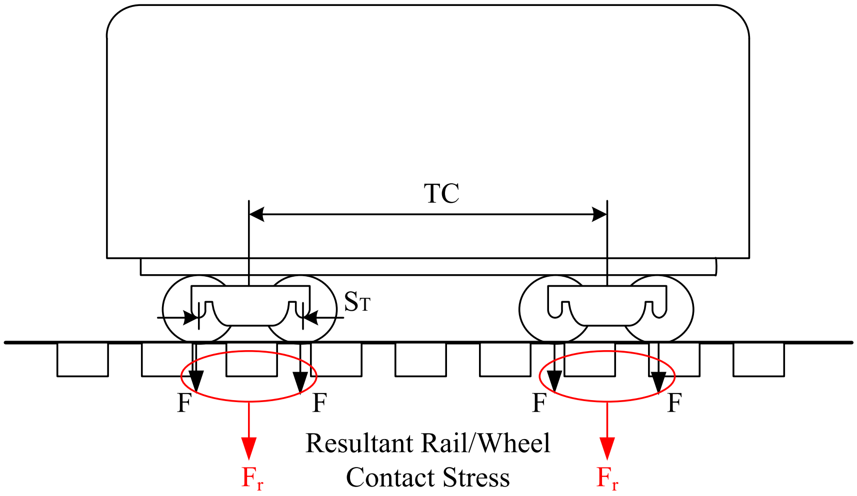

TC = length between the center pin on the trucks, known as the truck center distance, and
S_T = truck axle spacing, the distance between the adjacent axles of a truck.

Figure 3. 1. Diagram of resultant rail/wheel contact stress of a 4-axle railcar.

Table 3. 1 Parameters of the freight train and track superstructure

Parameter	Unit	Value
Number of axles per car	\	4
Per axle load (loaded)	lbs	36,000
	kN	160
Wheel diameter	inch	36
	m	0.914
Rail gauge	m	1.435
Tie width	m	0.229
Tie length	m	2.590
Tie height	m	0.150
Tie spacing	m	0.495

To obtain the external force, the loading condition has to be studied carefully. In that context, it has to be noted that several assumptions were made in specifying the loading condition, as follows:

1. The model is simplified to two dimensions without considering curves of the track, the only straight (tangent) track will be modeled, satisfying plane strain assumptions.
2. The train is stopped on the straight track (zero velocity) or is running with a certain constant speed through the straight track.
3. The track, the rails, and the wheels are level, even and smooth, respectively.
4. Wind and temperature conditions are neglected in this study.

The method used to obtain the force to be applied has already been well addressed in Section 2.2.3. Thus, the main steps of the calculation are shown in Figure 3.2.

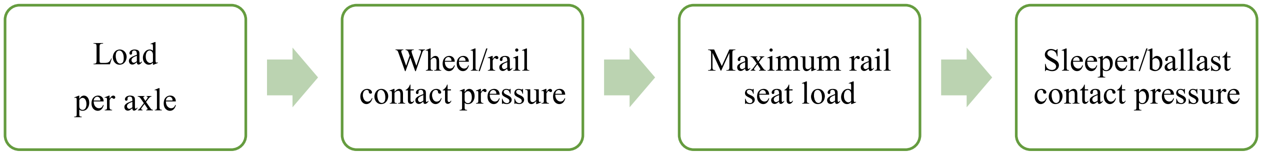

Figure 3. 2. Calculation flow of load transmission.

In the analysis, the moving heavy-haul freight train is assumed to travel straight along a river on the track. Based on the model parameters listed above in Table 3.1, the unknown parameters (e.g. wheel load, impact factor, distribution factor, and average ballast pressure at tie face) could be calculated through the aforementioned method from Section 2.2.3. As an example, assuming different train speeds, the corresponding impact factors, and average sleeper/ballast contact pressures are thus calculated and presented in Table 3.2. To be noted that the imperial units are adopted during the calculation, which would be transferred to the metric units in order to unify with those in the simulation software.

Table 3. 2 Impact factors for different train speeds

Train speed	mph	0	15	30	45	60	75
	km/h	0	24	48	72	96	120
Impact factor	\	0	0.1375	0.2750	0.4125	0.5500	0.6875
Impact factor in percent	%	0	13.75	27.50	41.25	55.00	68.75
Average ballast pressure at tie face	kPa	236.24	268.73	301.21	333.70	366.18	398.66

3.1.2 Geometry of the Entire Numerical Model

With the force transferred from a heavy-haul freight train to the bottom of a tie face, the next step is to define the embankment in a model. As shown in Figure 3.3, the embankment structure is composed of timber sleepers, ballast, subballast, and subgrade, which is built on a natural clay layer on the bank of a typical river. All dimensions are shown in the same figure (Figure 3.3). To provide adequate lateral resistance and confinement, the ballast shoulder width and roadbed shoulder width are set 0.35 m and 0.6 m, respectively. According to AREMA's Manual for Railway Engineering (AREMA 2010), the depths of each layer from top to bottom are set as 0.5 m, 0.2 m, and 0.3 m, which are typical values for such railways. The inclinations of the side slopes of ballast, subballast and subgrade are used 1V:2H (one vertical to two horizontal). The train loads are transferred to the average ballast pressure (uniform load) at the bottom of the tie.

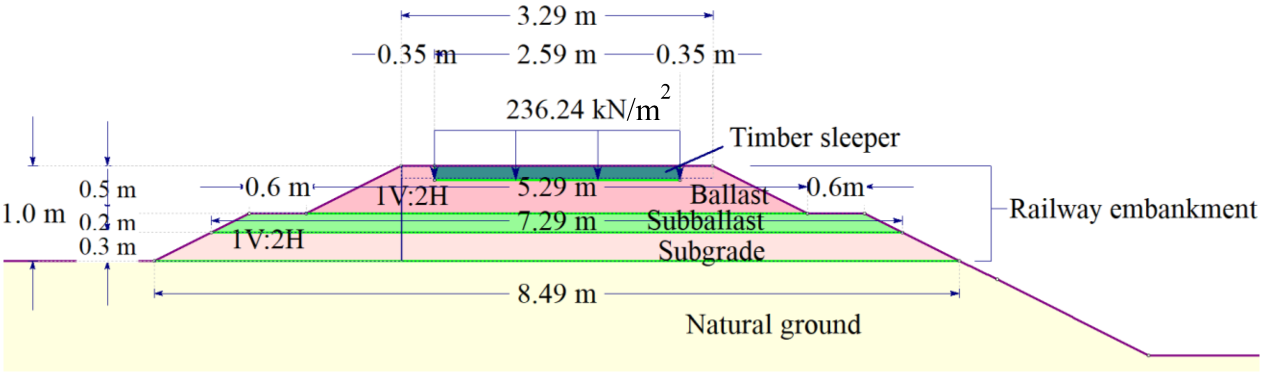

Figure 3. 3. Cross-section of the railway embankment structure with dimensions.

For the further parametric study, the height of subgrade is one of the variables, making the railway embankment height ranging from 1.0 m to 5.0 m. The inclinations of the side slopes of subballast, subgrade, and river bank are considered as one variable, named slope inclination, selected as 1V:2H or 1V:3H. Besides, the train speed is also one of the variables which induces different uniform loads at the tie-ballast interface.

Next step is to complete the geometry of natural ground under the railway embankment. The main considerations are to ensure that the stress is not reflected by the outer boundaries of the model, and the computing time. On the account of the variability of natural ground slope height, the dimensions of the natural ground foundation have the following relationships (Figure 3.4):

- the right-side height of the natural ground is set approximately 4 times the total height of both railway embankment and the nearby river, which can be expressed in Equation (3.1).

$$h \approx 4 \times (f + g) \tag{3.1}$$

- the lengths of the unsubmerged and submerged natural ground segments are at least the same length as that of the bottom of the embankment (Equation (3.2)) and greater than 1.5 times that of the bottom of the embankment (Equation (3.3)), respectively.

$$b \geq c \tag{3.2}$$

$$e \geq 1.5c \tag{3.3}$$

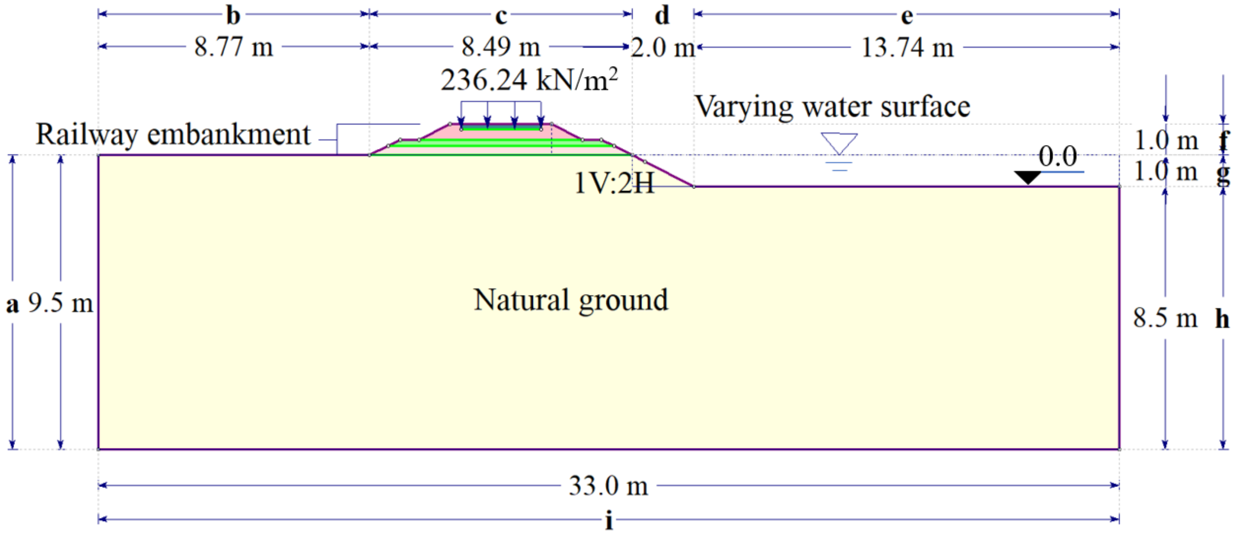

Figure 3. 4. Cross section of the numerical model with dimensions.

As illustrated in Figure 3.4, the height of railway embankment, measured from the top of the natural ground, is 1.0m. The water surface ranges from the river bed (at elevation zero) to the top of the natural ground, which means the railway embankment is unsubmerged.

3.1.3 Material Properties

The upper substructure layer is ballast, made of angular and uniformly graded crushed stone. A broadly graded gravel and sand layer of subballast could prevent mixing of subgrade and ballast. The natural ground soil type is clay. The material properties of embankment layers and foundation soil used for this analysis are summarized in Table 3.3, where the values are taken from the ones presented in Chapter 2. All soil layers are modeled as elastic-plastic materials. The failure criterion is set as Mohr-Coulomb.

Table 3. 3 Material properties of the railway embankment and foundation soil

Name	Soil type	Unit weight	Porosity	Cohesion	Friction angle	Poisson's ratio	Young's modulus	Permeability
		kN/m^3	\	kPa	°	\	kPa	cm/s
Ballast	Crushed stone	26	0.5	0	45	0.2	127,490	1.0×10^{-1}
Subballast	Gravel and sand	24	0.5	0	35	0.3	196,130	1.0×10^{-3}
Subgrade	Sand	22	0.5	0	38	0.3	78,000	1.0×10^{-4}
Natural Ground	Clay	18	0.3	35	10	0.3	20,000	1.3×10^{-6}

3.1.4 Mesh Convergence Study

The element type is chosen to be 6-noded (quadratic interpolation order with mid-side nodes) triangles which are generally more precise than 3-noded linear interpolation order elements (constant strain). Although the mesh type is uniform (approximately same-size triangles), the boundary discretization and element densities at the embankment structure and potential sliding zone within the rectangular dashed box are manually increased, as can be seen in Figure 3.5.

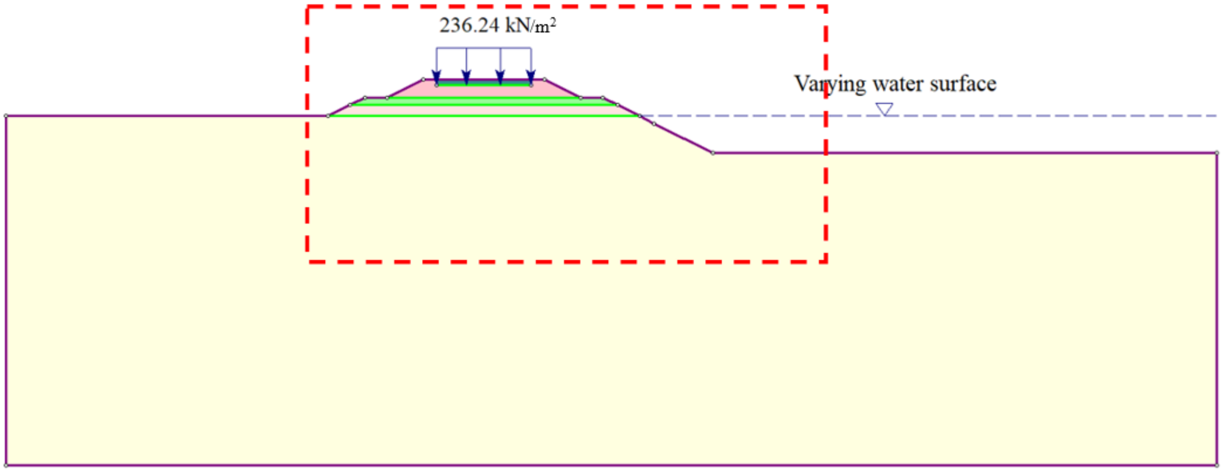

Figure 3. 5. Area of the numerical model with higher boundary discretization and element densities.

Generally, discretization (meshing) has a direct influence on the accuracy of finite element simulation results. Whether the mesh is satisfactory or not is to see if the simulation results remain the same by increasing the number of mesh elements in the same model, this process is called mesh convergence study.

In this study, the numerical model shown in Figure 3.5 is initially discretized by approximately 500 elements and up to around 16000 elements with the increasing number of elements step of $2^n \cdot N$ (N=500, and n = 0, 1, 2, …). To observe more evidently, the numerical model with 306 elements and 665 elements is also investigated. Table 3.4 summarizes the corresponding FS and computation time with a different number of mesh elements. Table 3.4 also shows the critical FS of the numerical model is 1.24 which is the criterion to calculate the differences in FS, as evaluated by Equation (3.4).

$$FS\ error = \frac{FS-1.24}{1.24} \tag{3.4}$$

Table 3. 4 The FS and computation time corresponding to a different number of mesh elements of the numerical model.

Number of elements	FS	FS Difference	Computation time (min)*	Normalized comp. time
306	1.51	21.77%	1.02	1.0
482	1.30	4.84%	1.22	1.2
665	1.27	2.42%	2.38	2.33
978	1.25	0.81%	2.70	2.65
2137	1.24	0.00%	5.40	5.29
4080	1.24	0.00%	9.00	8.82
8112	1.24	0.00%	19.90	19.50
16065	1.24	0.00%	40.37	39.58

* all computations were done on a Lenovo T450s with an i5 cpu @2.19 Ghz and 8 GB of memory

It can be seen that the mesh convergence occurs at 2137 mesh elements in Figure 3.6, where the FS difference curve reaches 0%. The relationship between mesh elements and the corresponding computation time for each simulation seems to be a linear relationship.

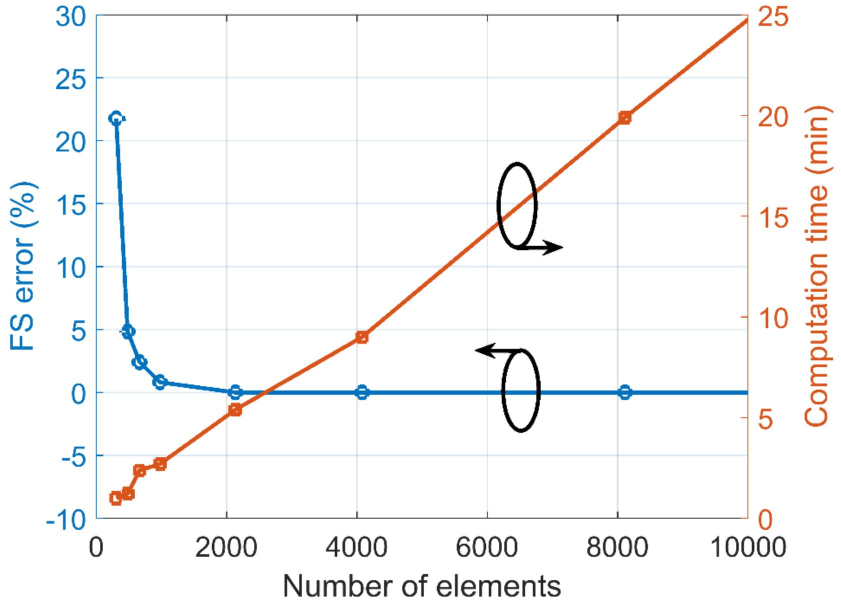

Figure 3. 6. Critical mesh elements for the numerical model and the corresponding computation time.

The phreatic line becomes smoother and continuous within the elliptical dashed region in Figure 3.7 (b) than that in Figure 3.7 (a), though the maximum shear strain contours are almost the same. Figure 3.7 reveals the mesh element number of 4080 could offer a more accurate simulation result than that of 2137. So, the adopted mesh element number is 4080 in this numerical model.

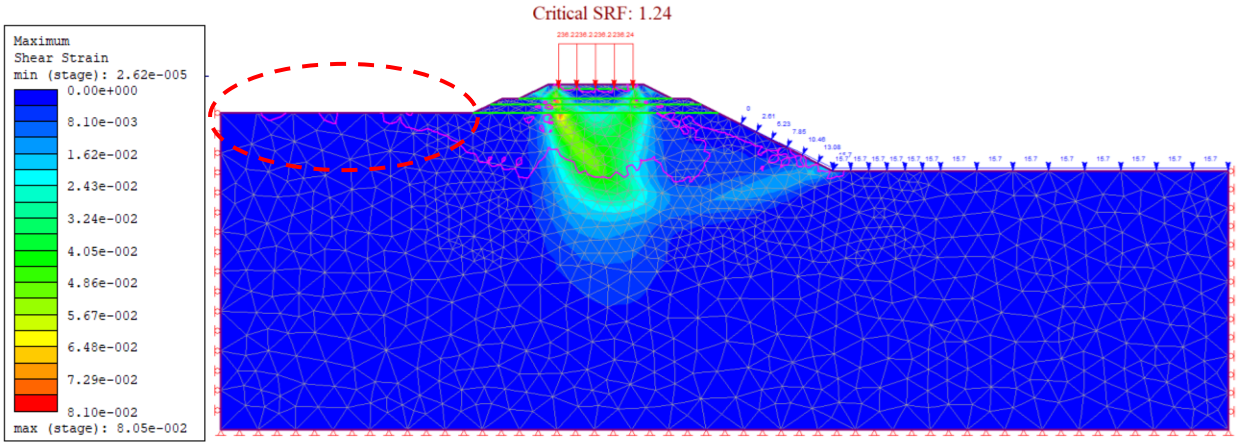

Figure 3. 7. (a) Maximum shear strain contour of the numerical model with 2137 mesh elements;

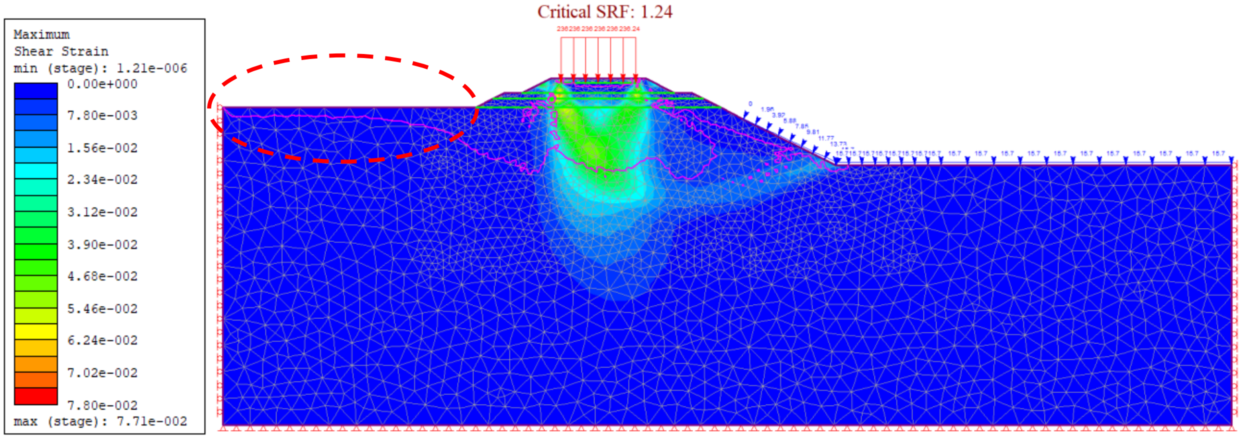

Figure 3. 7. (b) Maximum shear strain contour of the numerical model with 4080 mesh elements, (continued).

3.1.5 Boundary Conditions

Figure 3.8 shows a complete model, ready for analysis. The boundary is set at the bottom, left and right sides of the numerical model. At the bottom side of the model, the restraint exists in both X and Y directions (hinged or fixed), including the corners. Whereas the restraints along the vertical sides only exist in the X direction (rollers), allowing the effect of gravity in the Y direction. The boundary conditions remain the same during the entire simulation process.

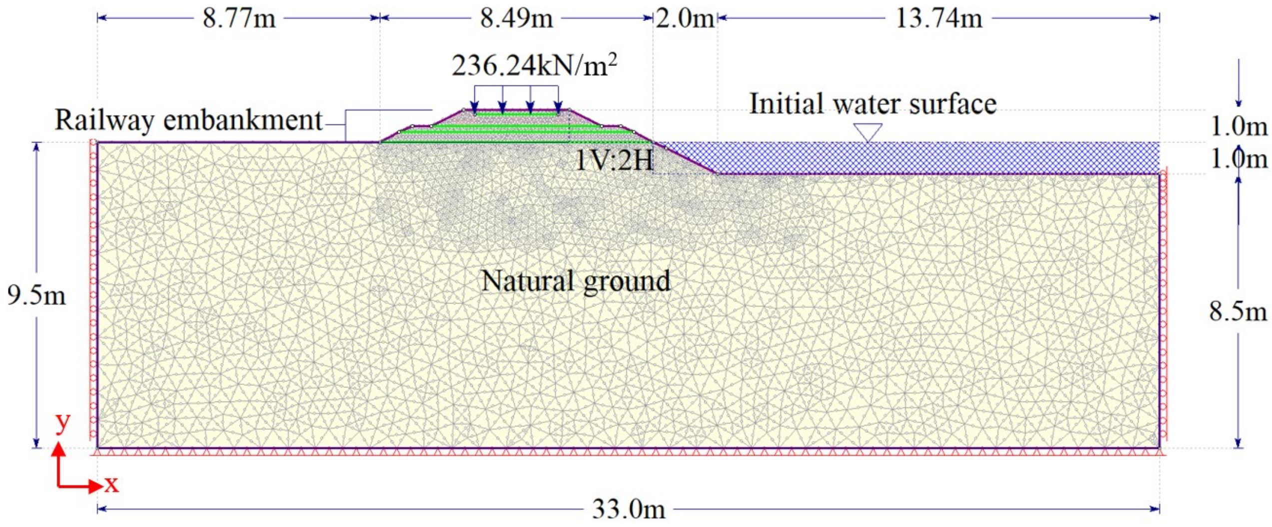

Figure 3. 8. Cross section of a complete model.

3.2 Verification

Before commencing the analysis of models, verifications are conducted with a comparison of results to that found in the literature. These are discussed in detail in this section. This significant step lays a solid foundation for subsequent analysis which will be presented in the following chapter. The selected reference studies slope stability analysis of an earth dam under rapid drawdown condition (Huang and Jia 2009). The main reason to select this reference is that it provides simulation results using SSRFEM which is the same method (also named FE-SSR method) applied for analyzing the numerical models in this thesis. Models under five different conditions were investigated and corresponding simulation results obtained by RS2 are attached for comparison.

3.2.1 Model Description

A homogeneous and isotropic earth dam on a foundation with a thickness of 7.3 m describes the major structure of the model, as presented in Figure 3.9. The dimensions of the model can also be found in the same figure. Table 3.5 lists material properties of the earth dam and foundation. It is assumed that the earth dam and foundation consist of the same type of soil.

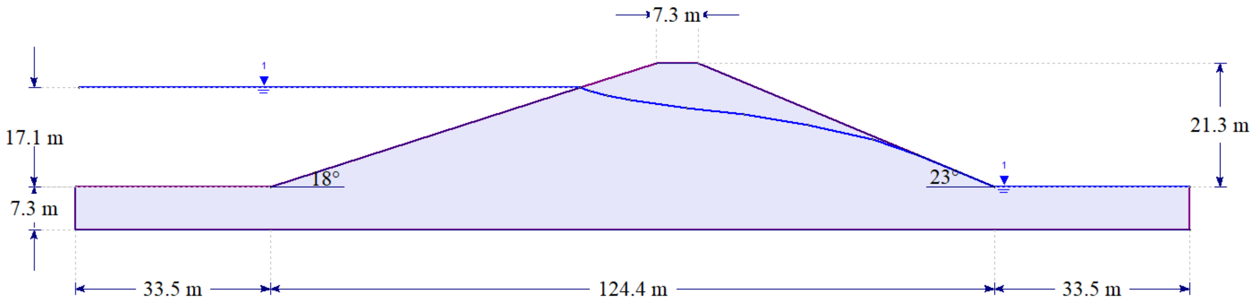

Figure 3. 9. Geometry of an earth dam with initial phreatic line (Huang and Jia 2009).

Table 3. 5 Material properties of earth dam and foundation

Name	Cohesion	Friction angle	Unit weight	Young's modulus	Poisson's ratio
	kPa	°	kN/m^3	kPa	\
Earth dam and foundation soil	13.8	37	18.2	1×10^5	0.3

3.2.2 Results and Discussion

With the same geometry, this structure has been investigated under five different conditions, i.e., dry dam (no phreatic surface), steady seepage before rapid drawdown takes place, 90 h, 300 h as well as 1500 h after rapid drawdown. The results reported by Huang and Jia (2009) and RS2, both using SSRFEM method, are shown as follows. The comparison mainly shows the critical SRF and failure mechanism as seen in Figures 3.10 – 3.14.

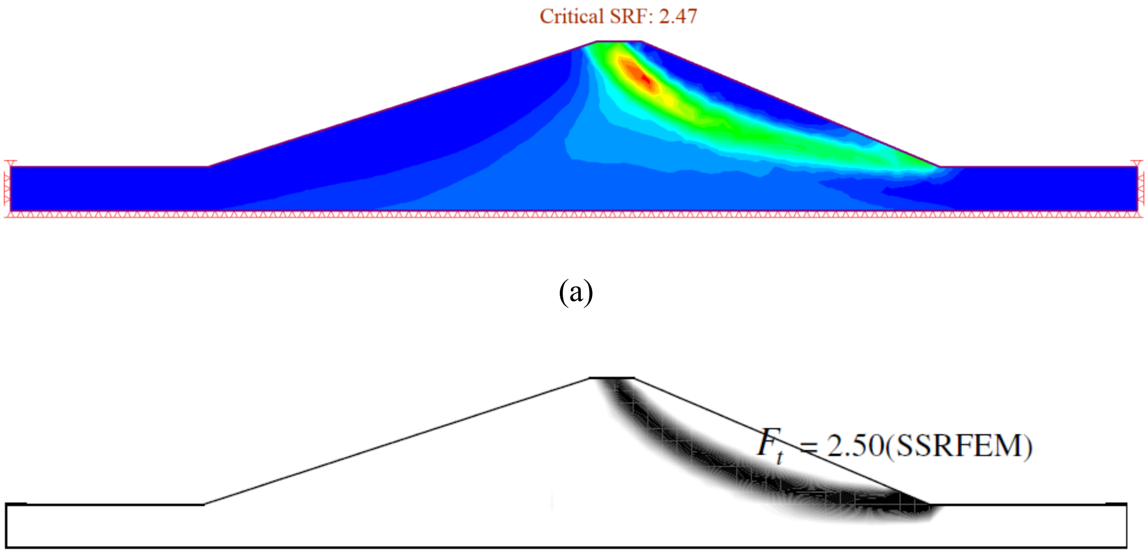

(a)

(b)

Figure 3. 10. Comparison of the critical SRF and failure mechanism for the case with no phreatic surface (dry dam): (a) results simulated by RS2 and (b) results captured in the work of Huang and Jia (2009).

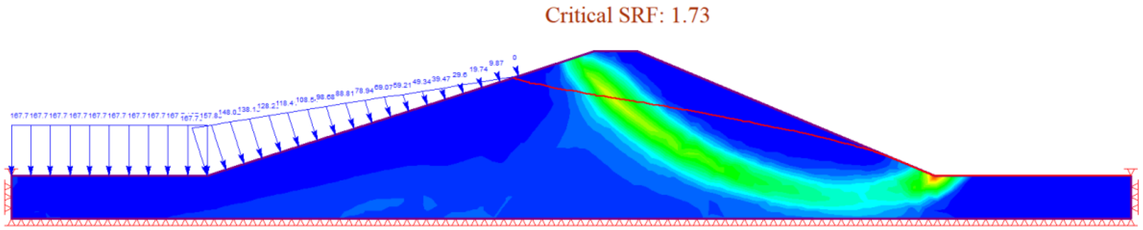

Figure 3. 11. (a) Comparison of the critical SRF and failure mechanism for the case with a steady phreatic surface (steady-state seepage): results simulated by RS2;

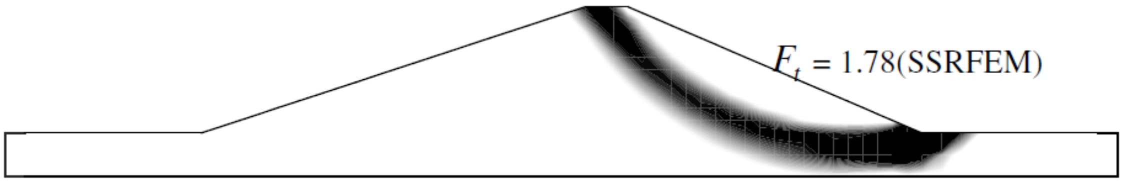

Figure 3. 11. (b) Comparison of the critical SRF and failure mechanism for the case with a steady phreatic surface (steady-state seepage): results captured in the work of Huang and Jia (2009), (continued).

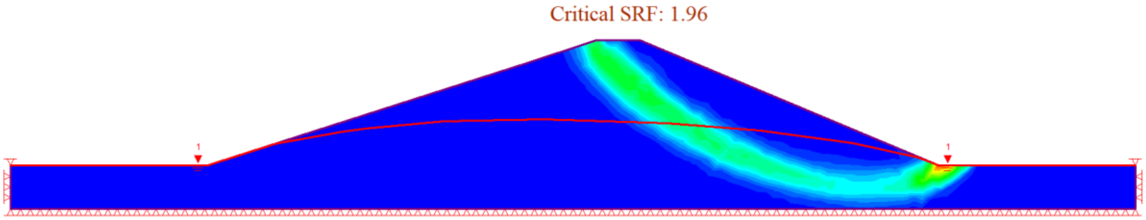

(a)

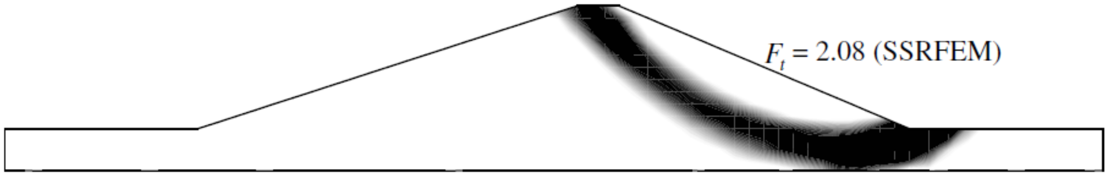

(b)

Figure 3. 12. Comparison of the critical SRF and failure mechanism at 90 h after rapid drawdown: (a) results simulated by RS2, and (b) results captured in the work of Huang and Jia (2009).

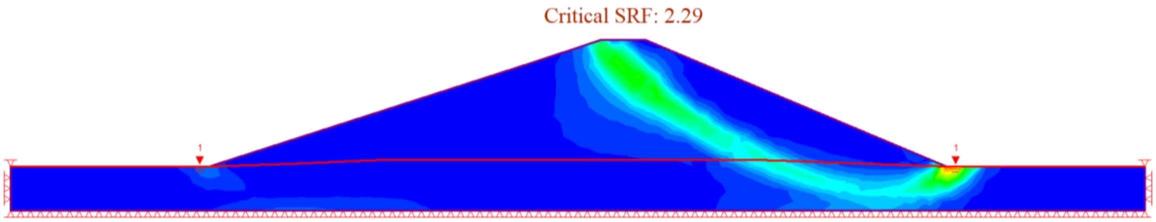

Figure 3. 13. (a) Comparison of the critical SRF and failure mechanism at 300 h after rapid drawdown: results simulated by RS2;

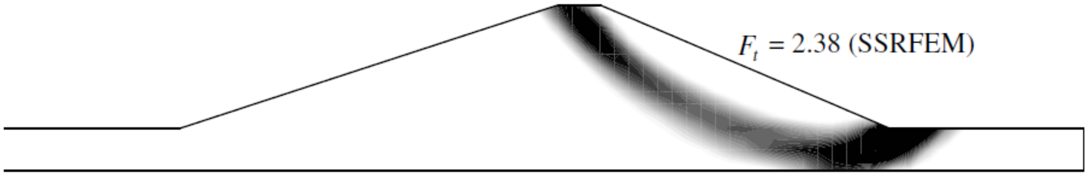

Figure 3. 13. (b) Comparison of the critical SRF and failure mechanism at 300 h after rapid drawdown: results captured in the work of Huang and Jia (2009), (continued).

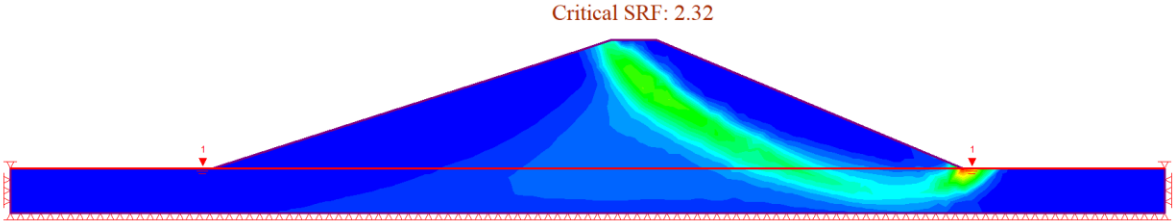

(a)

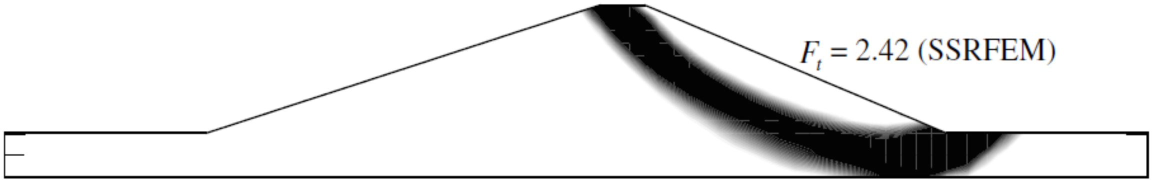

(b)

Figure 3. 14. Comparison of the critical SRF and failure mechanism at 1500 h after rapid drawdown: (a) results simulated by RS2, and (b) results captured in the work of Huang and Jia (2009).

As can be seen from Figures 3.10 – 3.14, for each different case, the critical SRF values computed by RS2 are relatively close to those reported by Huang and Jia (2009). Meanwhile, two sets of failure mechanisms under each condition agree with each other quite reasonably. Table 3.6 below summarizes the critical SRF values obtained from RS2 and reported by Huang and Jia (2009) both by SSRFEM as well as those obtained by LEM in the same reference. It can be observed that three sets of values under different conditions are quite close. Therefore, the simulation results by RS2 using SSRFEM are reliable, which means RS2 can be used for analyzing the target models.

Table 3. 6 Comparison of critical SRF values obtained by three different methods.

Stage	RS2 (FE-SSR method)	Reference	
		SSRFEM	LEM (Bishop's method)
Dry dam (with no free surface)	2.47	2.50	2.43
Initial condition (steady seepage)	1.73	1.78	1.70
At 90 h after rapid drawdown	1.96	2.08	1.92
At 300 h after rapid drawdown	2.29	2.38	2.28
At 1500 h after rapid drawdown	2.33	2.42	2.38

Chapter 4 Analysis of Rapid Drawdown and Discussion of Simulation Results

4.0 Introduction

Three different sets of simulation models were studied in this chapter with the aid of RS2 FEM software. The models represent three different scenarios, namely, a) no phreatic surface (dry slope) (Set I), b) only rapid drawdown (Set II), and c) both rapid drawdown and a moving freight train (Set III). The control variable method was applied to investigate model parameters. This chapter contains four sections which are organized as follows. Section 4.1 describes three sets of models, which are models with no phreatic surface, only rapid drawdown, both rapid drawdown and a moving freight train. A parametric study of models in Set I and II are presented in Section 4.2. Results of Set III are then discussed in Section 4.3 including discussions of the relationship between slope geometry and rapid drawdown information and maximum safe train speeds. Finally, conclusions are drawn in Section 4.4.

4.1 Three Sets of Models

To fully understand the stability of a slope influenced by rapid drawdown and moving freight train conditions, three sets of models are discussed in this section. Set I describes a dry slope with no train on the track. The rapid drawdown of water level is studied on top of Set I and forms models of Set II. Set III considers not only rapid drawdown but also the moving freight train conditions, as a further step based on Set II. Each set is interpreted from the following aspects: a) grouping for parametric study; b) description of simulation results of typical examples; c) discussion of results for the safety factors.

4.1.1 Set I: Dry Slope Model

Dry slope model refers to a slope with no free water surface and no train loads. Thus, three parameters were studied in this case: slope ratio, railway embankment height, and natural slope height, as shown in Figure 4.1. The simplified dendrogram in Figure 4.1 summarizes all the combinations of key values (from top to bottom) for the parametric study of the dry slope. Each combination denotes one case (one distinct model), and totally 30 models are studied in this section.

To better organize the results, Table 4.1 lists all the analysis cases derived from the above three parameters, 2 groups in total, consisting of 6 subgroups with 30 cases.

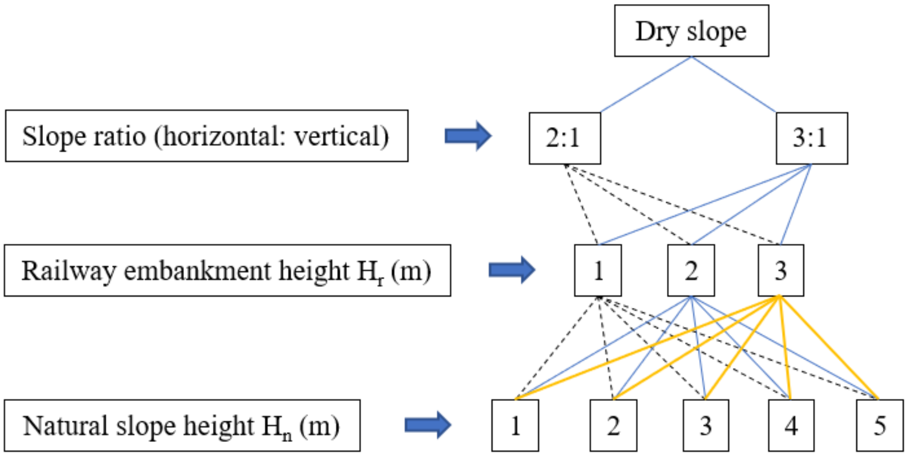

Figure 4. 1. Simplified dendrogram of various cases in Set I - dry slope model.

Table 4. 1 Cases in Set I - dry slope model

Groups	Subgroups	Slope ratio	H_r (m)	Number of H_n
Group 1	Subgroup 1	2:1	1	5
	Subgroup 2		2	5
	Subgroup 3		3	5
Group 2	Subgroup 4	3:1	1	5
	Subgroup 5		2	5
	Subgroup 6		3	5

The slope ratio has two conditions which are 3H:1V and 2H:1V (horizontal: vertical). The railway embankment height (H_r) is set to be 1, 2 or 3 meters. While the natural slope height H_n = 1, 2, 3, 4, and 5 meters, as shown in Figure 4.1. To be noted that all the other dimensions of the simulation model have been defined in Section 3.1 of Chapter 3 and remained the same during the analysis. As an example, Figures 4.2 (a) – (d) show a series of models of which only one parameter is different from each other. Figure 4.2 (a) shows the model with 2H:1V slope ratio, 1-meter railway embankment height, and 1-meter natural slope height. Models in Figures 4.2 (b) - (d) only have one parameter different from Figure 4.2 (a). Figure 4.2 (b) presents the model with a different slope ratio (3H:1V). The railway embankment height in Figure 4.2 (c) is set as 3 meters. In Figure 4.2 (d), the difference is the natural slope height (5 meters).

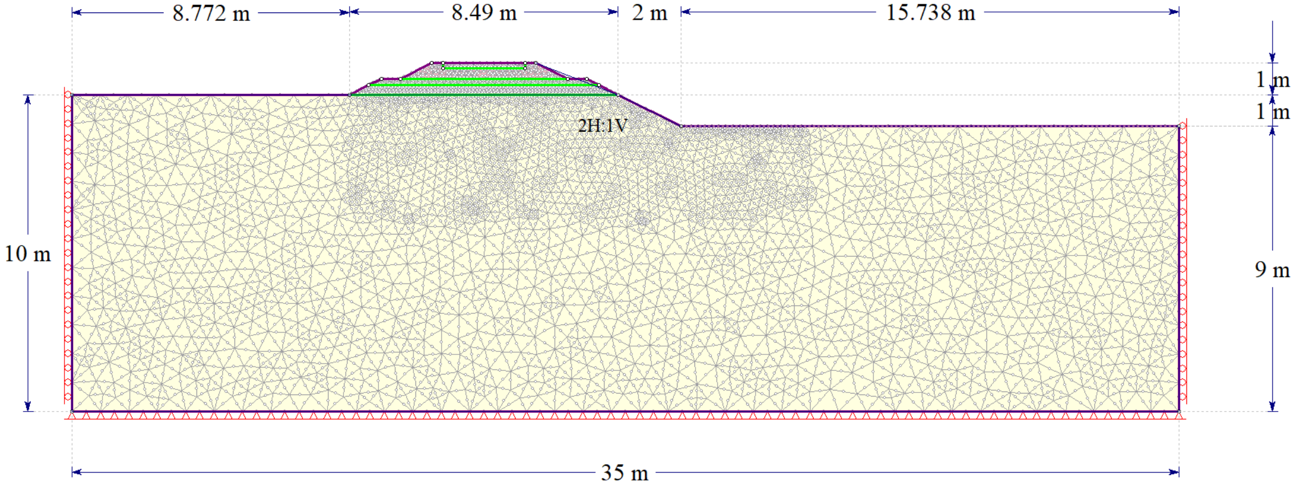

Figure 4. 2. (a) Model geometry: slope ratio = 2H:1V, H_r = 1 m, H_n = 1 m;

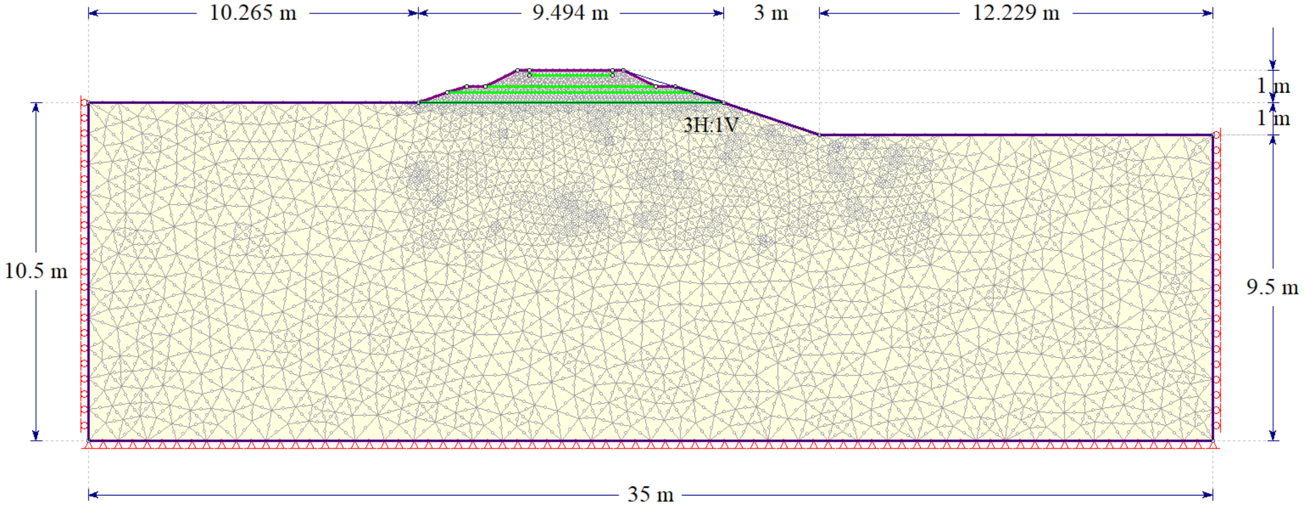

Figure 4. 2. (b) Model geometry: slope ratio = 3H:1V, H_r = 1 m, H_n = 1 m;

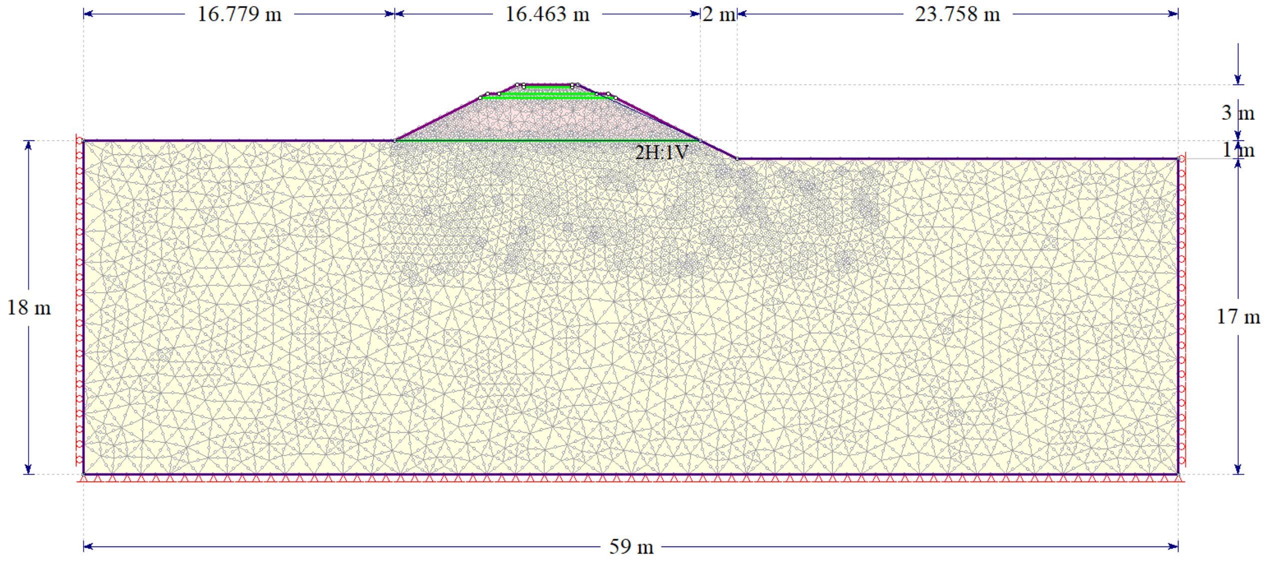

Figure 4. 2. (c) Model geometry: slope ratio = 2H:1V, H_r = 3 m, H_n = 1 m, (continued).

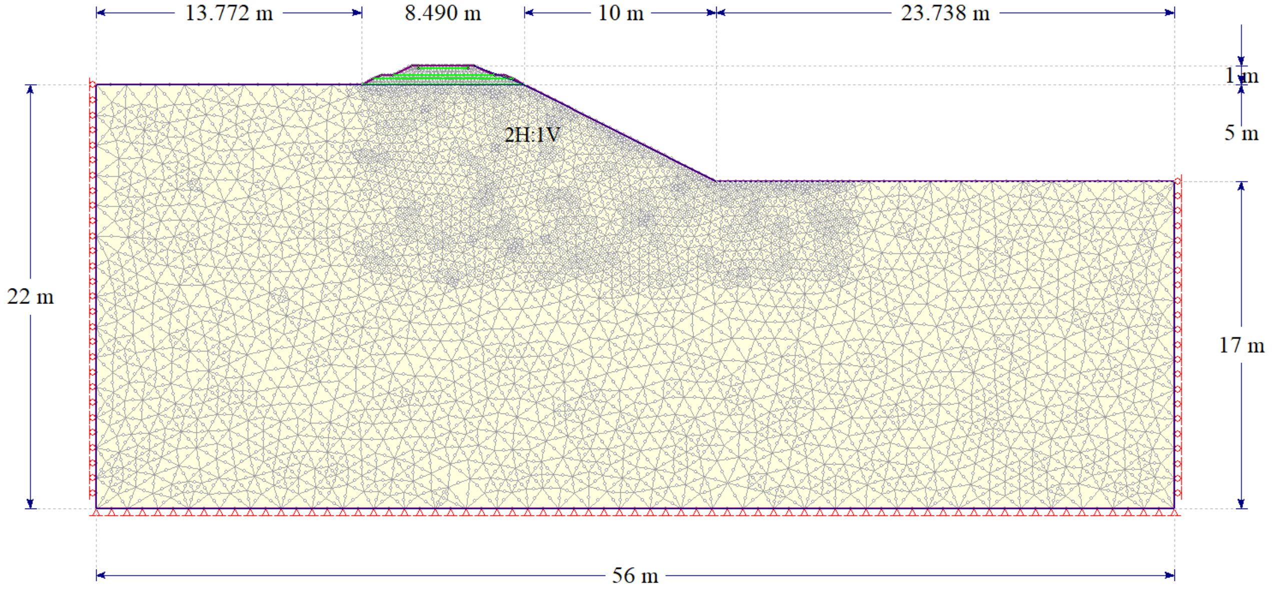

Figure 4. 2. (d) Model geometry: slope ratio = 2H:1V, H_r = 1 m, H_n = 5 m, (continued).

Corresponding simulation results of models in Figure 4.2 are displayed in Figure 4.3. The maximum shear strain contours and critical SRF values are shown. The model in Figure 4.3 (b) (slope ratio = 3H:1V, H_r = 1 m, H_n = 1 m) has the highest critical SRF value of 7.74. By contrast, the slope analysis in Figure 4.3 (d) (slope ratio = 2H:1V, H_r = 1 m, H_n = 5 m) has the lowest critical SRF value of 2.66. The comparison clearly indicates that a relatively flat slope is helpful for stability enhancement.

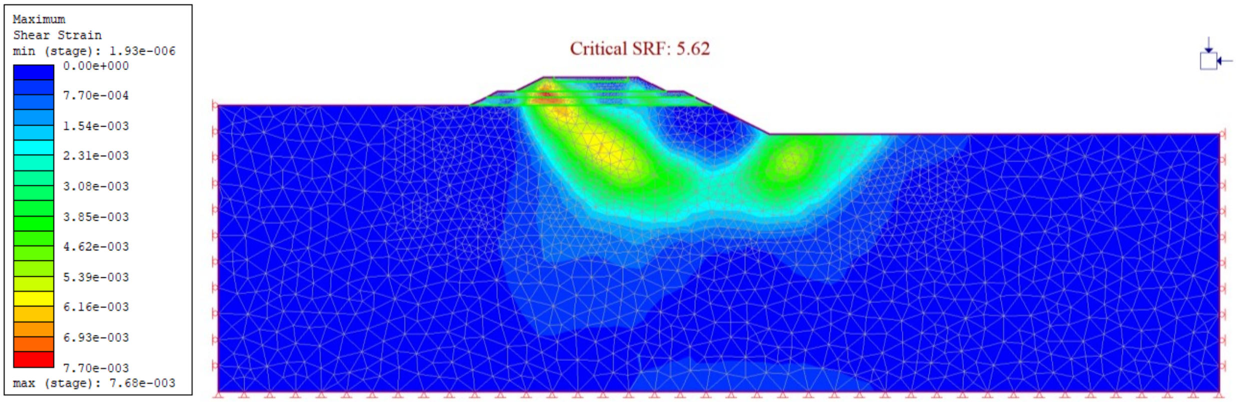

Figure 4. 3. (a) Maximum shear strain contours and critical SRF values for the models: slope ratio = 2H:1V, H_r = 1 m, H_n = 1 m;

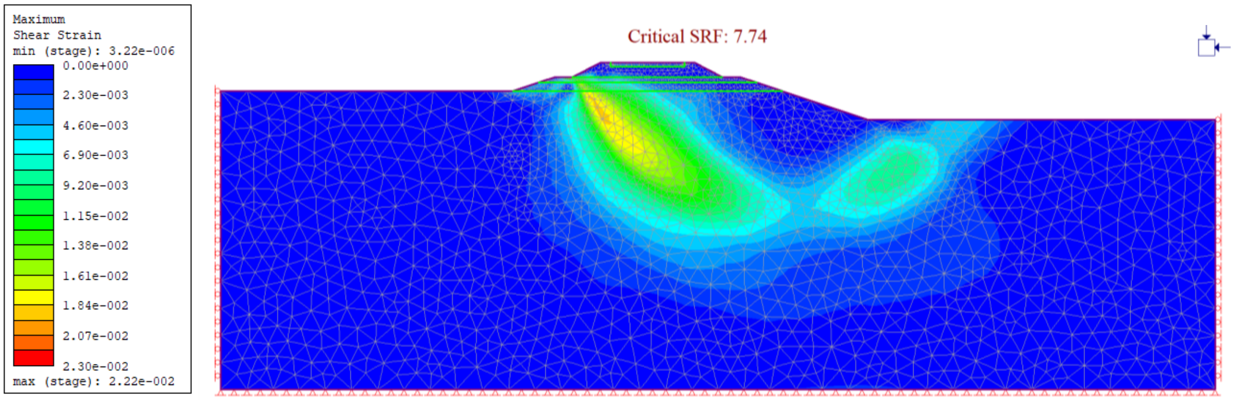

Figure 4. 3. (b) Maximum shear strain contours and critical SRF values for the models: slope ratio = 3H:1V, H_r = 1 m, H_n = 1 m;

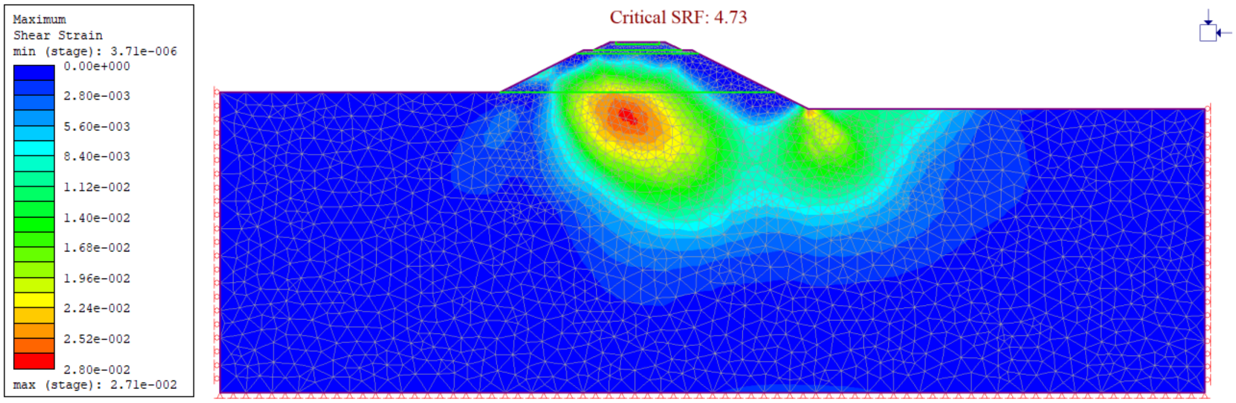

Figure 4. 3. (c) Maximum shear strain contours and critical SRF values for the models: slope ratio = 2H:1V, H_r = 3 m, H_n = 1 m;

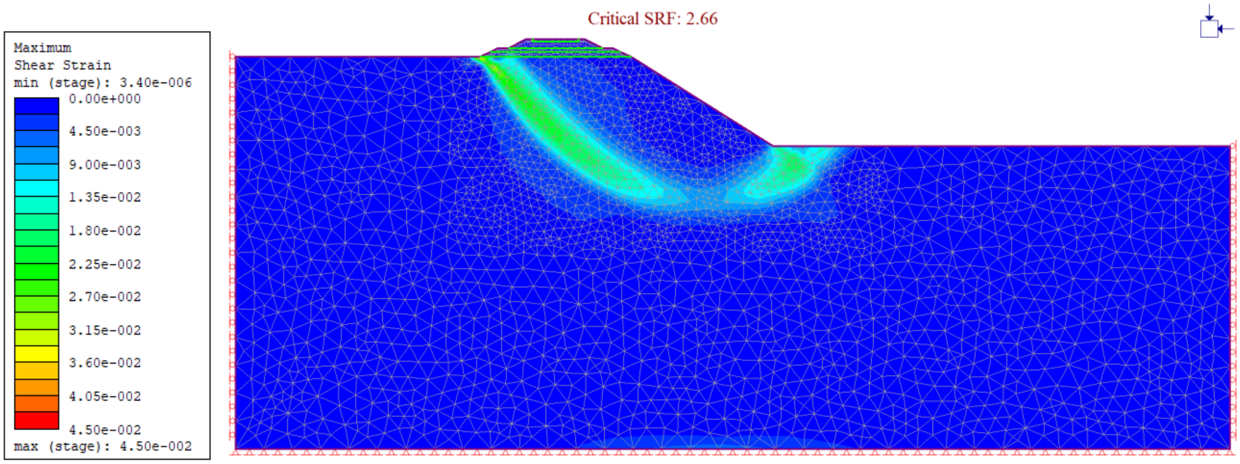

Figure 4. 3. (d) Maximum shear strain contours and critical SRF values for the models: slope ratio = 2H:1V, H_r = 1 m, H_n = 5 m, (continued).

During the simulation, starting from initial cohesion and friction, the slope was analyzed by the Shear Strength Reduction method. Subsequently, both the cohesion and friction were reduced by 1/FS in increments and the corresponding maximum total displacement was obtained from the simulation. The critical SRF value was reached once non-convergence occurs. Figure 4.4 shows the relationship between FS and the maximum total displacement for each model in Figure 4.2. To demonstrate the critical FS more clearly, the dense part has been enlarged which is shown in the left inset. Arrows mark all critical FS values for each case in the inset.

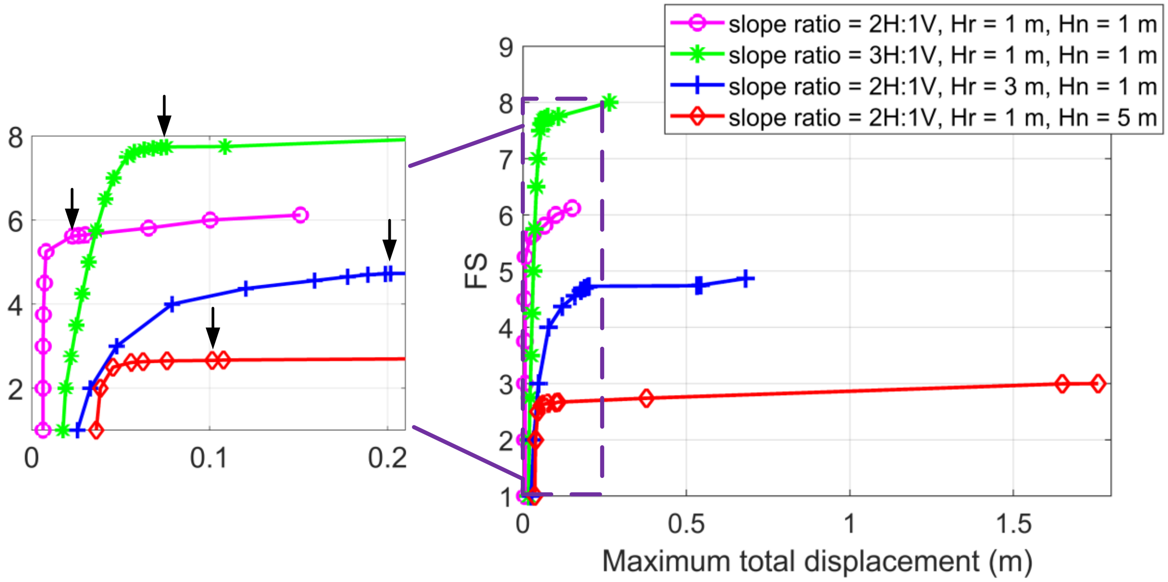

Figure 4. 4. Relationship between maximum total displacement and shear strength reduction factor (FS) for the selected models.

Table 4. 2 FS results of all cases in Set I

Groups	Subgroups	FS				
		Natural slope height (H_n) (m)				
		1	2	3	4	5
Group 1	Subgroup 1	5.62	5.36	4.13	3.46	2.66
	Subgroup 2	5.28	3.93	3.34	2.83	2.48
	Subgroup 3	4.73	2.88	2.98	2.54	2.37
Group 2	Subgroup 4	7.74	6.12	4.46	4.71	3.18
	Subgroup 5	5.47	4.25	3.29	4.03	2.65
	Subgroup 6	5.03	3.81	3.21	2.86	2.51

Results in Table 4.2 demonstrate that, in each group, FS generally decreases with a larger railway embankment height. Meanwhile, a higher natural slope tends to decrease the FS value. Based on Table 4.2, it also can be seen that the value of FS increases with a flatter slope.

4.1.2 Set II: Model Under Rapid Drawdown Conditions

In Set II, the drawdown ratio is included, besides the three factors (slope ratio, railway embankment height, and natural slope height) discussed in the previous dry slope model (Set I). The drawdown ratio is closely associated with the change in water level or drawdown depth (L) and the initial total head (H) as shown in Equation (4.1). For example, if H is 1 m, and L is 0.2 m, the corresponding drawdown ratio (L/H) equals 0.2. However, the drawdown rate (R) (the decline of water level per unit time) is not discussed since the undrained condition without drainage time is considered. It is generally understood that undrained cohesive soils have the lowest FS values among fully drained and partially drained conditions as shown in Figure 4.5.

$$Drawdown\ ratio = \frac{L}{H} \tag{4.1}$$

where L is the change in water level or drawdown depth (m), and H is the initial total head (m).

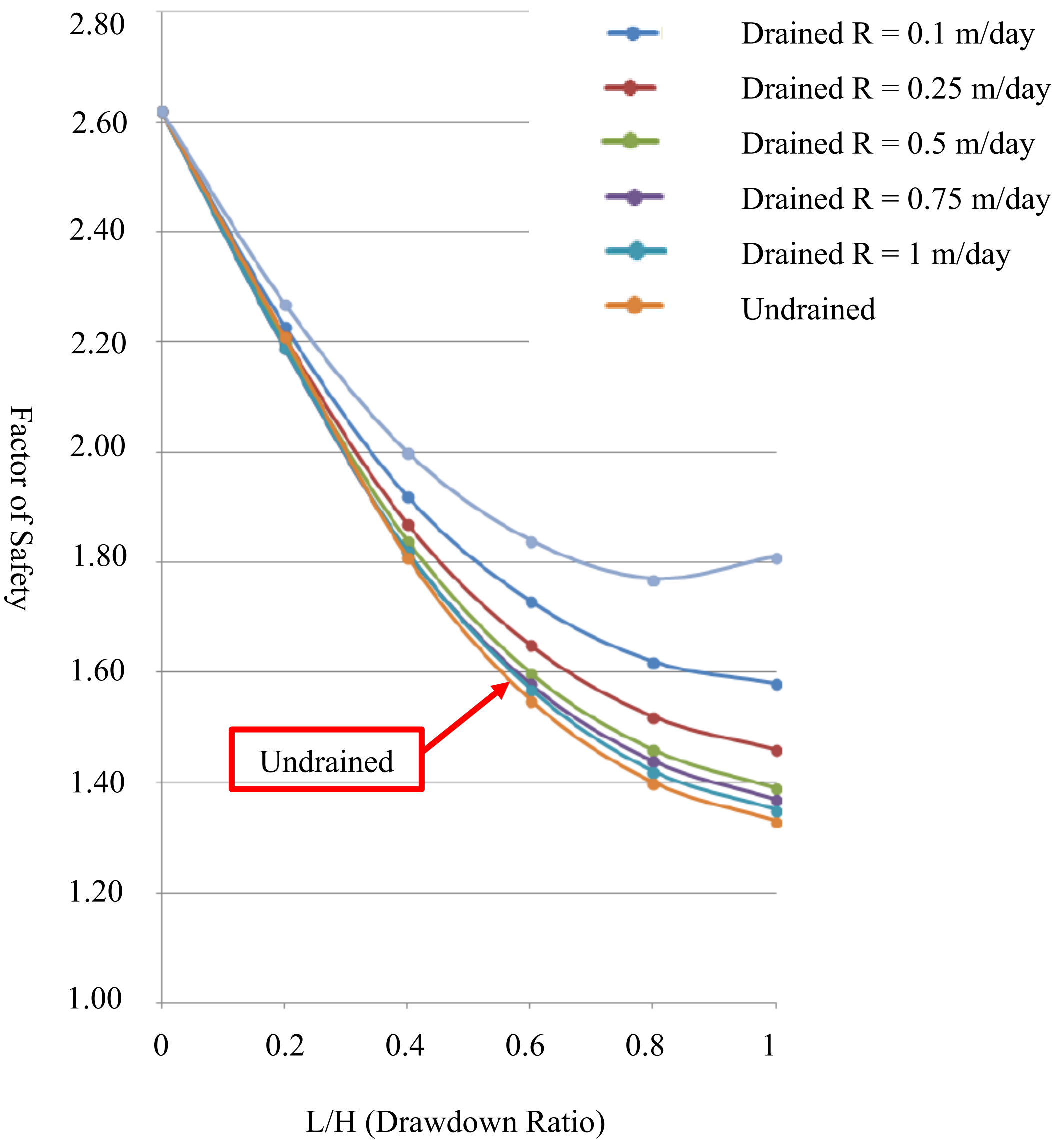

Figure 4. 5. FS versus drawdown ratio for three different drainage cases (Rocscience Inc. 2018b).

Five different drawdown ratios (L/H) (e.g. 0.2, 0.4, 0.6, 0.8, 1.0) were considered in the analysis. With assumed drawdown ratio, the corresponding drawdown depth can be calculated by Equation 4.1. In particular, L/H = 0 stands for a case that no rapid drawdown occurs, in other words, the initial water level condition remains constant. Similar to Figure 4.1, Figure 4.6 summarizes all combinations of four parameters studied in these models under rapid drawdown condition. Therefore, totally 150 different cases are investigated in Set II. Table 4.3 lists all these cases, with 6 groups in total, including 30 subgroups.

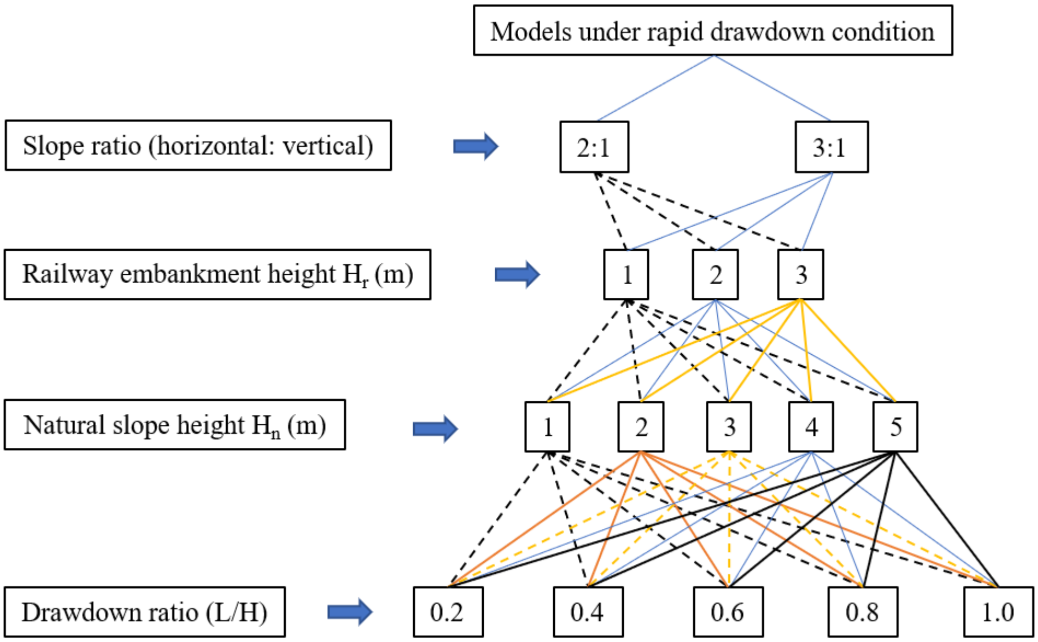

Figure 4. 6. Simplified dendrogram of various cases in Set II.

To have a straightforward comparison to the dry slope case (one example in Set I), the model with 2H:1V slope ratio, 1-meter railway embankment height, and 5-meter natural slope height, is taken as an example. The structure with these dimensions is shown in Figure 4.2 (d). The drawdown ratios of this model were considered as 0, 0.2, 0.4, 0.6, 0.8, 1.0, respectively. Similarly, the corresponding critical SRFs and maximum shear strain contours can be obtained through the simulation and results are presented in Figure 4.7.

Table 4. 3 Cases in Set II - model under the rapid drawdown conditions

Groups	Subgroups	Slope ratio	H_r (m)	L/H	Numbers of H_n
Group 3	Subgroup 7	2:1	1	0.2	5
	Subgroup 8			0.4	5
	Subgroup 9			0.6	5
	Subgroup 10			0.8	5
	Subgroup 11			1.0	5
Group 4	Subgroup 12		2	0.2	5
	Subgroup 13			0.4	5
	Subgroup 14			0.6	5
	Subgroup 15			0.8	5
	Subgroup 16			1.0	5
Group 5	Subgroup 17		3	0.2	5
	Subgroup 18			0.4	5
	Subgroup 19			0.6	5
	Subgroup 20			0.8	5
	Subgroup 21			1.0	5
Group 6	Subgroup 22	3:1	1	0.2	5
	Subgroup 23			0.4	5
	Subgroup 24			0.6	5
	Subgroup 25			0.8	5
	Subgroup 26			1.0	5
Group 7	Subgroup 27		2	0.2	5
	Subgroup 28			0.4	5
	Subgroup 29			0.6	5
	Subgroup 30			0.8	5
	Subgroup 31			1.0	5
Group 8	Subgroup 32		3	0.2	5
	Subgroup 33			0.4	5
	Subgroup 34			0.6	5
	Subgroup 35			0.8	5
	Subgroup 36			1.0	5

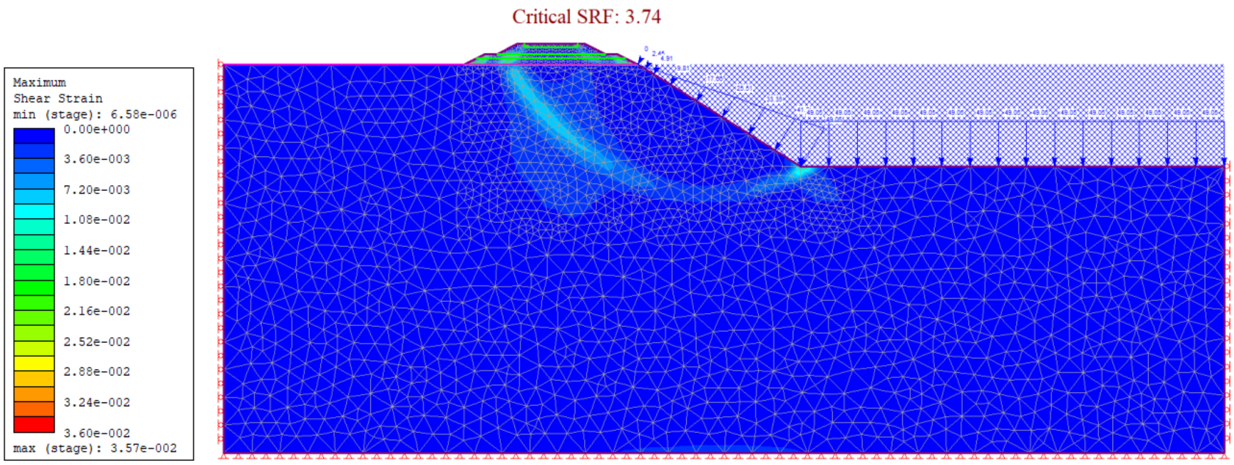

Figure 4. 7. (a) Maximum shear strain contour for the model with slope ratio = 2H:1V, $H_r = 1$ m, $H_n = 5$ m, and L/H = 0.

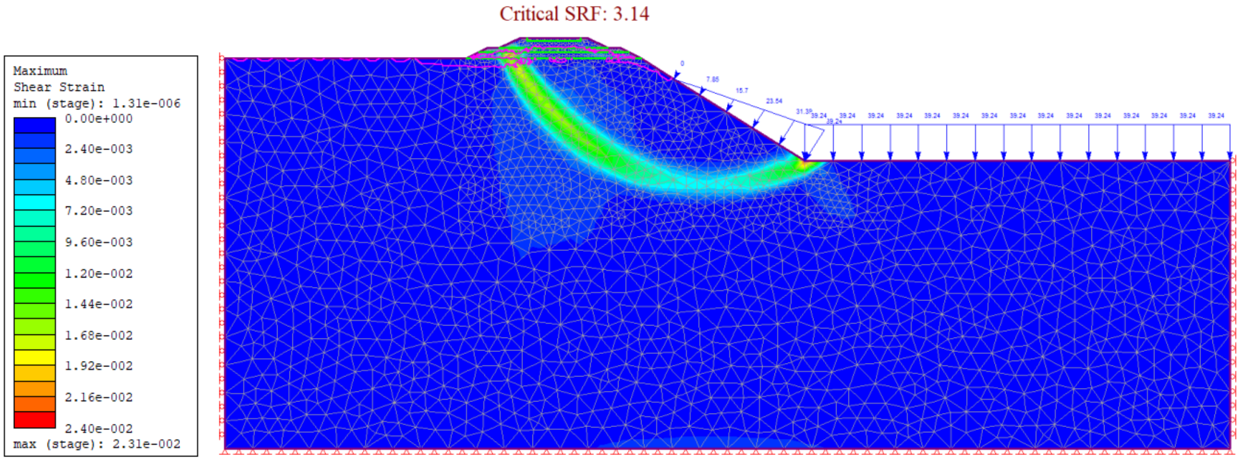

Figure 4. 7. (b) Maximum shear strain contour for the model with slope ratio = 2H:1V, $H_r = 1$ m, $H_n = 5$ m, and L/H = 0.2.

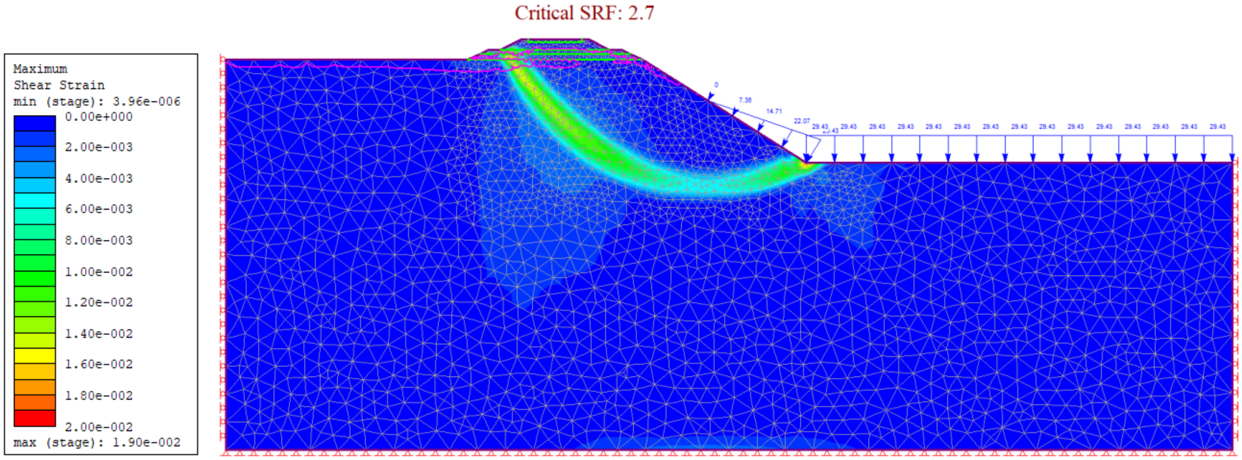

Figure 4. 7. (c) Maximum shear strain contour for the model with slope ratio = 2H:1V, H_r = 1 m, H_n = 5 m, and L/H = 0.4, (continued).

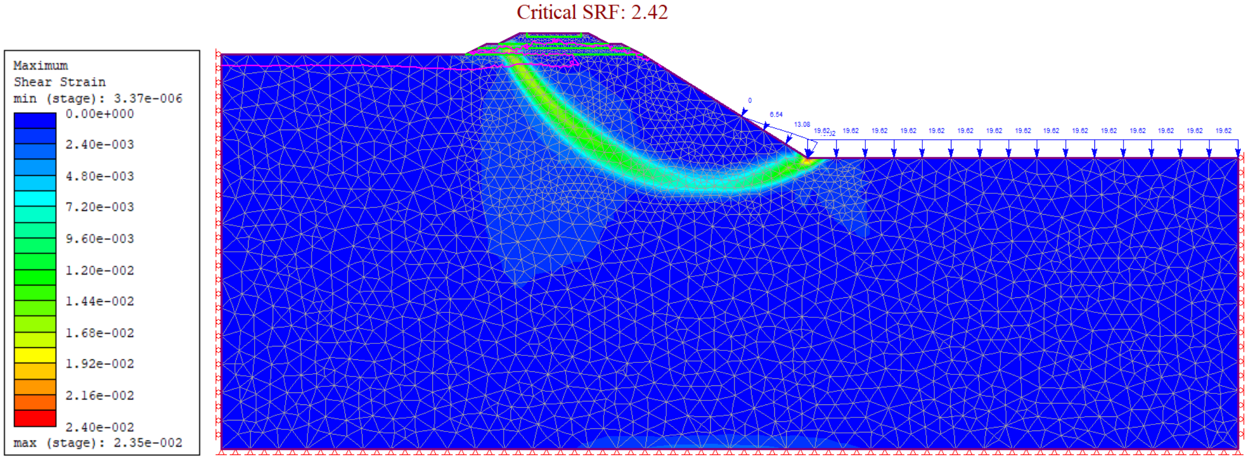

Figure 4. 7. (d) Maximum shear strain contour for the model with slope ratio = 2H:1V, H_r = 1 m, H_n = 5 m, and L/H = 0.6, (continued).

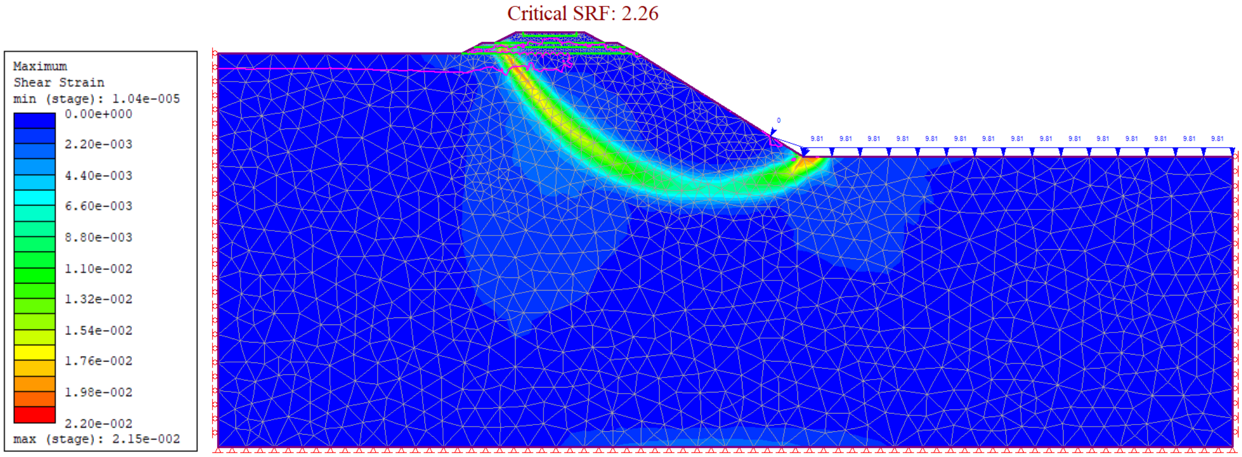

Figure 4. 7. (e) Maximum shear strain contour for the model with slope ratio = 2H:1V, H_r = 1 m, H_n = 5 m, and L/H = 0.8, (continued).

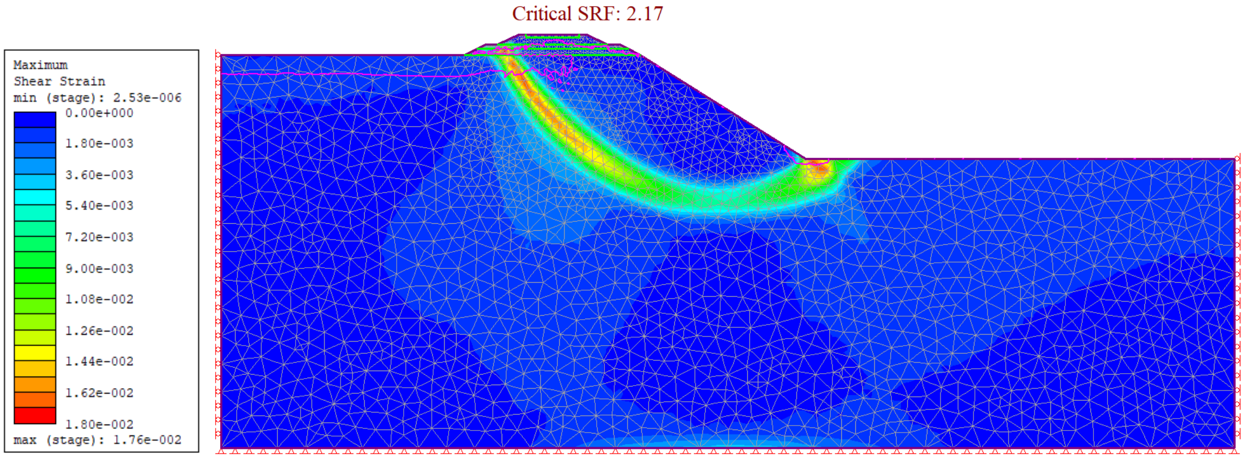

Figure 4. 7. (f) Maximum shear strain contour for the model with slope ratio = 2H:1V, H_r = 1 m, H_n = 5 m, and L/H =1.0, (continued).

Because of the hydrostatic load on the slope exerted by the body of water, the critical SRF increases to 3.74 without any rapid drawdown, while this value of the dry slope model was 2.66 (c.f. Figure 4.3 (d)). With a sudden decrease of water level, the critical SRF decreases from 3.74 to 2.17, since the low permeability of the soil blocks water inside the slope not allowing it to flow out instantly after the drawdown and pore water pressure persists, reducing the shear strength. It should be noted that the failure mechanism is global slope failure in most simulation results (Figures 4.7 (b) – (f)). Due to the relatively high permeabilities of railway embankment soil layers and the position of initial water level, suction causes the phreatic surface to climb up into the railway embankment, as shown in Figure 4.8 (a). When the water level is set to be 1 m (same as the natural slope height), the water has been sucked up into the railway embankment after the drawdown. By contrast, when the initial water level reduces to 0.4 m as shown in Figure 4.8 (b), a continuous water level below the railway embankment is obtained, in spite of a small portion of water (small pockets) still sucked up because of numerical noise in the solution phase.

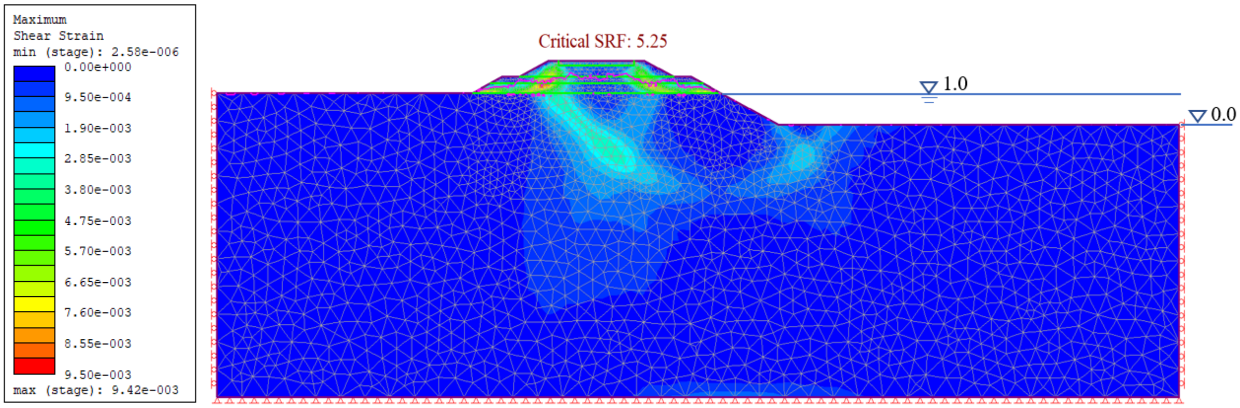

(a)

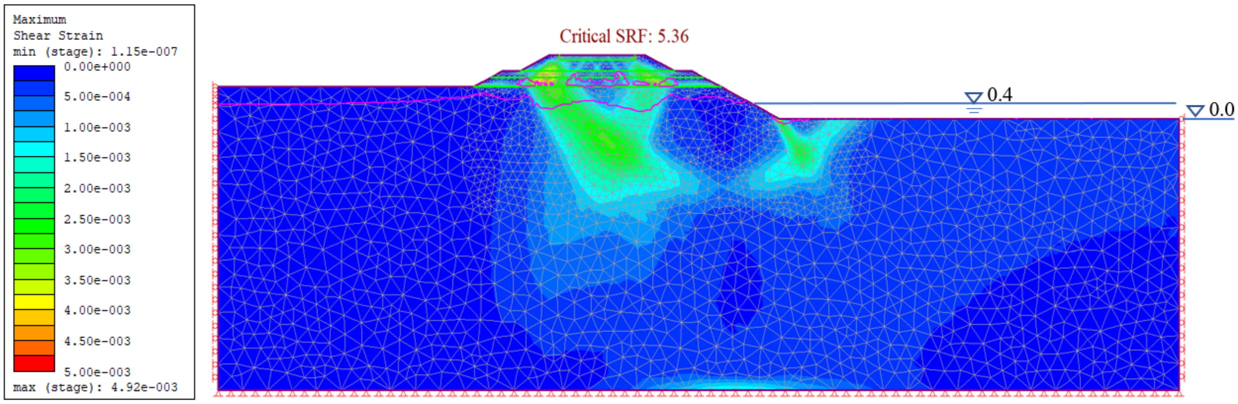

(b)

Figure 4. 8. Maximum shear strain contour for the model with slope ratio = 2H:1V, $H_r = 1$ m, $H_n = 1$ m when L/H =1.0 with different initial water levels: (a) 1 m and (b) 0.4 m.

The corresponding critical safety factors by SSR versus the maximum total displacements under different drawdown ratios are shown in Figure 4.9. Similar to Figure 4.4, the dense part has been enlarged in the inset and all critical safety factors are labeled.

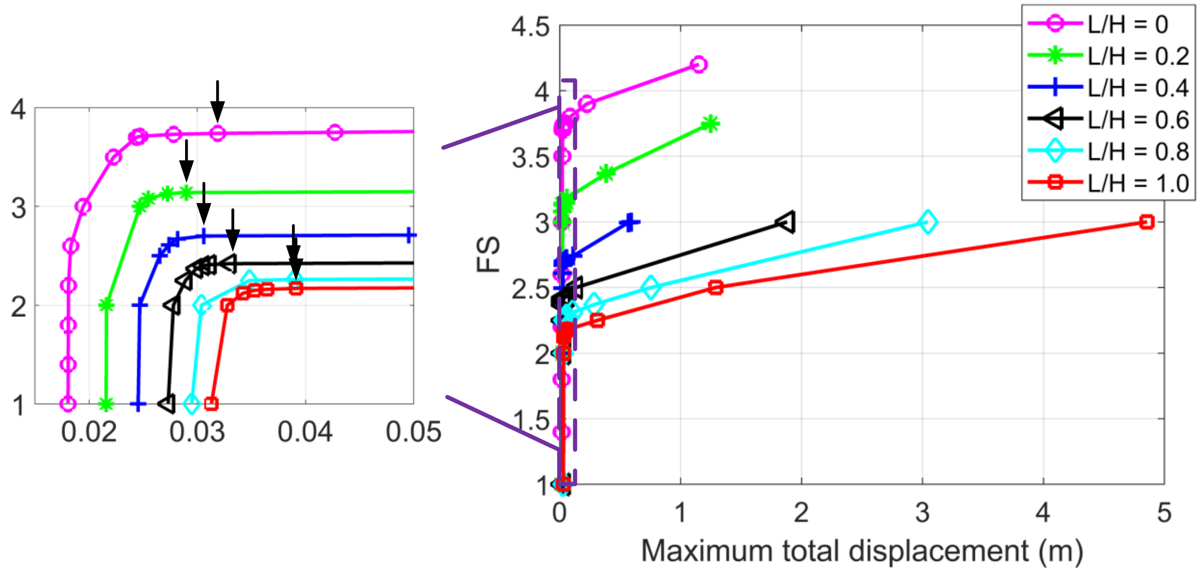

Figure 4. 9. Relationship between maximum total displacement and shear strength reduction factor for the models with slope ratio = 2H:1V, H_r = 1 m, H_n = 5 m under different drawdown ratios (L/H).

The critical safety factor decreases with a larger drawdown ratio. FS results, for all cases investigated in the model under rapid drawdown conditions, have been listed in Table 4.4. In each group, a higher rapid drawdown ratio causes a lower FS. The other trends are consistent with the case of a dry slope. For example, a higher natural slope height also has a negative influence on the FS of the slope.

Table 4. 4 FS results of cases in Set II

Groups	Subgroups	FS				
		Natural slope height (H_n) (m)				
		1	2	3	4	5
Group 3	Subgroup 7	6.17	5.87	5.61	5.41	5.25
	Subgroup 8	4.92	4.50	4.20	4.00	3.85
	Subgroup 9	4.19	3.74	3.42	3.20	3.08
	Subgroup 10	3.70	3.22	2.91	2.72	2.60
	Subgroup 11	3.14	2.70	2.42	2.26	2.17
Group 4	Subgroup 12	3.86	3.74	3.64	3.55	3.51
	Subgroup 13	2.93	2.79	2.68	2.60	2.54
	Subgroup 14	2.65	2.46	2.32	2.23	2.18
	Subgroup 15	2.44	2.22	2.07	1.97	1.91
	Subgroup 16	2.28	2.03	1.87	1.77	1.72
Group 5	Subgroup 17	2.96	3.00	2.85	2.80	2.77
	Subgroup 18	2.64	2.49	2.41	2.36	2.30
	Subgroup 19	2.37	2.28	2.14	2.08	2.00
	Subgroup 20	2.22	2.06	1.95	1.85	1.79
	Subgroup 21	2.09	1.91	1.78	1.70	1.64
Group 6	Subgroup 22	6.56	6.23	5.94	5.71	5.55
	Subgroup 23	5.39	4.91	4.56	4.33	4.14
	Subgroup 24	4.68	4.15	3.77	3.53	3.36
	Subgroup 25	4.19	3.63	3.26	3.01	2.86
	Subgroup 26	3.80	3.25	2.88	2.64	2.51
Group 7	Subgroup 27	4.19	4.07	3.98	3.90	3.84
	Subgroup 28	3.70	3.51	3.35	3.24	3.16
	Subgroup 29	3.39	3.13	2.94	2.81	2.72
	Subgroup 30	3.14	2.84	2.63	2.49	2.41
	Subgroup 31	2.95	2.63	2.40	2.25	2.17
Group 8	Subgroup 32	3.61	3.54	3.48	3.43	3.38
	Subgroup 33	3.24	3.11	3.03	2.90	2.84
	Subgroup 34	3.00	2.80	2.67	2.57	2.54
	Subgroup 35	2.79	2.59	2.43	2.31	2.24
	Subgroup 36	2.71	2.43	2.24	2.15	2.08

4.1.3 Set III: Model Under Both Rapid Drawdown and Freight Train Loads Conditions

After careful investigations of the cases in Set I and II, the next step is to study the model considering freight train loads and rapid drawdown conditions together (Set III).

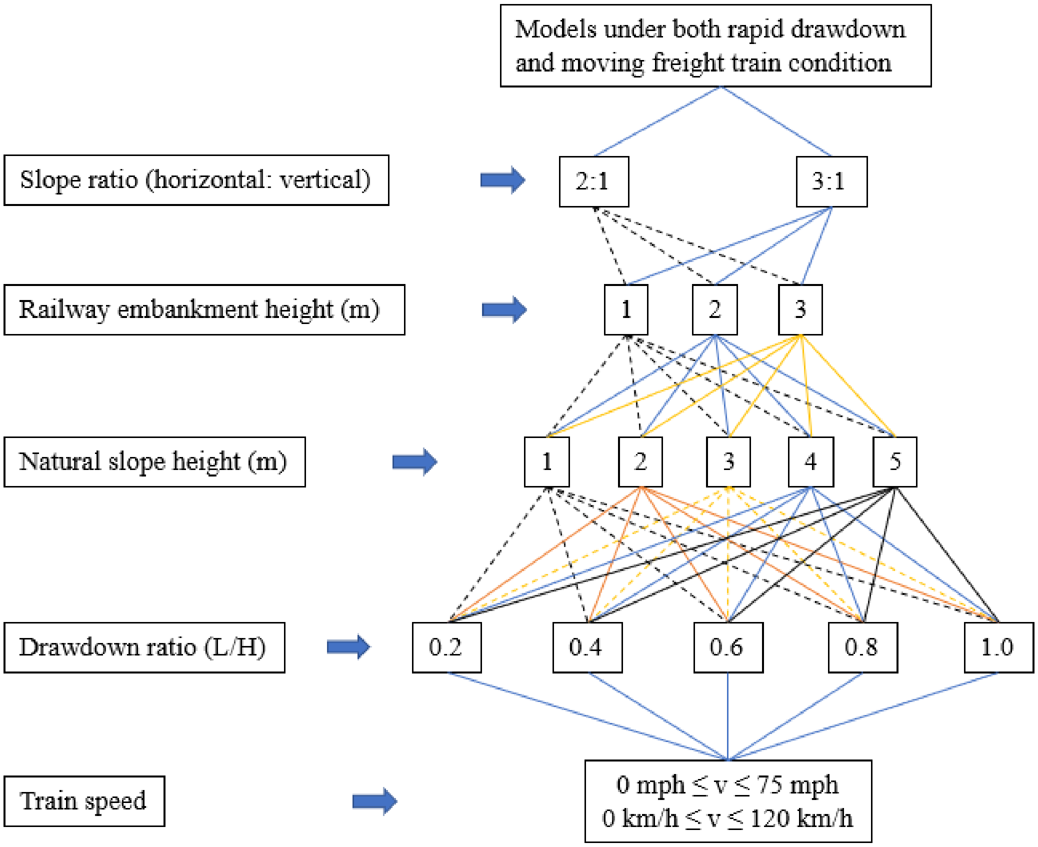

Figure 4. 10. Simplified dendrogram of various models including both moving freight train loads and rapid drawdown conditions.

Similar to Figure 4.1 and Figure 4.6, Figure 4.10 summarizes all combinations of five key parameters studied in the model under simultaneous moving train loads and rapid drawdown conditions, totally 1,025 cases. The maximum safe train speed is searched in a range of 0 mph (0 km/h) to 75 mph (120 km/h). Table 4.5 lists all combined cases, with 6 groups in total, consisting of 30 subgroups.

Table 4. 5 Cases in Set III – model under both train loads and rapid drawdown conditions

Groups	Subgroups	Slope ratio	H_r (m)	L/H	Number of H_n	Number of corresponding maximum safe train speed
Group 9	Subgroup 37	2:1	1	0.2	5	5
	Subgroup 38			0.4	5	5
	Subgroup 39			0.6	5	5
	Subgroup 40			0.8	5	5
	Subgroup 41			1.0	5	5
Group 10	Subgroup 42		2	0.2	5	5
	Subgroup 43			0.4	5	5
	Subgroup 44			0.6	5	5
	Subgroup 45			0.8	5	5
	Subgroup 46			1.0	5	5
Group 11	Subgroup 47		3	0.2	5	5
	Subgroup 48			0.4	5	5
	Subgroup 49			0.6	5	5
	Subgroup 50			0.8	5	5
	Subgroup 51			1.0	5	5
Group 12	Subgroup 52	3:1	1	0.2	5	5
	Subgroup 53			0.4	5	5
	Subgroup 54			0.6	5	5
	Subgroup 55			0.8	5	5
	Subgroup 56			1.0	5	5
Group 13	Subgroup 57		2	0.2	5	5
	Subgroup 58			0.4	5	5
	Subgroup 59			0.6	5	5
	Subgroup 60			0.8	5	5
	Subgroup 61			1.0	5	5
Group 14	Subgroup 62		3	0.2	5	5
	Subgroup 63			0.4	5	5
	Subgroup 64			0.6	5	5
	Subgroup 65			0.8	5	5
	Subgroup 66			1.0	5	5

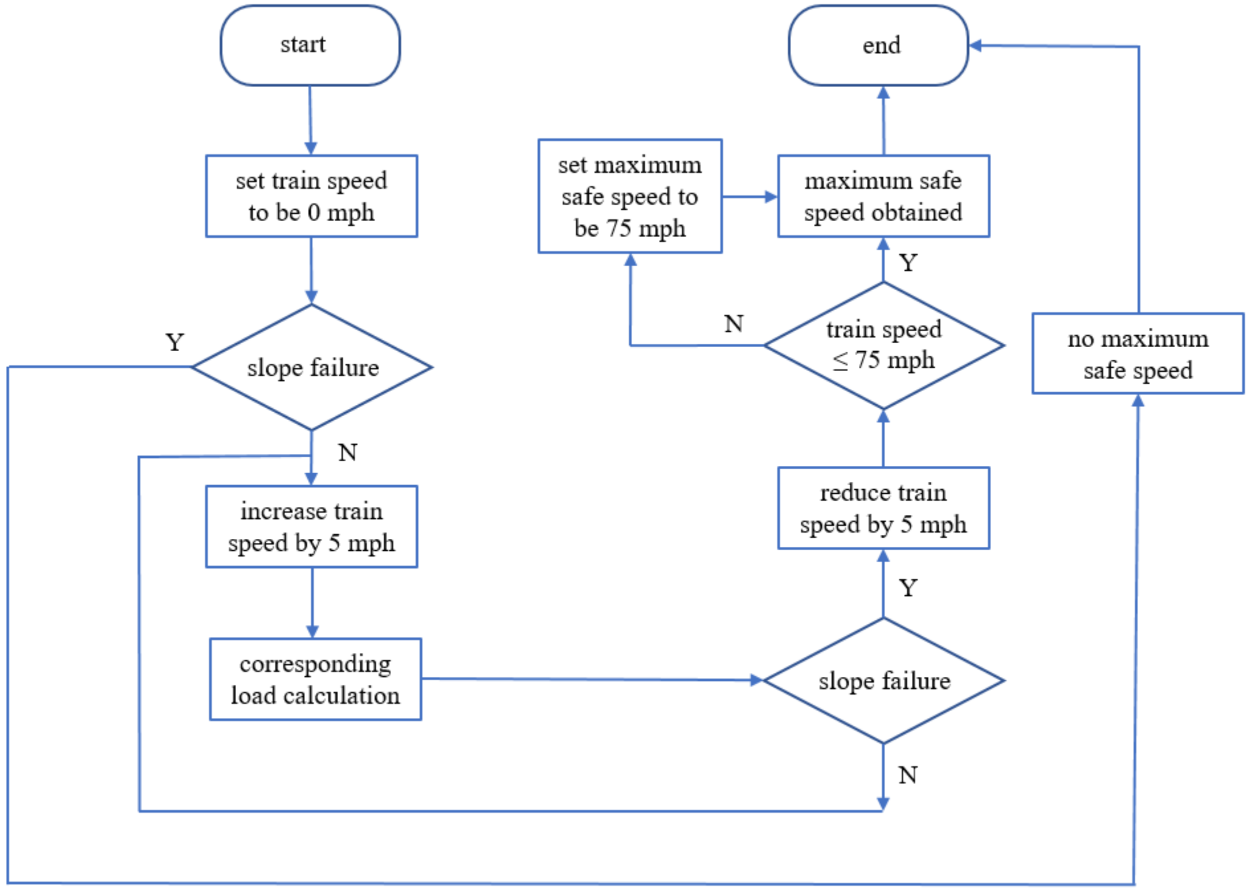

Figure 4. 11. Flowchart for calculating the maximum safe freight train speed.

A flowchart (Figure 4.11) shows the process to calculate the maximum safe train speed in several steps. All the train speeds mentioned in this process were calculated according to the train load applied on the bottom of the sleepers. The calculation step is 5 mph starting from an initial train speed (0 mph) to search for a possible slope failure state (FS < 1.3, refer to the explanation in Chapter 2.4.6). Note that in some cases, the load cannot be fully applied, which is also considered to be a failure state. Once the failure was detected, the speed was then reduced by 5 mph. If this speed is smaller than 75 mph, it is the maximum safe train speed. Otherwise, the maximum speed is set to be 75 mph. A special case is that even a stationary train on the track causes the damage to the slope. It is then considered as no maximum speed is attained. Through this calculation process, we can obtain the maximum safe train speed with respect to the applied train loads.

To directly capture the development of FS affected by the existence of rapid drawdown and train loads, the model with 2H:1V slope ratio, 1-meter railway embankment height, and 5-meter natural slope height, is still taken as an example. The maximum safe train speeds were achieved corresponding to the drawdown ratios of 0.2, 0.4, 0.6, 0.8, 1.0 which are discussed in Set II. Figures 4.12 (a) – (e) present the maximum shear strain contour of the chosen models with a stationary train.

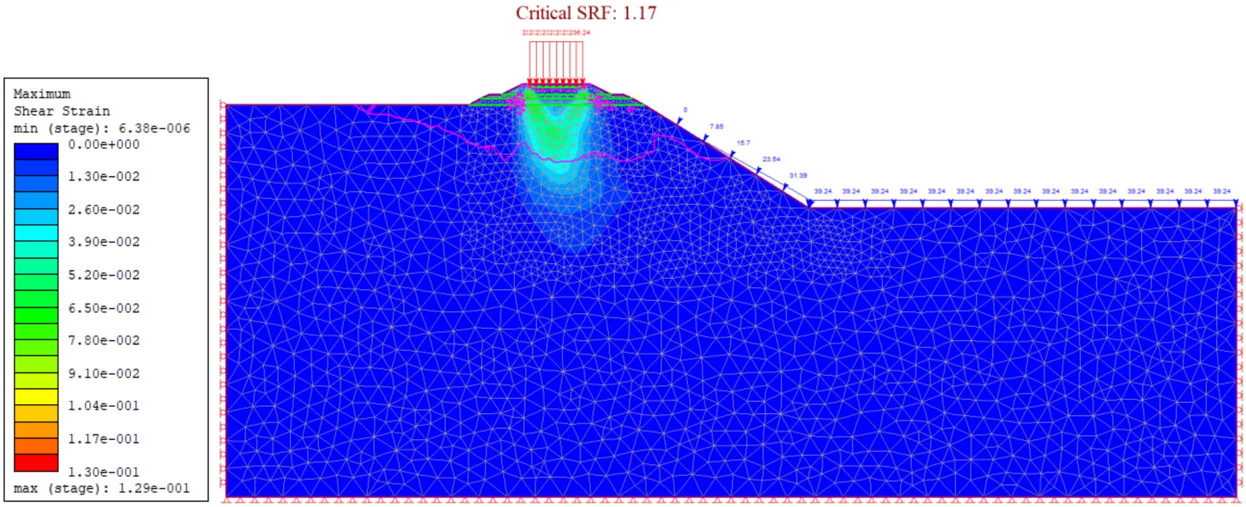

Figure 4. 12. (a) Maximum shear strain contour for the model with slope ratio = 2H:1V, H_r = 1 m, H_n = 5 m, and a stationary train when L/H = 0.2.

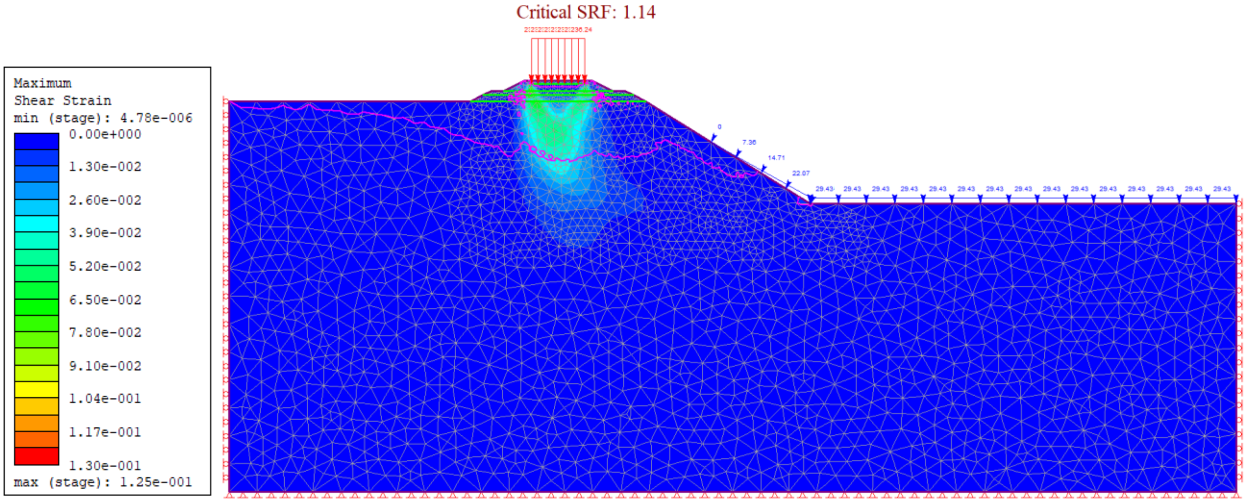

Figure 4. 12. (b) Maximum shear strain contour for the model with slope ratio = 2H:1V, H_r = 1 m, H_n = 5 m, and a stationary train when L/H = 0.4.

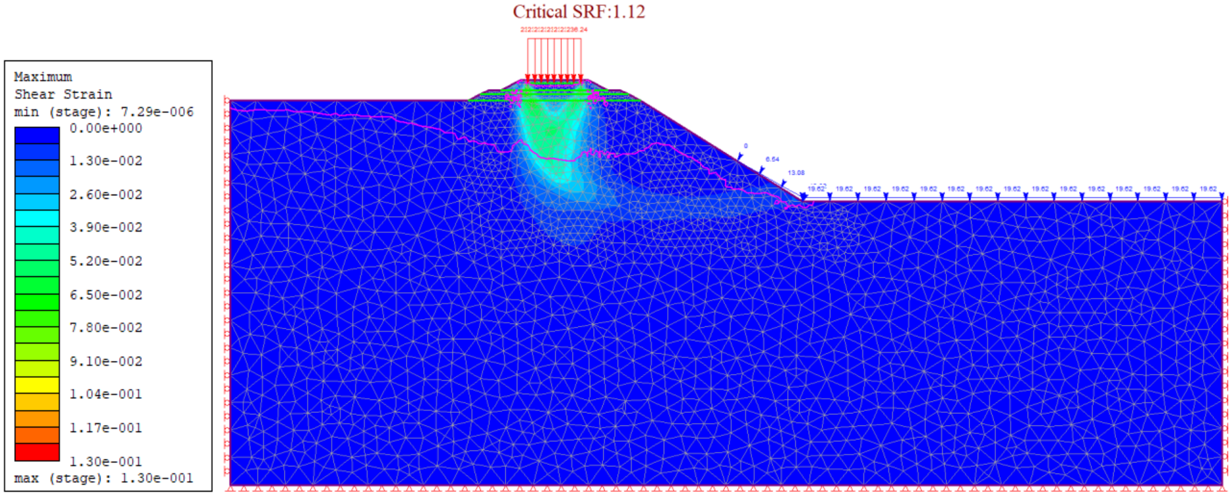

Figure 4. 12. (c) Maximum shear strain contour for the model with slope ratio = 2H:1V, H_r = 1 m, H_n = 5 m, and a stationary train when L/H = 0.6, (continued).

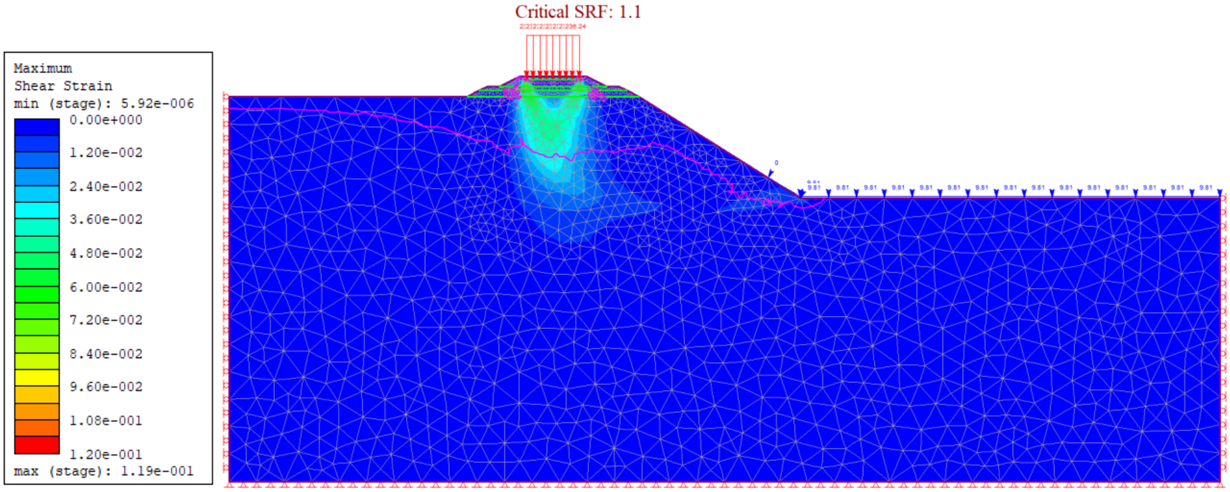

Figure 4. 12. (d) Maximum shear strain contour for the model with slope ratio = 2H:1V, H_r = 1 m, H_n = 5 m, and a stationary train when L/H = 0.8, (continued).

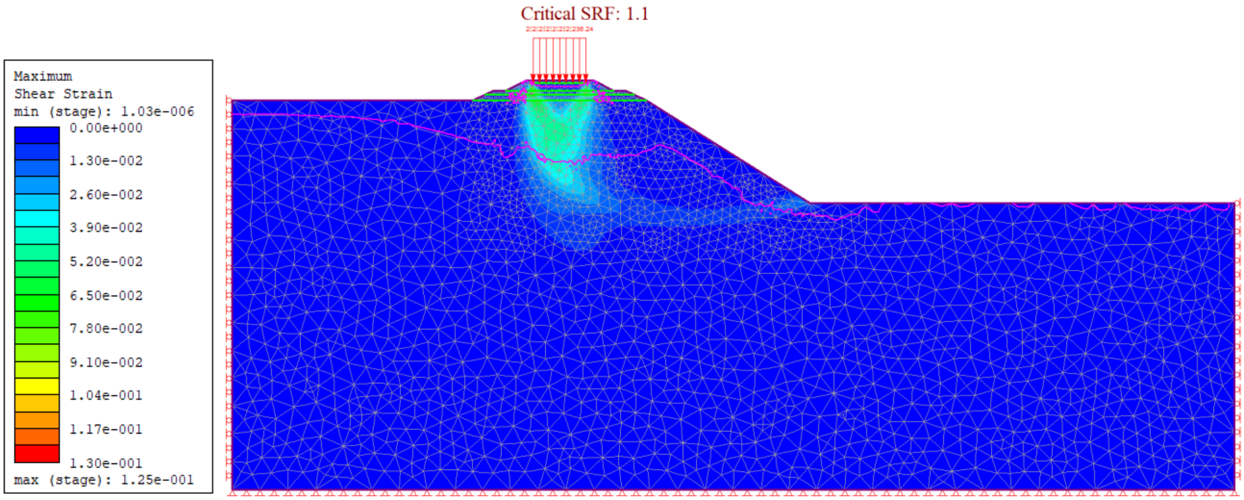

Figure 4. 12. (e) Maximum shear strain contour for the model with slope ratio = 2H:1V, $H_r = 1$ m, $H_n = 5$ m, and a stationary train when L/H = 1.0, (continued).

When the moving freight train loads are considered, a foundation failure turns out to be the main failure mechanism. In addition, the external train load added in the models lowers the phreatic surface. All the safety factors in Figure 4.12 are less than 1.3 which is the required safety factor for slopes under rapid drawdown in this thesis. Under this circumstance, the freight train could not cross or park on the area where a rapid drawdown occurs or have occurred.

Table 4.6 summarizes the results of safety factors for all the models in Set III with a stationary train on the railway embankment. It is noted that some cases have unstable slopes whose safety factors are less than 1.3 after a rapid drawdown. In those models, no maximum safe train speed is accepted, in other words, the freight train has to avoid passing or parking on the track. Table 4.7 shows the maximum safe train speeds in both mph and km/h units for each case listed in Table 4.5. If the maximum safe train speed is equal to or greater than 0 mph (km/h), it means the slope is stable with the stationary freight train on the track (maximum safe train speed = 0 mph) or the moving train (maximum safe train speed > 0 mph).

Therefore, all the corresponding FS results for all cases in Groups 9-12 are listed in Table 4.8. Further discussions regarding the maximum safe train speeds and FS results will be addressed afterwards, in Section 4.2.

Table 4. 6 FS results of cases with a stationary train (static train load) in Set III

Groups	Subgroups	FS				
		Natural slope height (Hn) (m)				
		1	2	3	4	5
Group 9	Subgroup 37	1.28	1.24	1.23	1.22	1.17
	Subgroup 38	1.28	1.23	1.21	1.19	1.14
	Subgroup 39	1.27	1.22	1.21	1.18	1.12
	Subgroup 40	1.27	1.21	1.20	1.17	1.10
	Subgroup 41	1.28	1.21	1.19	1.16	1.10
Group 10	Subgroup 42	1.86	1.20	1.17	1.16	1.15
	Subgroup 43	1.65	1.19	1.15	1.13	1.11
	Subgroup 44	1.65	1.18	1.14	1.11	1.09
	Subgroup 45	1.65	1.18	1.13	1.10	1.07
	Subgroup 46	1.64	1.17	1.13	1.09	1.07
Group 11	Subgroup 47	1.69	1.62	1.52	1.46	1.38
	Subgroup 48	1.68	1.60	1.51	1.43	1.36
	Subgroup 49	1.74	1.59	1.50	1.40	1.35
	Subgroup 50	1.66	1.57	1.45	1.37	1.27
	Subgroup 51	1.65	1.56	1.41	1.30	1.25
Group 12	Subgroup 52	1.32	1.29	1.30	1.30	1.29
	Subgroup 53	1.31	1.29	1.28	1.28	1.28
	Subgroup 54	1.30	1.29	1.28	1.27	1.27
	Subgroup 55	1.30	1.28	1.27	1.27	1.26
	Subgroup 56	1.30	1.28	1.27	1.27	1.26
Group 13	Subgroup 57	1.39	1.38	1.37	1.36	1.36
	Subgroup 58	1.39	1.37	1.35	1.34	1.34
	Subgroup 59	1.38	1.36	1.34	1.33	1.32
	Subgroup 60	1.38	1.35	1.34	1.32	1.30
	Subgroup 61	1.39	1.34	1.33	1.32	1.29
Group 14	Subgroup 62	1.94	1.90	1.76	1.75	1.69
	Subgroup 63	2.00	1.88	1.78	1.65	1.67
	Subgroup 64	2.00	1.86	1.74	1.74	1.60
	Subgroup 65	2.00	1.85	1.71	1.64	1.58
	Subgroup 66	1.91	1.84	1.69	1.61	1.54

Table 4. 7 Calculated maximum safe train speed for cases in Set III

Groups	Subgroups	Maximum safe train speed									
		mph					km/h				
		Natural slope height (Hn) (m)					Natural slope height (Hn) (m)				
		1	2	3	4	5	1	2	3	4	5
Group 9	Subgroup 37	\	\	\	\	\	\	\	\	\	\
	Subgroup 38	\	\	\	\	\	\	\	\	\	\
	Subgroup 39	\	\	\	\	\	\	\	\	\	\
	Subgroup 40	\	\	\	\	\	\	\	\	\	\
	Subgroup 41	\	\	\	\	\	\	\	\	\	\
Group 10	Subgroup 42	5	\	\	\	\	8	\	\	\	\
	Subgroup 43	5	\	\	\	\	8	\	\	\	\
	Subgroup 44	5	\	\	\	\	8	\	\	\	\
	Subgroup 45	5	\	\	\	\	8	\	\	\	\
	Subgroup 46	5	\	\	\	\	8	\	\	\	\
Group 11	Subgroup 47	25	20	20	20	20	40	32	32	32	32
	Subgroup 48	25	15	15	15	10	40	24	24	24	16
	Subgroup 49	25	15	15	15	5	40	24	24	24	8
	Subgroup 50	25	15	15	15	\	40	24	24	24	\
	Subgroup 51	25	15	15	15	\	40	24	24	24	\
Group 12	Subgroup 52	5	\	\	\	\	8	\	\	\	\
	Subgroup 53	0	\	\	\	\	0	\	\	\	\
	Subgroup 54	0	\	\	\	\	0	\	\	\	\
	Subgroup 55	0	\	\	\	\	0	\	\	\	\
	Subgroup 56	0	\	\	\	\	0	\	\	\	\
Group 13	Subgroup 57	25	20	15	15	15	40	32	24	24	24
	Subgroup 58	25	20	15	10	5	40	32	24	16	8
	Subgroup 59	25	15	10	5	5	40	24	16	8	8
	Subgroup 60	25	10	5	5	0	40	16	8	8	0
	Subgroup 61	25	10	5	5	\	40	16	8	8	\
Group 14	Subgroup 62	75	75	75	75	75	120	120	120	120	120
	Subgroup 63	75	75	75	75	75	120	120	120	120	120
	Subgroup 64	75	75	75	75	75	120	120	120	120	120
	Subgroup 65	75	75	75	75	75	120	120	120	120	120
	Subgroup 66	75	75	75	75	75	120	120	120	120	120

Table 4. 8 FS results of cases with the maximum train speeds in Set III

Groups	Subgroups	FS				
		Natural slope height (Hn) (m)				
		1	2	3	4	5
Group 9	Subgroup 37	\	\	\	\	\
	Subgroup 38	\	\	\	\	\
	Subgroup 39	\	\	\	\	\
	Subgroup 40	\	\	\	\	\
	Subgroup 41	\	\	\	\	\
Group 10	Subgroup 42	1.72	\	\	\	\
	Subgroup 43	1.66	\	\	\	\
	Subgroup 44	1.66	\	\	\	\
	Subgroup 45	1.64	\	\	\	\
	Subgroup 46	1.63	\	\	\	\
Group 11	Subgroup 47	1.71	1.59	1.53	1.42	1.35
	Subgroup 48	1.66	1.57	1.51	1.36	1.31
	Subgroup 49	1.64	1.57	1.40	1.36	1.34
	Subgroup 50	1.62	1.52	1.40	1.31	\
	Subgroup 51	1.60	1.52	1.39	1.31	\
Group 12	Subgroup 52	1.30	\	\	\	\
	Subgroup 53	1.31	\	\	\	\
	Subgroup 54	1.30	\	\	\	\
	Subgroup 55	1.30	\	\	\	\
	Subgroup 56	1.30	\	\	\	\
Group 13	Subgroup 57	1.30	1.30	1.31	1.30	1.30
	Subgroup 58	1.30	1.30	1.30	1.30	1.31
	Subgroup 59	1.30	1.30	1.30	1.30	1.30
	Subgroup 60	1.30	1.31	1.31	1.30	1.30
	Subgroup 61	1.30	1.30	1.31	1.30	\
Group 14	Subgroup 62	1.80	1.76	1.66	1.61	1.55
	Subgroup 63	1.79	1.77	1.63	1.48	1.52
	Subgroup 64	1.80	1.74	1.61	1.48	1.44
	Subgroup 65	1.80	1.75	1.49	1.45	1.42
	Subgroup 66	1.78	1.70	1.48	1.42	1.43

4.2 Parametric Study of Models in Set I and II

Simulation results of both Sets I and II are discussed in this section. FS results versus each parameter for models in Set I and II are demonstrated. Specifically, parameters of the natural slope height, railway embankment height, and slope ratio are investigated for models in Set I. While for models in Set II, the rapid drawdown ratio is added besides those in Set I. The development trends of FS are clearly shown to offer a comprehensive picture how FS interacts with each parameter.

4.2.1 Comparison of Simulation Results for Models in Set I

The geometric parameters studied in this model are the natural slope height, railway embankment height, and slope ratio, as shown in Figure 4.1. Two graphs in Figure 4.13 plot FS results as a function of natural slope heights with all cases in Group 1 and 2 correspondings to the three railway embankment heights considered. As can be seen from both graphs, higher railway embankment heights reduce FS results. Meanwhile, larger natural slope heights generally have a negative influence on the slope stability according to the curve trends. Also, a flatter slope makes the whole structure more stable.

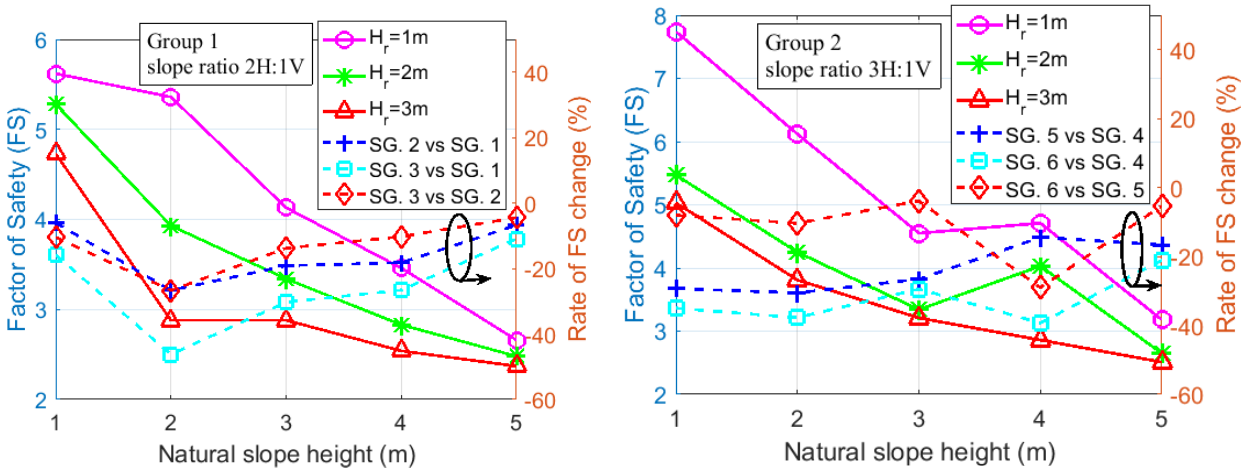

(a) (b)

Figure 4. 13. FS results and FS change between subgroups versus natural slope heights in a range of 1 m to 5 m with three railway embankment heights. Slope ratios are (a) 2H:1V and (b) 3H:1V.

The change of FS results for each subgroup (SG.) in Group 1 and 2 are also presented in Figure 4.13. The FS change is evaluated by Equation (4.2), as follows:

$$R_F = \frac{FS_n a - FS_m a}{FS_m a} \tag{4.2}$$

where R_F is the rate of FS change, n or m is the subgroup number to be compared (n, m = 1, 2, 3), and a is the natural slope height (a = 1, 2, 3, 4, 5). For example, if FS results in subgroup 2 are compared to those in subgroup 1 when natural slope height is 1 m, the calculation of R_F is $\frac{FS_2 1 - FS_1 1}{FS_1 1} = \frac{5.28 - 5.62}{5.62} = -6.05\ \%$. It means FS is reduced by 6.05 % for the model with 1-meter natural slope height when increasing the railway embankment height from 1 m to 2 m.

It can also be observed that the reduction ratio of FS for each subgroup gradually drops with the increment of the natural slope height. Similarly, the increment of railway embankment height cuts down the reduction ratio of FS for each group.

Among all models studied in Set I, the lowest FS of 2.37 was captured for the model in subgroup 3 with a 5-meter natural slope height. Note that this FS value is much higher than the threshold 1.3, thus rapid drawdown conditions can be introduced on top of models in Set I which actually form models in Set II.

4.2.2 Comparison of Simulation Results for Models in Set II

Figure 4.14 shows FS results of models in Group 3 – 8 as well as the rate of FS change between subgroups within each group. Upper subplots show FS results and lower ones are for the rate of FS change. FS values of first subgroup models in each group act as a reference to calculate the rate of FS change. In the analysis, slope ratios are 2H:1V and 3H:1V, while the drawdown ratios are set to be 0.2, 0.4, 0.6, 0.8, 1.0.

The influence of various natural slope heights, railway embankment heights and slope ratios are similar to those observed in Set I. For example, smaller natural slope heights, railway embankment heights and flatter slope can help stabilize the slope. When the slope ratio is set to be 2H:1V or 3H:1V, trends of FS curves in Figure 4.14 for each group are almost the same with different railway embankment heights. However, the FS curve with 0.2 drawdown ratio is much larger (at least 10 %) than other counterparts in each graph, indicating that the increase of drawdown ratio is a notable factor that may bring negative influence to the slope safety. With a larger natural slope height in each subgroup, the rate of FS change slightly decreases. It can also be observed that the rate of FS changes increases by around 10 % when the L/H ratio increases by 0.2.

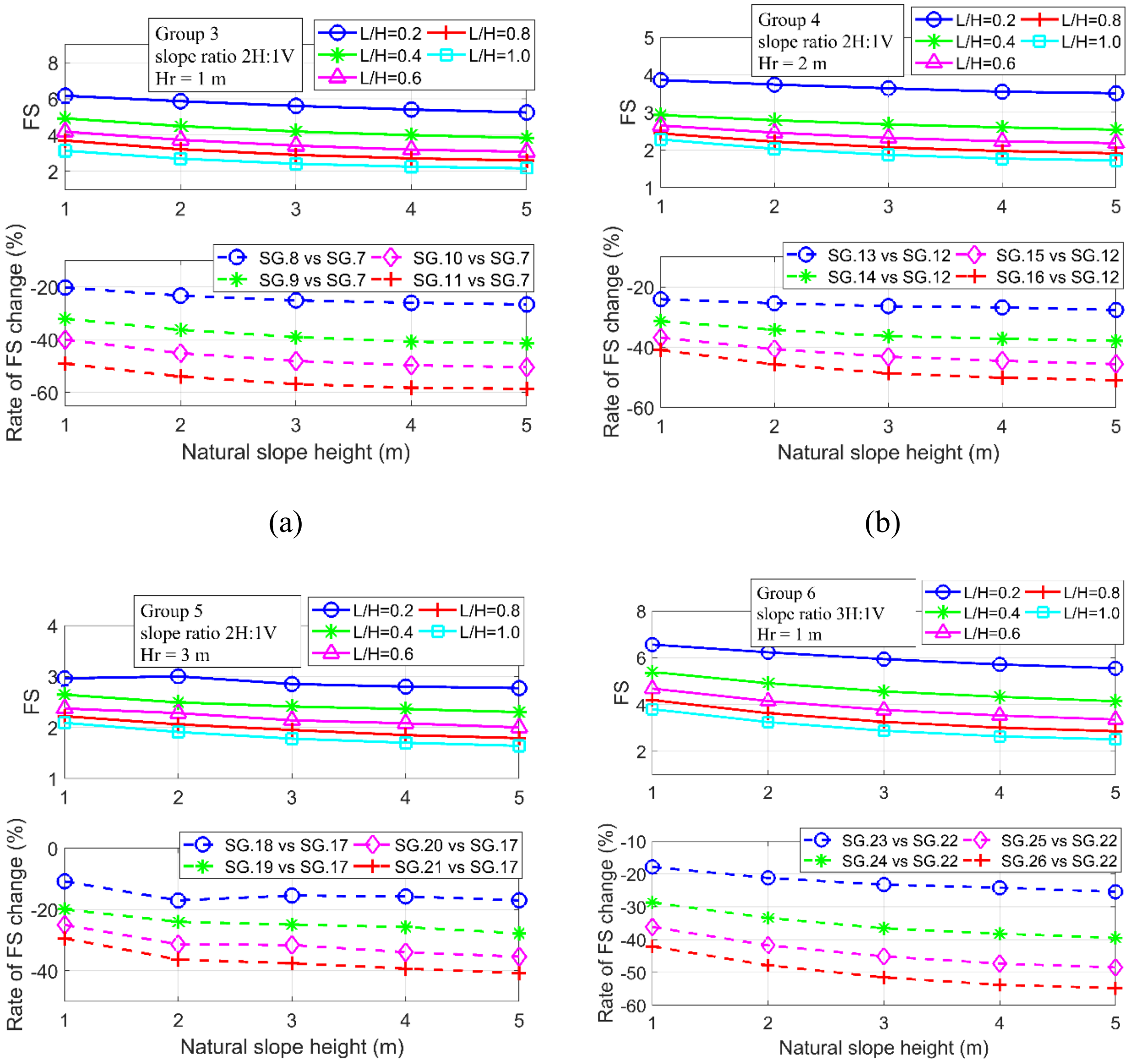

(a) (b)

(c) (d)

Figure 4. 14. FS results and rate of FS change versus natural slope height (in a range of 1 m to 5 m) with three railway embankment heights (1m, 2m, and 3m). All cases in Set II are divided into (a) Group 3, (b) Group 4, (c) Group 5, (d) Group 6;

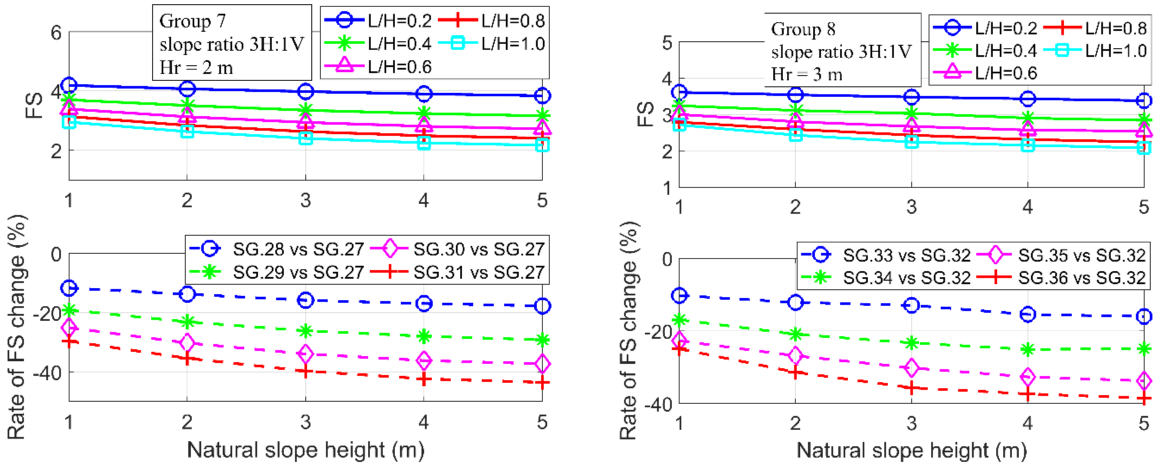

(e) (f)

Figure 4. 14. FS results and rate of FS change versus natural slope height (in a range of 1 m to 5 m) with three railway embankment heights (1m, 2m, and 3m). (e) Group 7, and (f) Group 8, (continued).

The lowest FS in Set II is 1.64 for the case in subgroup 21 with a 5-meter natural slope height, which is still higher than threshold 1.3. Therefore, all models are still stable for further analysis which has simultaneously rapid drawdown and train load conditions in Set III.

4.3 Results Discussion of Set III

4.3.1 Influence of Slope Geometry for the Model Under Train Loads and Rapid Drawdown Conditions

Firstly, Figures 4.15 (a) – (f) present the FS results of models in Group 9 to 14 with a stationary train in Set III, as well as the change of FS within each group. FS values of first subgroup models in each group act as the reference to calculate the rate of FS change. Slope ratios are set to be 2H:1V and 3H:1V. Drawdown ratios are 0.2, 0.4, 0.6, 0.8, 1.0. Different from the above conclusions in Set I and Set II, the slope with a stationary train on the track (under static load) is the most stable when the railway embankment height is 3 m (Group 11) as shown in Figure 4.15 (c) and (f). This is mainly because the strength of embankment is much higher than that of the natural slope, and the majority of slip surface concentrates in the embankment (with 3 m railway embankment height). With the train loads added on the track, the location of the slip surface changes compared to the case without train loads, which determines the magnitude of the factor of safety. Thus, the influence of slope geometry and train speed for models in Set III are discussed in more details in this section, which have five aspects:

(a) influence of the slope ratio,

(b) influence of the railway embankment height,

(c) influence of the natural slope height,

(d) influence of the drawdown ratio, and

(e) influence of the train speed.

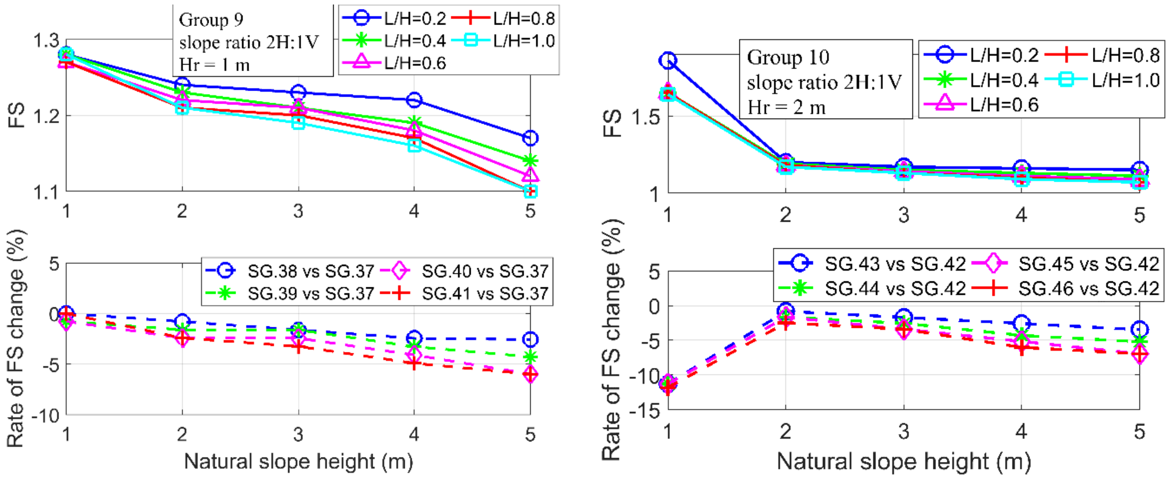

(a) (b)

Figure 4. 15. FS results with a stationary train on the track and the rate of FS change versus natural slope height (in a range of 1 m to 5 m) with three railway embankment heights (1m, 2m, and 3m). All cases in Set III are divided into (a) Group 9, (b) Group 10;

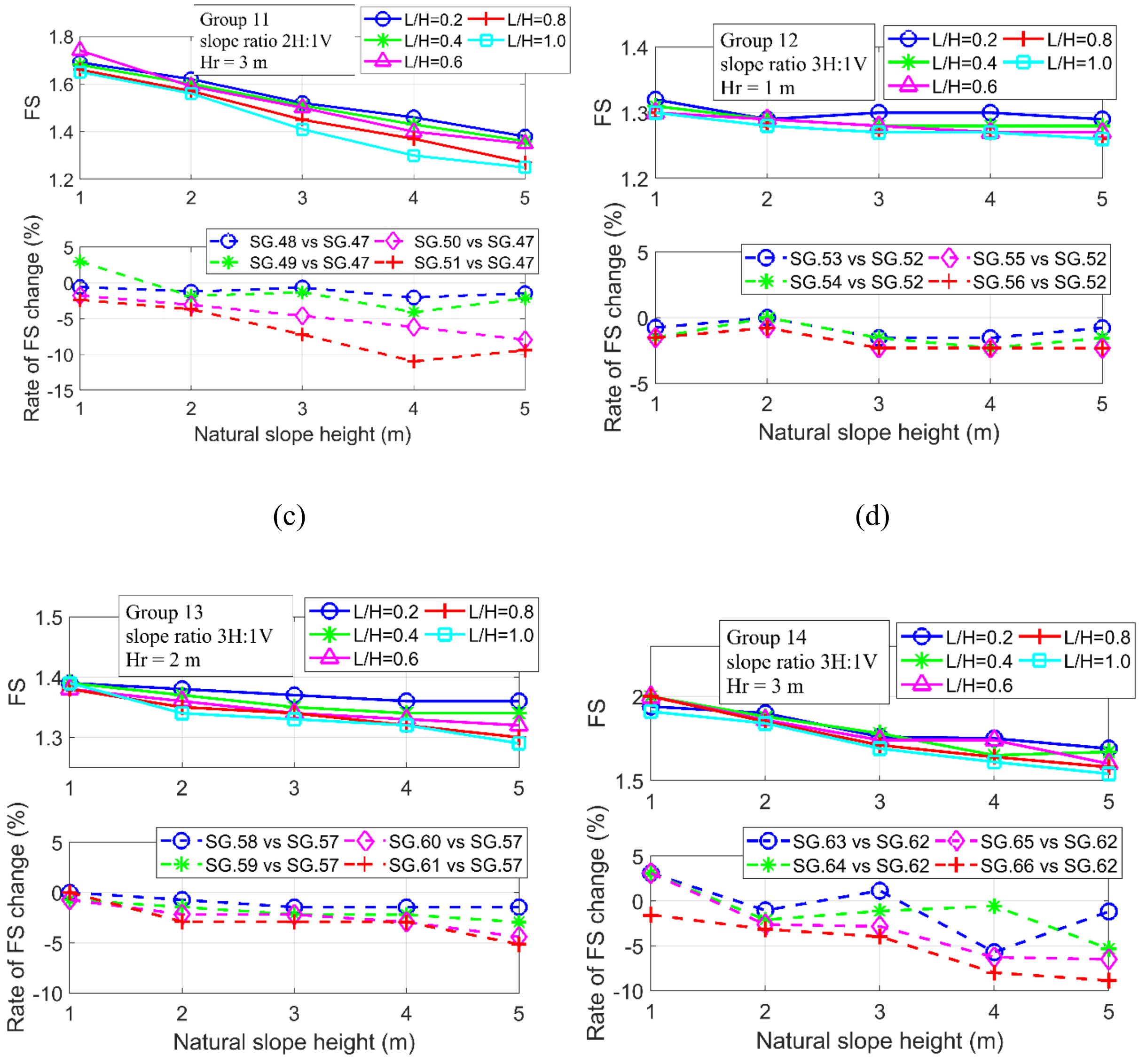

(c) (d)

(e) (f)

Figure 4. 15. FS results with a stationary train on the track and the rate of FS change versus natural slope height (in a range of 1 m to 5 m) with three railway embankment heights (1m, 2m, and 3m). All cases in Set III are divided into (c) Group 11, (d) Group 12, (e) Group 13, and (f) Group 14, (continued).

(a) Influence of the slope ratio

Table 4.9 describes the FS results of models in Group 9 (2H:1V) and Group 12 (3H:1V) with the same H_r (1 m) and the corresponding ratio of FS change when the slope ratio increases from 2H:1V to 3H:1V. All the values of FS change are positive, indicating that FS results increase with a flatter slope. The increment of FS results is at least 1.56 %. With a 5-m natural slope height and drawdown ratios of 0.8 and 1.0, the increment of FS results reaches the peak of 14.55 % when slope ratio increases from 2H:1V to 3H:1V.

Table 4. 9 Comparison of FS results and FS change rate of models in Group 9 and 12 under static load (slope ratio of 2H:1V versus 3H:1V).

Groups	Subgroups	FS				
		Natural slope height (Hn) (m)				
		1	2	3	4	5
Group 9	Subgroup 37	1.28	1.24	1.23	1.22	1.17
Group 12	Subgroup 52	1.32	1.29	1.30	1.30	1.29
Rate of FS change (%)		**3.13**	**4.03**	**5.69**	**6.56**	**10.26**
Group 9	Subgroup 38	1.28	1.23	1.21	1.19	1.14
Group 12	Subgroup 53	1.31	1.29	1.28	1.28	1.28
Rate of FS change (%)		**2.34**	**4.88**	**5.79**	**7.56**	**12.28**
Group 9	Subgroup 39	1.27	1.22	1.21	1.18	1.12
Group 12	Subgroup 54	1.30	1.29	1.28	1.27	1.27
Rate of FS change (%)		**2.36**	**5.74**	**5.79**	**7.63**	**13.39**
Group 9	Subgroup 40	1.27	1.21	1.20	1.17	1.10
Group 12	Subgroup 55	1.30	1.28	1.27	1.27	1.26
Rate of FS change (%)		**2.36**	**5.79**	**5.83**	**8.55**	**14.55**
Group 9	Subgroup 41	1.28	1.21	1.19	1.16	1.10
Group 12	Subgroup 56	1.30	1.28	1.27	1.27	1.26
Rate of FS change (%)		**1.56**	**5.79**	**6.72**	**9.48**	**14.55**

The values of FS change rates are summarized and plotted in Figure 4.16, from which can be observed that a higher natural slope height leads to a higher FS change rate due to slope ratio variation. This trend is valid for all drawdown ratios. Moreover, FS change rate due to slope ratio increase is insensitive to the drawdown ratio, showing negligible differences. Thus, it is strongly recommended to design the slope with a ratio of 3H:1V if FS results are not satisfying to stabilize the slope.

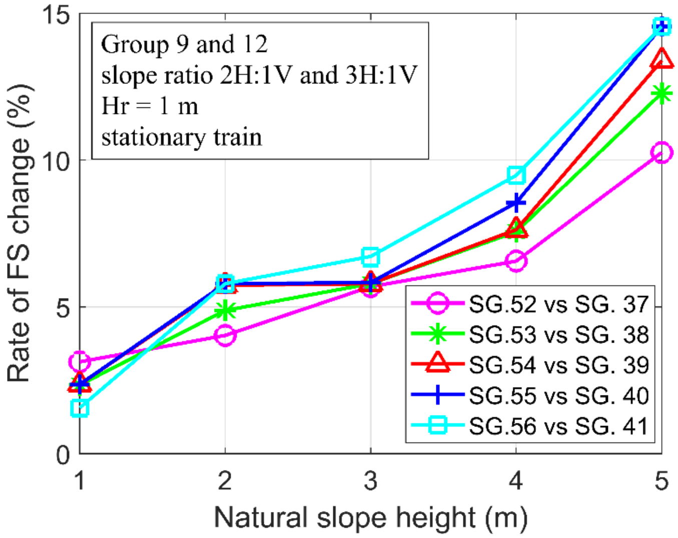

Figure 4. 16. Relationship between FS change rate and the natural slope height for models in Group 9 and 12 with a stationary train.

(b) Influence of the railway embankment height

The railway embankment height varies from 1 m to 3 m in this study. Thus, two sets of comparison are presented in this section, H_r = 2 m (Group 10) versus H_r = 1 m (Group 9) listed in Table 4.10, and H_r = 3 m (Group 11) versus H_r = 1 m (Group 9) listed in Table 4.11.

As can be seen in Table 4.10, when natural slope height is 1 m, increasing embankment height from 1 m to 2 m is helpful to get a larger FS. Since the strength of embankment is much higher than that of the natural slope, higher embankment height is prone to keeping the majority of slip surface inside the embankment structure. When natural slope height is only 1 m, embankment height is a dominant factor and thus its increase leads to the noticeable increase of FS. When natural slope height is larger than 1 m, the change of railway embankment height has less impact than that of natural slope height. Thus, FS declines if embankment height changes from 1 m to 2 m in this case. But FS degradation is not severe, with the largest negative change rate of 6.03 %. As can be seen in Figure 4.17, the drawdown ratio does not bring an obvious influence on the FS change rate, except when the drawdown ratio is 0.2 at which FS increment is much larger than the rest.

Table 4. 10 Comparison of FS results and FS change rate of models in Group 9 and 10 under static load (railway embankment height of 1 m versus 2 m).

Groups	Subgroups	FS				
		Natural slope height (Hn) (m)				
		1	2	3	4	5
Group 9	Subgroup 37	1.28	1.24	1.23	1.22	1.17
Group 10	Subgroup 42	1.86	1.20	1.17	1.16	1.15
Rate of FS change (%)		**45.31**	**-3.23**	**-4.88**	**-4.92**	**-1.71**
Group 9	Subgroup 38	1.28	1.23	1.21	1.19	1.14
Group 10	Subgroup 43	1.65	1.19	1.15	1.13	1.11
Rate of FS change (%)		**28.91**	**-3.25**	**-4.96**	**-5.04**	**-2.63**
Group 9	Subgroup 39	1.27	1.22	1.21	1.18	1.12
Group 10	Subgroup 44	1.65	1.18	1.14	1.11	1.09
Rate of FS change (%)		**29.92**	**-3.28**	**-5.79**	**-5.93**	**-2.68**
Group 9	Subgroup 40	1.27	1.21	1.20	1.17	1.10
Group 10	Subgroup 45	1.65	1.18	1.13	1.10	1.07
Rate of FS change (%)		**29.92**	**-2.48**	**-5.83**	**-5.98**	**-2.73**
Group 9	Subgroup 41	1.28	1.21	1.19	1.16	1.10
Group 10	Subgroup 46	1.64	1.17	1.13	1.09	1.07
Rate of FS change (%)		**28.13**	**-3.31**	**-5.04**	**-6.03**	**-2.73**

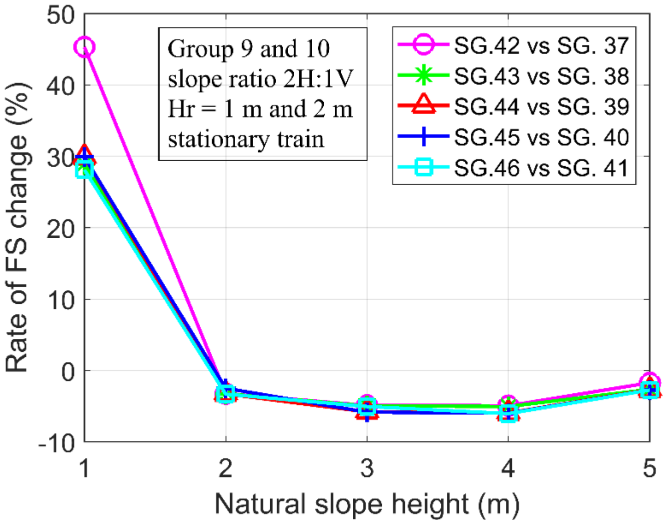

Figure 4. 17. Relationship between FS change rate of railway embankment height (1 m and 2 m) and natural slope height for models in Group 9 and 10 with a stationary train.

Table 4.11 shows the comparison of FS results with embankment heights of 1 m and 3 m. Unlike the data shown in Table 4.10, all FS values augment with a larger embankment height. When the drawdown ratio is 0.6, FS increments are relatively larger as shown in Figure 4. 18. By contrast, it can be noted that FS increments are the lowest with 1.0 drawdown ratio, for all natural slope heights. Thus, 3-meter railway embankment height is a better choice to build a more stable slope under external static load conditions.

Table 4. 11 Comparison of FS results and FS change rate of models in Group 9 and 11 under static load (railway embankment height of 1 m versus 3 m).

Groups	Subgroups	FS				
		Natural slope height (Hn) (m)				
		1	2	3	4	5
Group 9	Subgroup 37	1.28	1.24	1.23	1.22	1.17
Group 11	Subgroup 47	1.69	1.62	1.52	1.46	1.38
Rate of FS change (%)		**32.03**	**30.65**	**23.58**	**19.67**	**17.95**
Group 9	Subgroup 38	1.28	1.23	1.21	1.19	1.14
Group 11	Subgroup 48	1.68	1.60	1.51	1.43	1.36
Rate of FS change (%)		**31.25**	**30.08**	**24.79**	**20.17**	**19.30**
Group 9	Subgroup 39	1.27	1.22	1.21	1.18	1.12
Group 11	Subgroup 49	1.74	1.59	1.50	1.40	1.35
Rate of FS change (%)		**37.01**	**30.33**	**23.97**	**18.64**	**20.54**
Group 9	Subgroup 40	1.27	1.21	1.20	1.17	1.10
Group 11	Subgroup 50	1.66	1.57	1.45	1.37	1.27
Rate of FS change (%)		**30.71**	**29.75**	**20.83**	**17.09**	**15.45**
Group 9	Subgroup 41	1.28	1.21	1.19	1.16	1.10
Group 11	Subgroup 51	1.65	1.56	1.41	1.30	1.25
Rate of FS change (%)		**28.91**	**28.93**	**18.49**	**12.07**	**13.64**

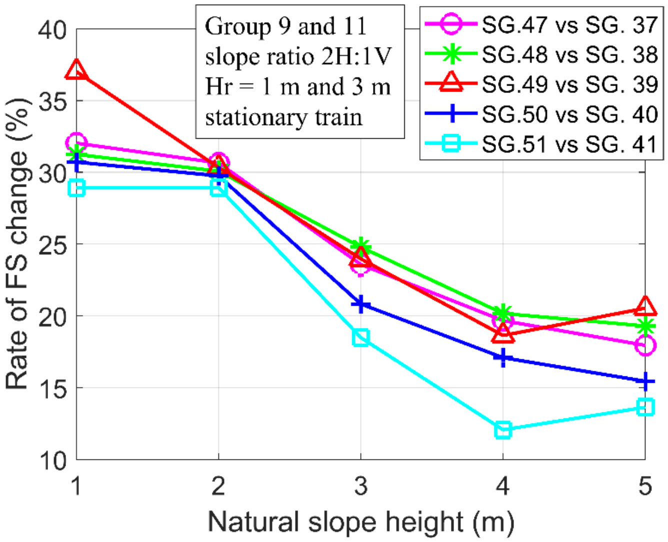

Figure 4. 18. Relationship between FS change rate of railway embankment height (1 m and 3 m) and natural slope height for models in Group 9 and 11 with a stationary train.

(c) Influence of the natural slope height

In this section, how different natural slope heights affect the FS results are studied. Three batches of comparison are sorted out according to different railway embankment heights (H_r = 1m, 2m, and 3m). Within each comparison, FS values with natural slope heights larger than 1 m are compared to that with 1-m height (the first column of FS results in each table). Table 4.12 shows FS results and FS change rate due to the variations of natural slope height when H_r = 1m. It is clearly observed that with larger natural slope heights, FS tends to decline continuously at any drawdown ratio. Furthermore, Figure 4.19 which has visualized the FS change rate shows that with a larger drawdown ratio, the FS change rate becomes larger.

Table 4. 12 Comparison of FS results and FS change rate of models in Group 9 under static load with natural slope height of 1 m to 5 m.

Groups	Subgroups	FS				
		Natural slope height (Hn) (m)				
		1	2	3	4	5
Group 9	Subgroup 37	1.28	1.24	1.23	1.22	1.17
Rate of FS change (%)		**0.00**	**-3.13**	**-3.91**	**-4.69**	**-8.59**
	Subgroup 38	1.28	1.23	1.21	1.19	1.14
Rate of FS change (%)		**0.00**	**-3.91**	**-5.47**	**-7.03**	**-10.94**
	Subgroup 39	1.27	1.22	1.21	1.18	1.12
Rate of FS change (%)		**0.00**	**-3.94**	**-4.72**	**-7.09**	**-11.81**
	Subgroup 40	1.27	1.21	1.20	1.17	1.10
Rate of FS change (%)		**0.00**	**-4.72**	**-5.51**	**-7.87**	**-13.39**
	Subgroup 41	1.28	1.21	1.19	1.16	1.10
Rate of FS change (%)		**0.00**	**-5.47**	**-7.03**	**-9.38**	**-14.06**

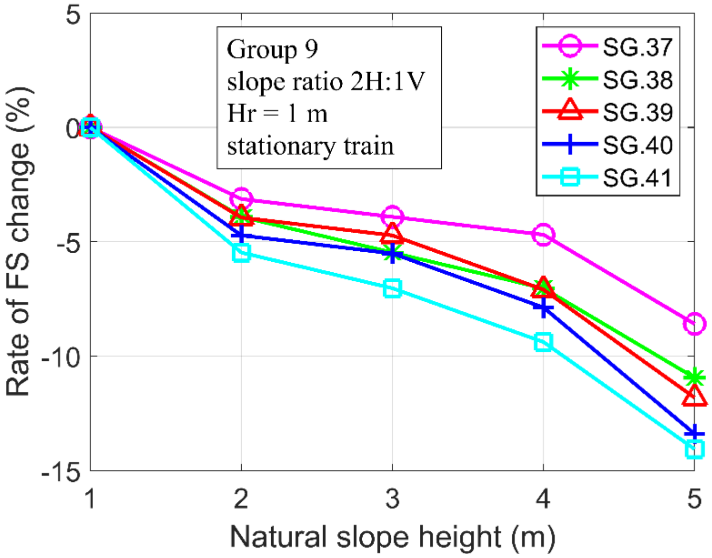

Figure 4. 19. Relationship between the FS change rate of natural slope height (1 m to 5 m) and natural slope height for models in Group 9 with a stationary train.

The FS results and FS change rate when $H_r = 2$ m are summarized in Table 4.13. Higher railway embankment primarily brings two factors, enhancing the shear strength of soil and shear stress in the structure simultaneously. The former one leads to higher FS, while the latter drags down FS. FS results with 1-m natural slope height are much higher than those in Table 4.12 ($H_r = 1$ m case). This observation is because the increase of railway embankment height helps stabilize the slope as its strength is much larger, persisting most of the slip surface in this model. But when natural slope height becomes larger (> 1m), the aforementioned analysis reveals it is harmful to slope stability. And compared to FS results in Table 4.12, FS results with 2-m railway embankment are smaller mainly because the increase of shear stress surpasses that of the shear strength. Thus, as can be seen in Figure 4.20, a sharp drop of FS when natural slope height increases from 1 m to 2 m for all drawdown ratios.

Table 4. 13 Comparison of FS results and FS change rate of models in Group 10 under static load with natural slope height of 1 m to 5 m.

Groups	Subgroups	FS				
		Natural slope height (Hn) (m)				
		1	2	3	4	5
Group 10	Subgroup 42	1.86	1.20	1.17	1.16	1.15
Rate of FS change (%)		**0.00**	**-35.48**	**-37.10**	**-37.63**	**-38.17**
	Subgroup 43	1.65	1.19	1.15	1.13	1.11
Rate of FS change (%)		**0.00**	**-27.88**	**-30.30**	**-31.52**	**-32.73**
	Subgroup 44	1.65	1.18	1.14	1.11	1.09
Rate of FS change (%)		**0.00**	**-28.48**	**-30.91**	**-32.73**	**-33.94**
	Subgroup 45	1.65	1.18	1.13	1.10	1.07
Rate of FS change (%)		**0.00**	**-28.48**	**-31.52**	**-33.33**	**-35.15**
	Subgroup 46	1.64	1.17	1.13	1.09	1.07
Rate of FS change (%)		**0.00**	**-28.66**	**-31.10**	**-33.54**	**-34.76**

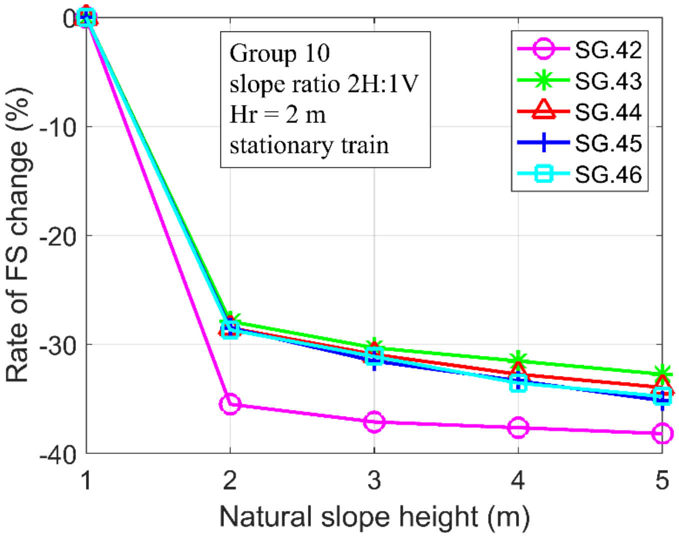

Figure 4. 20. Relationship between the FS change rate of natural slope height (1 m to 5 m) and natural slope height for models in Group 10 with a stationary train.

Table 4.14 demonstrates FS results and FS change rate when railway embankment is 3 m, versus various natural slope heights. In this case, the enhancement of shear strength due to a higher railway embankment becomes the major factor increasing slope stability compared to shorter embankments shown in the above two tables. With natural slope height augmenting, FS continuously reduces but in a quasi-linear way as presented in Figure 4.21. Based on the analysis, it is suggested that smaller natural slope heights have the priority in design.

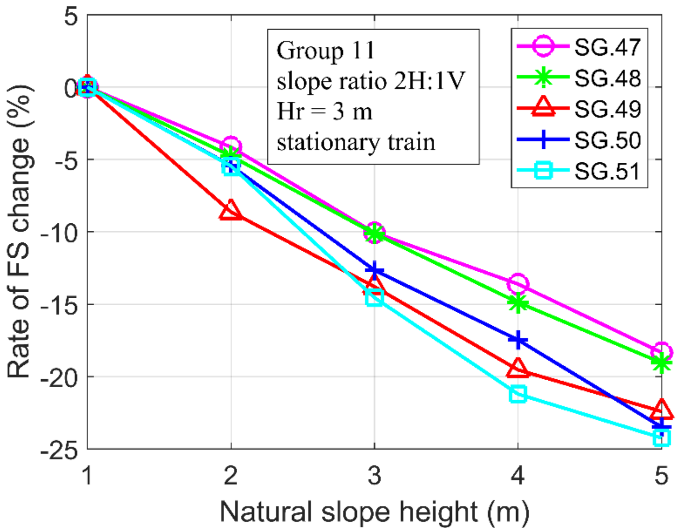

Figure 4. 21. Relationship between the FS change rate of natural slope height (1 m to 5 m) and natural slope height for models in Group 11 with a stationary train.

Table 4. 14 Comparison of FS results and FS change rate of models in Group 11 under static load with natural slope height of 1 m to 5 m.

Groups	Subgroups	FS				
		Natural slope height (Hn) (m)				
		1	2	3	4	5
Group 11	Subgroup 47	1.69	1.62	1.52	1.46	1.38
Rate of FS change (%)		**0.00**	**-4.14**	**-10.06**	**-13.61**	**-18.34**
	Subgroup 48	1.68	1.60	1.51	1.43	1.36
Rate of FS change (%)		**0.00**	**-4.76**	**-10.12**	**-14.88**	**-19.05**
	Subgroup 49	1.74	1.59	1.50	1.40	1.35
Rate of FS change (%)		**0.00**	**-8.62**	**-13.79**	**-19.54**	**-22.41**
	Subgroup 50	1.66	1.57	1.45	1.37	1.27
Rate of FS change (%)		**0.00**	**-5.42**	**-12.65**	**-17.47**	**-23.49**
	Subgroup 51	1.65	1.56	1.41	1.30	1.25
Rate of FS change (%)		**0.00**	**-5.45**	**-14.55**	**-21.21**	**-24.24**

(d) Influence of the drawdown ratio

Similar to the investigation of natural slope height, the study of drawdown ratio is classified in three batches based on different railway embankment heights. FS results at the drawdown ratios larger than 0.2 are compared to that at 0.2 (first row of FS results). Table 4.15 lists FS results and FS change rate when railway embankment height is 1 m at various drawdown ratios. It is clear that with the drawdown ratio becoming larger, FS decreases continuously with any natural slope height. Beyond this observation, Figure 4.22 further shows that a larger drawdown ratio enlarges the reduction of FS change as a function of natural slope heights.

Table 4. 15 Comparison of FS results and FS change rate of models in Group 9 under static load with the drawdown ratio of 0.2 to 1.0.

Groups	Subgroups	FS				
		Natural slope height (Hn) (m)				
		1	2	3	4	5
Group 9	Subgroup 37	1.28	1.24	1.23	1.22	1.17
	Subgroup 38	1.28	1.23	1.21	1.19	1.14
Rate of FS change (%)		**0.00**	**-0.81**	**-1.63**	**-2.46**	**-2.56**
	Subgroup 39	1.27	1.22	1.21	1.18	1.12
Rate of FS change (%)		**-0.78**	**-1.61**	**-1.63**	**-3.28**	**-4.27**
	Subgroup 40	1.27	1.21	1.20	1.17	1.10
Rate of FS change (%)		**-0.78**	**-2.42**	**-2.44**	**-4.10**	**-5.98**
	Subgroup 41	1.28	1.21	1.19	1.16	1.10
Rate of FS change (%)		**0.00**	**-2.42**	**-3.25**	**-4.92**	**-5.98**

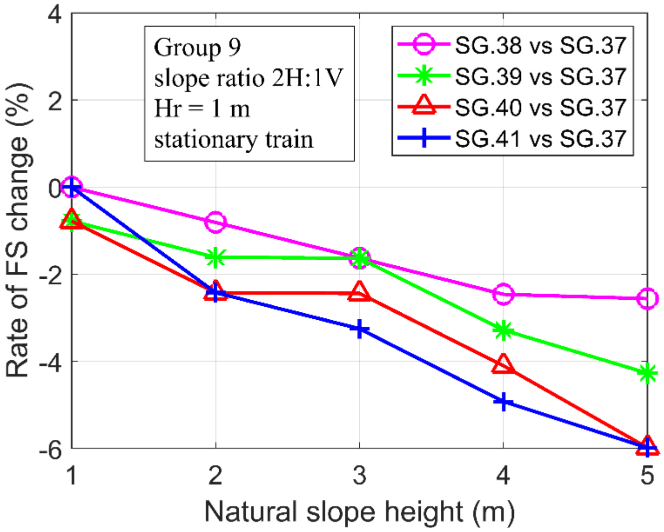

Figure 4. 22. Relationship between the FS change rate of drawdown ratios (0.2 to 1.0) versus the natural slope height for models in Group 9 with a stationary train.

When railway embankment height increases to 2 m, a similar trend of FS change compared to the above case can be observed when natural slope height is larger than 1 m in Table 4.16 and Figure 4.23. FS change rate increases in a quasi-linear way against the natural slope height. However, when natural slope height is 1 m, 2-m embankment is prominent to stabilize the slope, resulting in higher FS values. When the drawdown ratio continuously increases by 0.2, FS change stays almost the same (around 11.5 %) with the 1-m natural slope in Table 4.16.

Table 4. 16 Comparison of FS results and FS change rate of models in Group 10 under static load with the drawdown ratio of 0.2 to 1.0.

Groups	Subgroups	FS				
		Natural slope height (Hn) (m)				
		1	2	3	4	5
Group 10	Subgroup 42	1.86	1.20	1.17	1.16	1.15
	Subgroup 43	1.65	1.19	1.15	1.13	1.11
Rate of FS change (%)		**-11.29**	**-0.83**	**-1.71**	**-2.59**	**-3.48**
	Subgroup 44	1.65	1.18	1.14	1.11	1.09
Rate of FS change (%)		**-11.29**	**-1.67**	**-2.56**	**-4.31**	**-5.22**
	Subgroup 45	1.65	1.18	1.13	1.10	1.07
Rate of FS change (%)		**-11.29**	**-1.67**	**-3.42**	**-5.17**	**-6.96**
	Subgroup 46	1.64	1.17	1.13	1.09	1.07
Rate of FS change (%)		**-11.83**	**-2.50**	**-3.42**	**-6.03**	**-6.96**

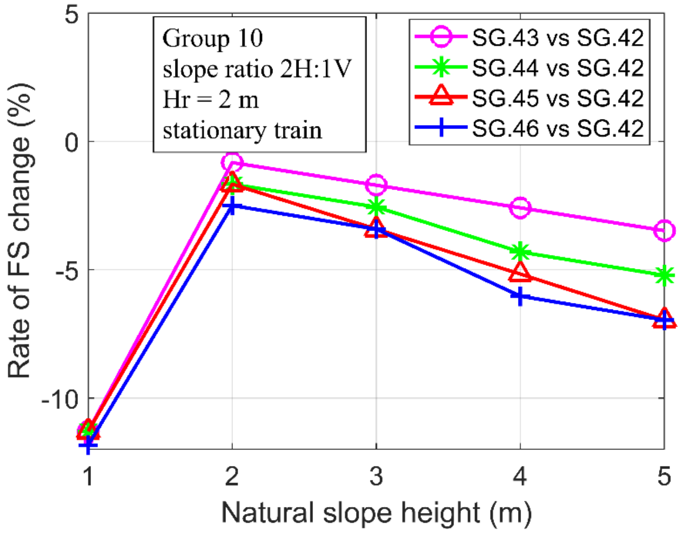

Figure 4. 23. Relationship between the FS change rate of drawdown ratios (0.2 to 1.0) versus the natural slope height for models in Group 10 with a stationary train.

For the model with 3-m railway embankment, all results are summarized in Table 4.17 and Figure 4.24. Except for the positive value (Rate of FS change = 2.96 %) which is believed to be an anomaly, FS change shares similar tendency compared to the first batch (H_r= 1 m). but the FS change due to variations of drawdown ratios with same natural slope heights becomes larger compared to the first batch.

Table 4. 17 Comparison of FS results and FS change rate of models in Group 11 under static load with the drawdown ratio of 0.2 to 1.0.

Groups	Subgroups	FS Natural slope height (Hn) (m) 1	 2	 3	 4	 5
Group 11	Subgroup 47	1.69	1.62	1.52	1.46	1.38
	Subgroup 48	1.68	1.60	1.51	1.43	1.36
Rate of FS change (%)		**-0.59**	**-1.23**	**-0.66**	**-2.05**	**-1.45**
	Subgroup 49	1.74	1.59	1.50	1.40	1.35
Rate of FS change (%)		**2.96**	**-1.85**	**-1.32**	**-4.11**	**-2.17**
	Subgroup 50	1.66	1.57	1.45	1.37	1.27
Rate of FS change (%)		**-1.78**	**-3.09**	**-4.61**	**-6.16**	**-7.97**
	Subgroup 51	1.65	1.56	1.41	1.30	1.25
Rate of FS change (%)		**-2.37**	**-3.70**	**-7.24**	**-10.96**	**-9.42**

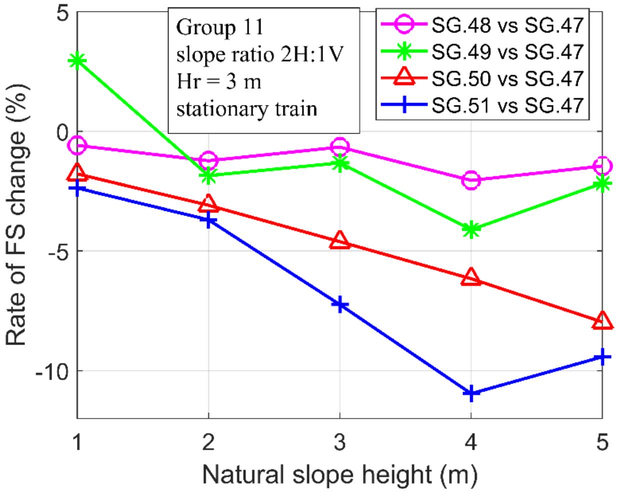

Figure 4. 24. Relationship between the FS change rate of drawdown ratios (0.2 to 1.0) versus the natural slope height for models in Group 11 with a stationary train.

(e) Influence of the train speed

In this section, a moving train on the track is considered with the model of H_r = 1 m and 3H:1V slope ratio. The range of the moving train speed is from 0 mph to 20 mph with a step of 5 mph. FS results are demonstrated in Table 4.18. With the train moving faster, FS reduces in all subgroups.

Figure 4.25 has visualized the FS results in Table 4.18 and it is clear to identify FS change rate versus natural slope height and train speed. To compare results in different graphs, the color bar for each one has been kept the same with a min of 1.19 and a max of 1.32. It is noticeable that large FS results are obtained with smaller natural slope heights and low train speeds for each graph.

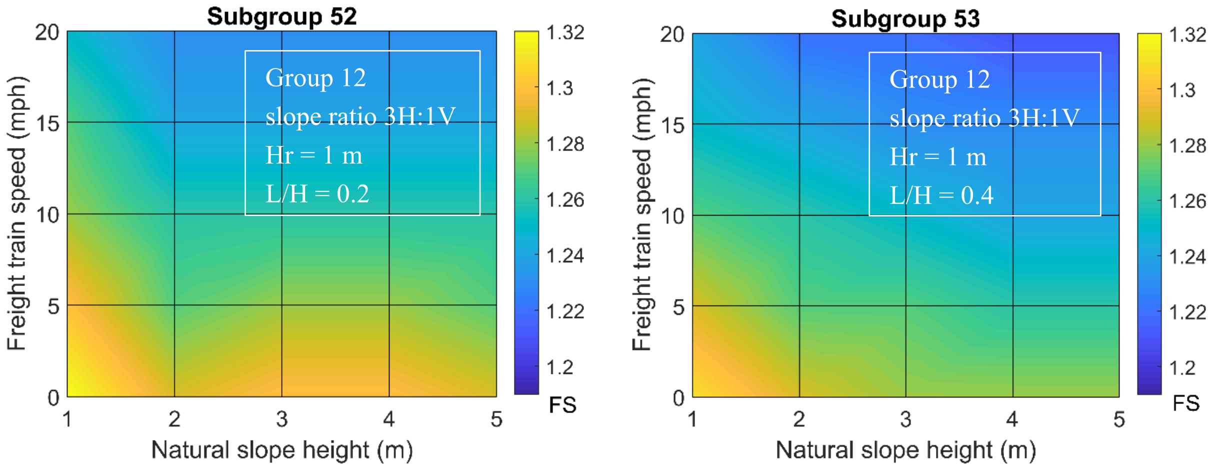

(a)

(b)

Figure 4. 25. Pseudocolor graphs of FS results for each subgroup in Table 4.18. (a) slope ratio 0.2; (b) 0.4; The color bar has a color data min of 1.19 and a max of 1.32 for each graph.

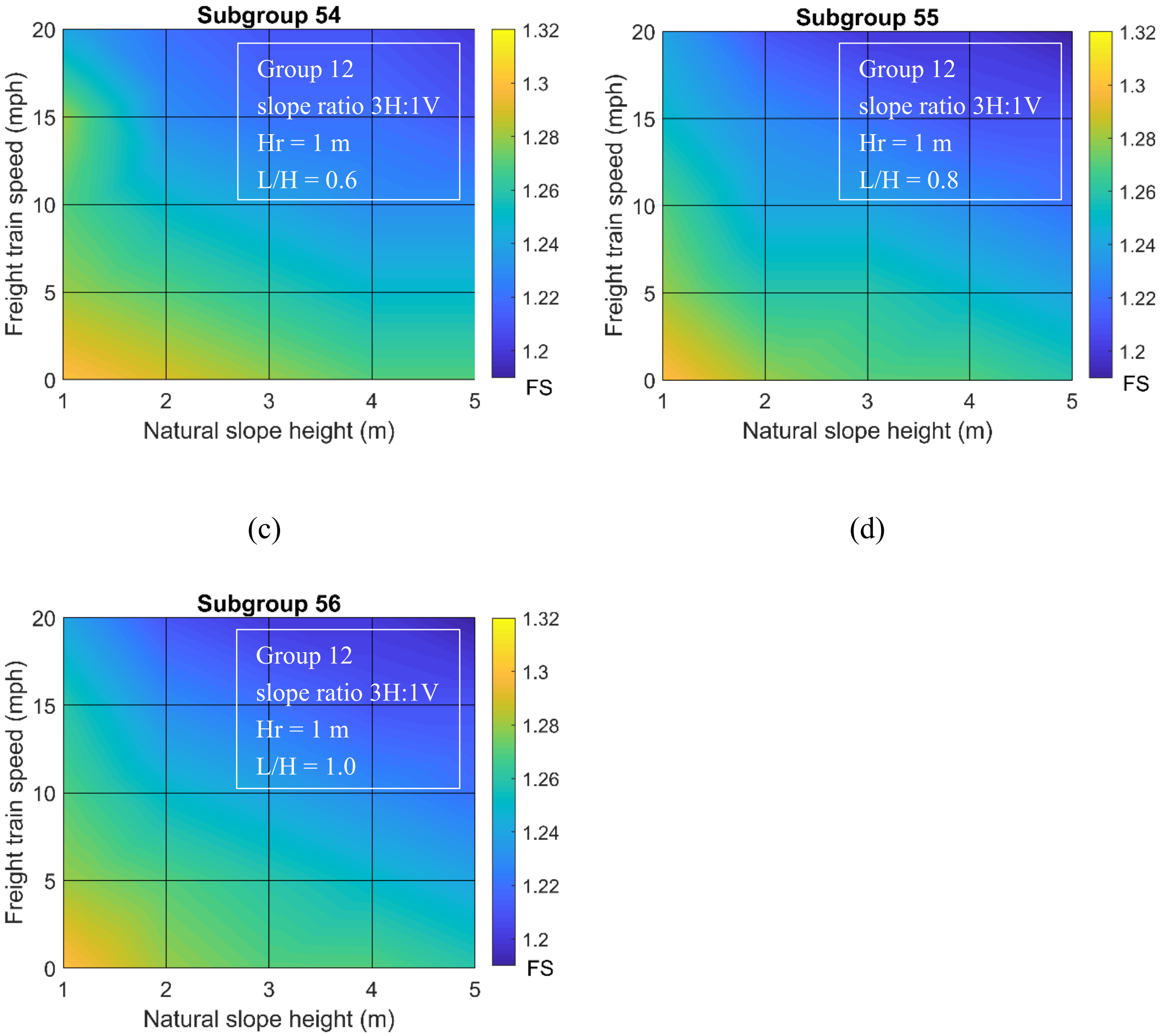

(c)

(d)

(e)

Figure 4. 25. Pseudocolor graphs of FS results for each subgroup in Table 4.18. (c) slope ratio 0.6; (d) 0.8; and (e) 1.0. The color bar has a color data min of 1.19 and a max of 1.32 for each graph. (continued).

Table 4. 18 Corresponding FS results of models in Group 12 under various train speed with the drawdown ratio of 0.2 to 1.0.

Groups	Subgroups	Train speed (mph)	FS				
			Natural slope height (H_n) (m)				
			1	2	3	4	5
Group 12	Subgroup 52	0	1.32	1.29	1.30	1.30	1.29
		5	1.30	1.27	1.28	1.28	1.27
		10	1.28	1.26	1.26	1.26	1.26
		15	1.27	1.24	1.24	1.24	1.24
		20	1.25	1.23	1.23	1.23	1.23
	Subgroup 53	0	1.31	1.29	1.28	1.28	1.28
		5	1.29	1.27	1.27	1.26	1.26
		10	1.27	1.26	1.25	1.24	1.24
		15	1.25	1.24	1.23	1.23	1.23
		20	1.24	1.22	1.22	1.21	1.21
	Subgroup 54	0	1.30	1.29	1.28	1.27	1.27
		5	1.28	1.27	1.26	1.25	1.25
		10	1.27	1.25	1.24	1.23	1.23
		15	1.28	1.23	1.22	1.22	1.21
		20	1.24	1.22	1.21	1.21	1.20
	Subgroup 55	0	1.30	1.28	1.27	1.27	1.26
		5	1.28	1.26	1.26	1.25	1.24
		10	1.27	1.24	1.24	1.23	1.22
		15	1.25	1.23	1.22	1.21	1.21
		20	1.24	1.21	1.20	1.20	1.19
	Subgroup 56	0	1.30	1.28	1.27	1.27	1.26
		5	1.28	1.27	1.26	1.25	1.24
		10	1.27	1.25	1.24	1.23	1.22
		15	1.26	1.23	1.22	1.21	1.21
		20	1.24	1.21	1.20	1.20	1.19

4.3.2 General Tendency Under the Rapid Drawdown and Stationary Train Load Conditions

Figure 4.26 has shown graphs to investigate the FS results of models in Set I, II and III vertically. The slope ratio is fixed as 2H: 1V and drawdown ratio of models in Set II and III is selected as 1.0. A stationary train with a static load (ABP = 236.24kN/m^2) is considered in Set III. The FS change rates between models in different Sets are shown against the right y-axis. Models in Set I with no phreatic surface and no train load is defined as Scenario 1 in the plot. When rapid drawdown of the water level is included in Scenario 1, it evolves to Scenario 2. While Scenario 3 considers both rapid drawdown and train load conditions. The development of models from Scenario 1 to 3 has been expressed with clear logic.

All three graphs show that FS has decreased by at least 20 % if rapid drawdown occurs with a ratio of 1.0 on the dry slope (Scenario 1). Furthermore, on top of Scenario 2, if a static train is on the track, the slope safety is degraded dramatically, with an FS reduction of at least 45 %. FS change rate tends to increase with a larger H_r for the case of Scenario 2 versus Scenario 1. However, when H_r=1m, FS reduction, due to adding the static load, is the greatest.

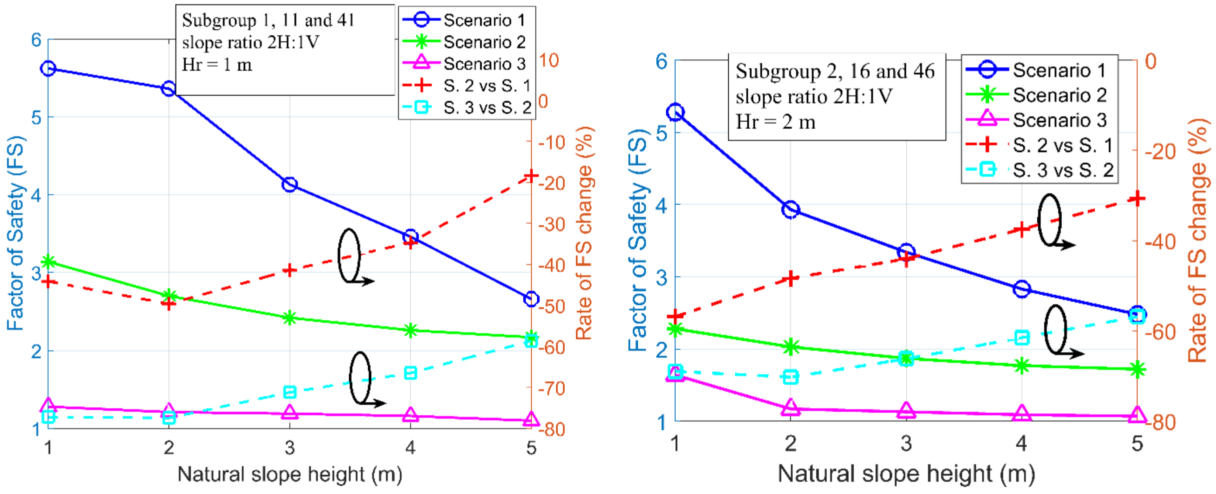

(a) (b)

Figure 4. 26. Relationships between the FS or FS change rate under different scenarios versus the natural slope height for models in (a) Subgroup 1, 11, and 41, (b) Subgroup 2, 16, and 46.

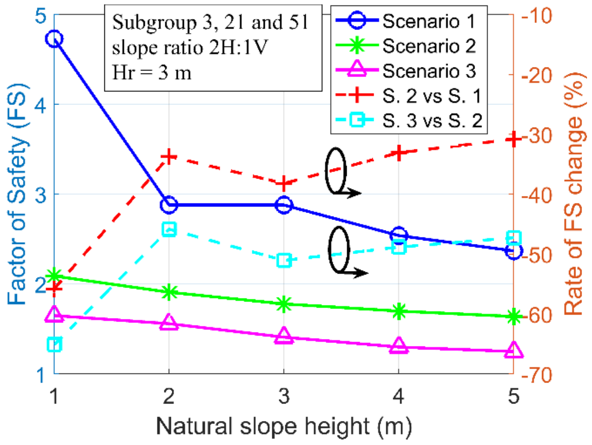

(c)

Figure 4. 26. Relationships between the FS or FS change rate under different scenarios versus the natural slope height for models in (c) Subgroup 3, 21, and 51, (continued).

4.3.3 Recommendation of Maximum Safe Train Speed Based on the Study

Figure 4.27 has visualized maximum safe train speeds for all possible situations listed in Table 4.7. Note that if the color indicates negative speed (–5 mph), it means this model cannot support a stationary train on the track let alone a moving train with any speed. The threshold of FS value was selected as 1.3, as discussed in Section 2.4.6. As can be seen in Figure 4.27 (a), when 2H:1V and H_r=1 m, the models are not safe to support any external loads. By contrast, in the previous case, if the slope ratio is built to be 3H:1V, this model can support a train in some specific conditions as shown in Figure 4.27 (d). When drawdown ratio is only 0.2 at a low level, a slow-moving train can go through safely at a speed of 5 mph if the natural slope height is 1 m. The train has to stop on the track if there are higher drawdown ratios in this case. Whereas, for Figure 4.27 (b) with 2H:1V and H_r=2 m, 1-m natural slope model can support a train moving at a low speed (only 5 mph). The slope cannot support any freight train loads including a stationary train on the track if the natural slope is higher than 1 meter. By contrast, when slope ratio increases to 3H:1V and other conditions are still the same (H_r=2 m, 1-m natural slope), the slope then becomes stable enough to support a freight train running at a moderate speed. The maximum speed can reach 25 mph in this case as shown in Figure 4.27 (e).

Clearly shown in Figure 4.27 (c) and (f), models with H_r=3 m are the best choices. For the case with the slope ratio of 2H:1V (Figure 4.27 (c)), the maximum safe train speed can reach 25 mph with 1-m natural slope. With a larger natural slope height, the train has to slow down. And if the model has 5 m natural slope and at the same time, the drawdown ratio is larger than 0.6, this model becomes unstable on which any external loads are not allowed, even a stationary train. Whereas, when the slope ratio is 3H:1V, the maximum speed reaches 75 mph which is the upper bond speed in our analysis. And this slope can support this maximum speed of 75 mph for all rapid drawdown ratios as shown in Figure (f).

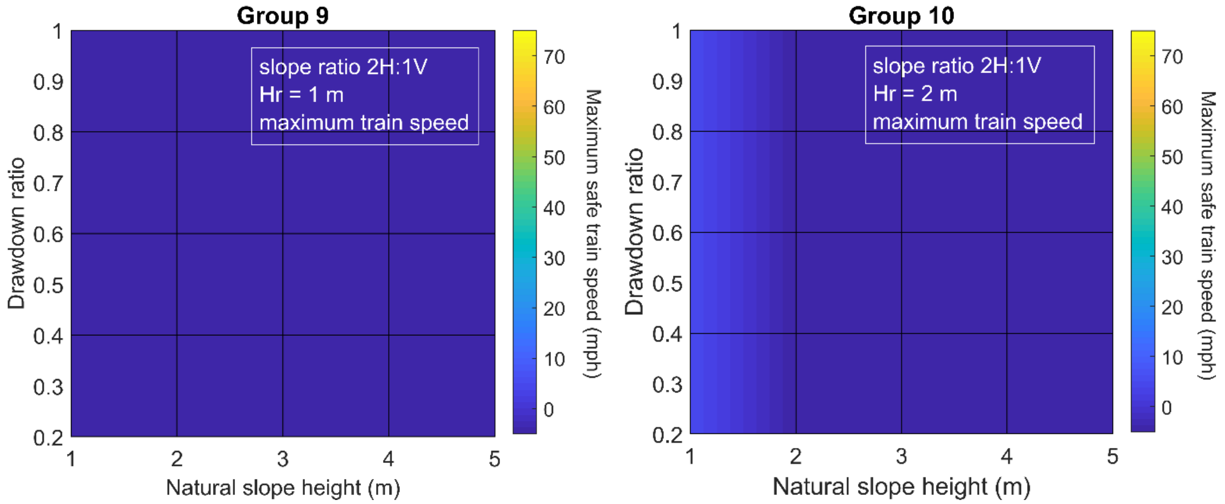

(a)

(b)

Figure 4. 27. Pseudocolor graphs of maximum safe train speed for cases listed in Table 4.7. (a) 2H:1V, H_r=1 m, (b) 2H:1V, H_r=2 m. Note that negative speed in the plotting is defined as the model cannot support a stationary train or any moving train.

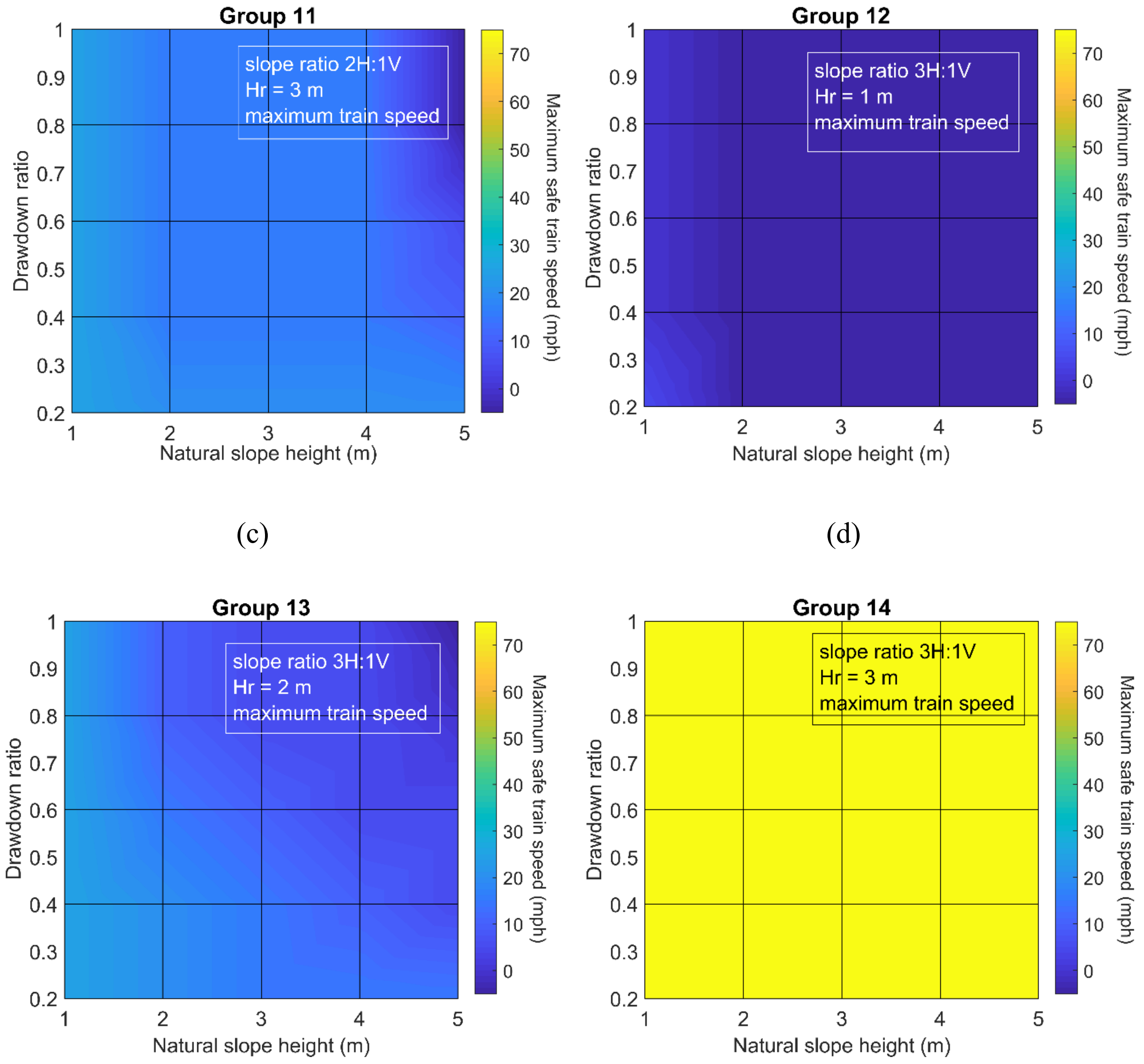

(c) (d)

(e) (f)

Figure 4. 27. Pseudocolor graphs of maximum safe train speed for cases listed in Table 4.7. (c) 2H:1V, H_r=3 m, (d) 3H:1V, H_r=1 m, (e) 3H:1V, H_r=2 m, and (f) 3H:1V, H_r=3 m. Note that negative speed in the plotting is defined as the model cannot support a stationary train or any moving train. (continued).

Thus, regarding the slope construction from the standpoint of larger maximum safe train speed, the combination of the 1-m natural slope, 3H:1V and H_r=3 m is a good choice. According to the preceding analysis, it can support the freight train running at a speed of 75 mph even with a rapid drawdown condition. With this study, a convenient mapping relationship can be established between maximum safe train speeds and slope and railway embankment geometries.

4.4 Summary

This chapter first established three sets of models, which are dry slope, slope under rapid drawdown condition but no train load, slope under both rapid drawdown and train load conditions simultaneously. The above three sets of models show how models develop from the simple to the complicated, revealing the major logic line of this research. Analysis of the first two sets of models set a foundation for the study of the set that is subjected to both rapid drawdown and a moving freight train. For all sets of models, each structural parameter is investigated in detail using the control variable method. As a special case, the model with the stationary train rests on the track is studied first in Set III. Then, maximum safe train speeds for different models are demonstrated with discussions.

Based on the parametric study, smaller natural slope heights help stabilize the slope under rapid drawdown condition. A larger slope ratio, in this study 3H:1V, is recommended in terms of obtaining higher slope stability. Also, 3-m railway embankment is strongly recommended over 1-m or 2-m counterparts. The calculation of maximum safe train speed reveals that 3H:1V slope ratio is better than 2H:1V based on Figure 4.27.

In conclusion, the geometric choices of 1-m natural slope height, 3H:1V slope ratio, and 3-m railway embankment are strongly recommended to ensure larger FS values, in other words, higher maximum safe train speeds. Also, results show that any rapid drawdown condition has a negligible influence on the maximum safe train speeds if these geometrical parameters of the slope are selected. Given the geometrical parameters of the slope and railway embankment as well as the information of rapid drawdown ratios, the maximum safe train speeds can be quickly identified with the help of this study.

Chapter 5 Conclusions and Future Work

5.0 Introduction

This chapter summarizes the major work and contributions of this work and possible future directions as related to the project, which is divided into four sections. Section 5.1 reviews the project objective and methodology to achieve the goal. The conclusions are addressed in Section 5.2 after the analysis and discussion of the simulation results. Section 5.3 presents the limitations of this study. Finally, recommendations for future work are discussed in Section 5.4.

5.1 Thesis Summary

The primary objective of this study was to provide a guideline to identify the maximum safe train speed with respect to a clay slope under rapid drawdown conditions. To quantify the effect of major parameters on the stability of a slope, the control variable method was applied to the parametric analysis. Several methodological steps were established to fulfill the primary objective. As introduced in Chapter 1, the methodological steps consisted of:

(a) modeling of the situation and identification of key variables that control model behavior, especially slope stability;
(b) verification of finite element method based RS2 to be able to handle the requirements imposed by the models;
(c) development of numerical models based on the literature review;
(d) parametric study of numerical models, including the factor of safety and maximum safe train speed of the slope under these conditions.

Chapter 2 established a review of literature of numerical methods in geomechanics, rapid drawdown analysis in slopes, moving train loads analysis on the railway embankment, and the typical values of key parameters identified in the analyzed model. Chapter 3 presents verification of RS2 which could offer reliable simulation results compared to those from a published work and the establishment of three sets of numerical models (Set I, II, and III). Finally, Chapter 4 compares simulation results for the models in Set I, II, and III. Parametric study of models in detail and a summary of maximum safe train speeds according to results of slope safety factors are also presented in this chapter. This work successfully developed a model to evaluate the effect of rapid drawdown on an unsubmerged railway embankment under moving freight train loads. Most importantly, a relationship between the maximum safe train speed and a clay slope given geometrical parameters with rapid drawdown occurring has been established.

5.2 Conclusion

The focus of this thesis was to perform a set of parametric studies to understand slope stability and further identify maximum safe train speeds for given slope geometries and rapid drawdown conditions. During the parametric study, to stabilize the slope under rapid drawdown and a moving freight train conditions, several dimensional parameters should be carefully considered:

(a) smaller natural slope heights; In the study, 1-m natural slope height demonstrates a higher slope factor of safety and allows a higher maximum safe train speed.

(b) larger slope ratio; 3H:1V slope ratio is theoretically proved an effective way to enhance slope stability.

(c) optimum railway embankment height; In the study, a railway embankment height of 3 m helps increase both factor of safety and maximum safe train speed, compared to 1 m and 2 m counterparts. It also indicates an optimum railway embankment may exist for each model.

5.3 Limitations

Although many relevant parameters were considered in the study, some were not included, such as:

(a) Models do not consider curves of on the track or any potential change of soil layering along the track.

(b) Temperature and wind factors often have an influence on the track and soil behavior. However, they were not considered in the study.

(c) Calculation of moving train loads is simplified. For example, the track is assumed to level, smooth, and even. The contact between train wheels and the track was assumed to be ideal.

(d) The conclusion addressed in this work only applies to the properties of the clay discussed in Chapter 3.

5.4 Future Work

Regarding this study, certain further improvements can be done, including but not limited to:

(a) A determination of the duration of impact for the stability of a slope after the occurrence of rapid drawdown should be studied.

(b) A 3-dimensional model is strongly recommended. Only in this way can we take practical track situation into accounts, such as a curved track and an uneven track.

(c) More environmental factors should be introduced in the simulation. For example, consideration of temperature is essential, as soil behaves quite differently in hot summer and cold winter seasons in Canada.

(d) Calculation of moving freight train loads need to be optimized. With the aid of dynamic simulation capabilities of other software, it is possible to obtain actual loading force on the track at each point in time. This can help to mimic a more realistic situation.

References

1. Abramson, L. W., Lee, T. S., Sharma, S., and Boyce, G. M. (2002). *Slope Stability and Stabilization Methods*, 2nd Ed., John Wiley & Sons, New York.
2. Akin, J. E. (2005). *Finite element analysis with error estimators: an introduction to the FEM and adaptive error analysis for engineering students*, Butterworth-Heinemann, Burlington, MA.
3. American Railway Engineering and Maintenance-of-Way Association (AREMA) (2010). *AREMA manual for railway engineering*, Landover, MD.
4. American Railway Engineering and Maintenance-of-Way Association (AREMA) (2013). *AREMA manual for railway engineering*, Landover, MD.
5. Banerjee, P. K., and Wilson, B. (2005). *Developments in boundary element methods: industrial applications*, CRC Press, London.
6. Bear, J. (2012). *Hydraulics of groundwater*, Courier Corporation, New York.
7. Bertram, A., and Gluge, R. (2013). *Solid mechanics: theory, modeling, and problems.* Springer International Publishing, Switzerland.
8. Bobet, A. (2010). "Numerical methods in geomechanics." *Arab. J. Sci. Eng.*, 35(1B), 27-48.
9. Budhu, M. (2008). *Soil mechanics and foudations,* John Wiley & Sons, Hoboken, NJ.
10. Calamak, M., and Yanmaz, A. (2016). "Seepage characteristics in embankments subject to variable water storages on both sides." *Proc., 4th IAHR Europe Congress,* International Association for Hydro-Environment Engineering and Research, Liege, Belgium, 551-556.
11. Chang, S., and Zhang, S. (2006). *Geological engineering manual,* 4th Ed., China Contruction and Industry Press, Bejing, China.
12. Chen, W.-F., and Mizuno, E. (1990). *Nonlinear analysis in soil mechanics*, Elsevier, Amsterdam, Netherlands.
13. Cheng, Y., Lansivaara, T., and Wei, W. (2007). "Two-dimensional slope stability analysis by limit equilibrium and strength reduction methods." *Comput. Geotech.*, 34(3), 137-150.
14. Cheng, Y., and Lau, C. (2014). *Slope stability analysis and stabilization: new methods and insight*, CRC Press, London.
15. Clough, R. W. (1960). "The finite element method in plane stress analysis." *Proc., 2nd Conf. on Electronic Computation,* ASCE, Pittsburgh, PA, 345-378.

16. Cook, R. D. (2007). *Concepts and applications of finite element analysis*, John Wiley & Sons, Hoboken, NJ.
17. Costabel, M. (1987). "Principles of boundary element methods." *Comput. Phys. Rep.*, 6(1-6), 243-274.
18. Cundall, P. A., and Hart, R. D. (1992). "Numerical modelling of discontinua." *Eng. Computation.*, 9(2), 101-113.
19. Dawson, E., Roth, W., and Drescher, A. (1999). "Slope stability analysis by strength reduction." *Geotechnique*, 49(6), 835-840.
20. Desai, C. S., and Christian, J. T. (1979). *Numerical methods in geotechnical engineering*, McGraw-Hill, New York.
21. Dick, S. (2016). "Legacy train configurations for fatigue life evaluation of steel railway bridges." *Proc., 2016 AREMA Annu. Conf.,* American Railway Engineering and Maintenance-of-Way Association, Orlando, FL, 1357-1378.
22. Donald, I., and Giam, S. (1988) "Application of the nodal displacement method to slope stability analysis." *Proc., 5th Australia-New Zealand Conf. on Geomechanics,* Australian Geomechanics Society, Sydney, Australia, 22-23.
23. Duncan, J. M. (1996). "State of the art: limit equilibrium and finite-element analysis of slopes." *J. Geotech. Eng.*, 122(7), 577-596.
24. Duncan, J. M., and Dunlop, P. (1969). "Slopes in stiff-fissured clays and shales." *J. Soil Mech. Foud. Div.,* 95(2), 467-492.
25. Duncan, J. M., Wright, S. G., and Brandon, T. L. (2014). *Soil strength and slope stability*, John Wiley & Sons, Hoboken, NJ.
26. Dunlavy, J., Akuoko-Asibey, A., Masse, R., and Pilon, D. (2005). "An analysis of the transportation industry in 2005." *Statistics Canada*, Catalogue No. 11-621-MIE-NO. 044, 2005.
27. Egeli, I., and Usun, H. (2012). "Designing high-speed train railway embankments using finite element analysis." *Arab. J. Sci. Eng.*, 37, 2127-2126.
28. Esveld, C. (2001). *Modern railway track*, MRT-productions, Zaltbommel, Netherlands.
29. Farias, M., and Naylor, D. (1998). "Safety analysis using finite elements." *Comput. Geotech.*, 22(2), 165-181.

30. Fellenius, W. (1922). Statens jarnvagars geotekniska kommission: slutbetankande. *Tech. Rep.*, Stockholm, Sweden. (in Swedish)
31. Fellenius, W. (1927). Erdstatish berechnungen mit reibung und kohäsion. W. Ernst & Sohn, Berlin, Germany. (in German)
32. Fredlund, M., Lu, H., and Feng, T. (2011). "Combined seepage and slope stability analysis of rapid drawdown scenarios for levee design." *Proc., GeoFrontiers 2011,* ASCE, Reston, VA, 1595-1604.
33. Frost, M. W., Fleming, P. R., and Rogers, C. D. (2004). "Cyclic triaxial tests on clay subgrades for analytical pavement design." *J. Transp. Eng.*, 130(3), 378-386.
34. Griffiths, D. V. (1994). “Coupled analyses in geomechanics.” *Visco-plastic behaviour of geomaterials*, N. D. Cristescu and G. Gioda, eds., Chap. 5, Springer, New York.
35. Griffiths, D. V., and Lane, P. (1999). "Slope stability analysis by finite elements." *Geotechnique*, 49(3), 387-403.
36. Hall, W. S. (1994). *Boundary element method*, Springer Science & Business Media, Dordrecht, Netherlands.
37. Hammah, R. E., Yacoub, T. E., Corkum, B., and Curran, J. H. (2005a). "A comparison of finite element slope stability analysis with conventional limit-equilibrium investigation." *Proc., 58th Canadian Geotechnical and 6th Joint IAH-CNC and CGS Groundwater Specialty Conf.*, Saskatoon, Saskatchewan, Canada.
38. Hammah, R. E., Yacoub, T. E., Corkum, B., and Curran, J. H. (2005b). "The shear strength reduction method for the generalized Hoek-Brown criterion." *Proc., 40th U.S. Symp. on Rock Mechanics: Rock Mechanics for Energy, Mineral and Infrastructure Development in the Northern Regions,* Vol. 1, Curran Associates, Red Hook, NY, 234-239.
39. Hammah, R. E., Yacoub, T. E., Corkum, B., and Curran, J. H. (2007a). "Analysis of blocky rock slopes with finite element shear strength reduction analysis." *Proc., 1st Canada-U.S. Rock Mechanics Symp.*, Taylor & Francis Group, London, 329-334.
40. Hammah, R. E., Yacoub, T. E., and Curran, J. H. (2007b) "Serviceability-based slope factor of safety using the shear strength reduction (SSR) method." *Proc., 11th ISRM Cong.,* International Society for Rock Mechanics, Lisbon, Portugal, 1137-1140.
41. Herrmann, H. (1997). "Intermittency and self-similarity in granular media." *Powders & Grains 97*, Balkema, Rotterdam, 317-320.

42. Hinrichsen, H., and Wolf, D. E. (2006). *The physics of granular media*, John Wiley & Sons, Hoboken, NJ.
43. Hoek, E. (2007). “Practical rock engineering.” <http://www.rocscience .com/hoek/corner/Practical_Rock_Engineering.pdf> (Apr. 4, 2012).
44. Hopkins, T. C., Allen, D. L., and Deen, R. C. (1975). “Effect of water on slope stability.” *Res. Rep. 435*, Div. of Research, Kentucky Dept. of Transportation, Frankfort, KY.
45. Huang, M., and Jia, C.-Q. (2009). "Strength reduction FEM in stability analysis of soil slopes subjected to transient unsaturated seepage." *Comput. Geotech.*, 36(1-2), 93-101.
46. Indraratna, B., Salim, W., and Rujikiatkamjorn, C. (2011). *Advanced rail geotechnology–ballasted track*, CRC press, London.
47. Jiang, H., Bian, X., Cheng, C., Chen, Y., and Chen, R. (2016). "Simulating train moving loads in physical model testing of railway infrastructure and its numerical calibration." *Acta Geotech.*, 11(2), 231-242.
48. Johansson, A. (2006). "Out-of-round railway wheels—assessment of wheel tread irregularities in train traffic." *J. Sound Vib.*, 293(3), 795-806.
49. Kainthola, A., Verma, D., Thareja, R., and Singh, T. (2013). "A review on numerical slope stability analysis." *Int. J. Sci. Eng. Technol. Res.*, 2(6), pp: 1315-1320.
50. Lam, L., Fredlund, D., and Barbour, S. (1987). "Transient seepage model for saturated–unsaturated soil systems: a geotechnical engineering approach." *Can. Geotech. Journal*, 24(4), 565-580.
51. Lekarp, F., and Dawson, A. (1998). "Modelling permanent deformation behaviour of unbound granular materials." *Constr. Build. Mater.*, 12(1), 9-18.
52. Leonard, T. (1971). "Train wheel defect detector." The United States of America.
53. Li, D., Hyslip, J., Sussmann, T., and Chrismer, S. (2002). *Railway geotechnics*, CRC Press, London.
54. Li, G., and Desai, C. (1983). "Stress and seepage analysis of earth dams." *J. Geotech. Eng.*, 109(7), 946-960.
55. Luding, S. (2008). "Introduction to discrete element methods: basic of contact force models and how to perform the micro-macro transition to continuum theory." *Eur. J. Environ. Civ. Eng.*, 12(7-8), 785-826.

56. Matsui, T. (1988) "Finite element stability analysis method for reinforced slope cutting." *Proc., Int. Geotechnical Symp. on Theory and Practice of Earth Reinforcement,* Fukuoka, Japan, 317-322.
57. Matsui, T., and San, K.-C. (1992). "Finite element slope stability analysis by shear strength reduction technique." *Soils Found.*, 32(1), 59-70.
58. Matthews, C., Farook, Z., and Helm, P. (2014). "Slope stability analysis–limit equilibrium or the finite element method." *Ground Eng.*, 162, 22-28.
59. Munjiza, A. (2004). *The combined finite-discrete element method*, John Wiley & Sons, London.
60. Naylor, D. J. (1982). "Finite elements and slope stability." *Numerical methods in geomechanics*, J. B. Martins, ed., Springer, New York, 229–244.
61. Nikolić, M., Roje-Bonacci, T., and Ibrahimbegović, A. (2016). "Overview of the numerical methods for the modelling of rock mechanics problems." *Tehnički vjesnik*, 23(2), 627-637.
62. Peck, R. B., Hanson, W. E., and Thornburn, T. H. (1974). *Foundation engineering*, Wiley, New York.
63. Pietruszczak, S. (2010). *Fundamentals of plasticity in geomechanics*, CRC Press, Boca Raton, FL.
64. Pinyol, N. M., Alonso, E. E., and Olivella, S. (2008). "Rapid drawdown in slopes and embankments." *Water Resour. Res.*, 44(5).
65. Profillidis, V. A. (2014). *Railway management and engineering*, Ashgate Publishing Company, Burlington, VT.
66. Punmia, B. C., Jain, Ashok K., and Jain Arun K. (2005). *Soil mechanics and foundations*, Laxmi Publications, New Delhi, India.
67. Railway Association of Canada (RAC) (2017). "Rail trends 2017." , Ottawa, Ontario, Canada.
68. Rocscience Inc. (2019) RS2 Excavation & Design support software. Specification sheet.
69. Rocscience Inc. "Convergence Criteria." (2018a). <https://www.rocscience.com/help/rs2/pdf_files/theory/Convergence_Criteria.pdf>.
70. Rocscience Inc. "Coupled Drawdown Analysis." (2018b). <https://www.rocscience.com/help/rs2/index.htm#t=tutorials%2FRS2__Coupled_Drawdown_Analysis.htm>.

71. Rowe, R. K. (2012). *Geotechnical and geoenvironmental engineering handbook*, Springer Science & Business Media, Berlin, Germany.
72. Selig, E. T., and Waters, J. M. (1994). *Track technology and substructure management*, Thomas Telford, London.
73. Sherard, J. L., Woodward, R. J., Gizienski, S. G., and Clevenger, W. A. (1963). *Earth and earth-rock dams*, Wiley, New York.
74. Smith, I. M., Griffiths, D. V., and Margetts, L. (2013). *Programming the finite element method*, John Wiley & Sons, Chichester, UK.
75. Snitbhan, N., and Chen, W.-F. (1976). "Elastic-plastic large deformation analysis of soil slopes." *Comp. Struct.*, 9(6), 567-577.
76. Song, E. (1997). "Finite element analysis of safety factor for soil structures." *Chi. J. Geotech. Eng.*, 19(2), 1-7. (in Chinese)
77. Suiker, A. S., Selig, E. T., and Frenkel, R. (2005). "Static and cyclic triaxial testing of ballast and subballast." *J. Geotech. Geoenviron. Eng.*, 131(6), 771-782.
78. Terzaghi, K. (1951). *Theoretical soil mechanics*, Chapman And Hall, London.
79. Timoshenko, S. P., and Goodier, J. N. (1982). *Theory of elasticity*. 3rd ed. McGraw-Hill, New York.
80. Transport Canada (2006). "Transportation in Canada 2006.", Ottawa, Ontario, Canada.
81. Transport Canada (2017). "Transportation in Canada 2017.", Ottawa, Ontario, Canada.
82. Transportation Safety Board (TSB) (1992). "Railway Occurrence Report", *Rep. No. R92T0183*, Nakina, Ontario, Canada.
83. Transportation Safety Board (TSB) (1997). "Railway Occurrence Report", *Rep. No. R97D0113*, Coteau-du-Lac, Quebec, Canada.
84. Transportation Safety Board (TSB) (2018). "Rail transportation occurrence data.", Ottawa, Ontario, Canada.
85. Ugai, K., and Leshchinsky, D. (1995). "Three-dimensional limit equilibrium and finite element analyses: a comparison of results." *Soils Found.*, 35(4), 1-7.
86. Wong, R., Thomson, P., and Choi, E. (2006). "In situ pore pressure responses of native peat and soil under train load: a case study." *J. Geotech. Geoenviron. Eng.*, 132(10), 1360-1369.

87. Xue, F.-C., and Zhang, J.-M. (2014). "Dynamic Responses of Rail-Embankment-Foundation on High-Speed Railways under Moving Loads." *Proc., 10th Asia Pacific Transportation Development Conf.*, ASCE, Beijing, China, 655-662.
88. Zhang, T., Cui, Y., Lamas-Lopez, F., Calon, N., and D'Aguiar, S. C. (2016). "Modelling stress distribution in substructure of French conventional railway tracks." *Constr. Build. Mater.*, 116, 326-334.
89. Zheng, Y.-R., Zhao, S.-Y., Kong, W.-X., and Deng, C.-J. (2005). "Geotechnical engineering limit analysis using finite element method." *Yantu Lixue(Rock Soil Mech.)*, 26(1), 163-168.
90. Zienkiewicz, O., Humpheson, C., and Lewis, R. (1975). "Associated and non-associated visco-plasticity in soils mechanics." *J. Geotechnique*, 25(5), 671-689.
91. Zienkiewicz, O. C., Taylor, R. L., Nithiarasu, P., and Zhu, J. (1977). *The finite element method*, McGraw-hill, London.